Alma Mater Studiorum · Università di Bologna

**Scuola di Scienze**
**Corso di Laurea Magistrale in Fisica del Sistema Terra**

# Axisymmetric tornado simulations using semi-slip boundary conditions

**Relatore:**
**Dott. Carlo Cintolesi**

**Presentata da:**
**Stefano Giove**

**Correlatori:**
**Dott. Mario Marcello Miglietta**
**Dott. Richard Rotunno**

**Anno Accademico 2022/2023**

## Sommario

La fluidodinamica dei tornado è spesso studiata mediante simulazioni idealizzate a simmetria assiale, isolando le caratteristiche delle supercelle che sono importanti per la loro formazione. I vortici prodotti da queste simulazioni sono dei vortici potenziali, caratterizzati da una regione a momento angolare costante. Solitamente vengono utilizzate condizioni al contorno al suolo no-slip, portando alla formazione di un cosiddetto "potential vortex boundary layer", con una struttura a due strati e un flusso radiale verso il centro del vortice (inflow).

Lo scopo di questo studio è quello di indagare gli effetti di condizioni al contorno semi-slip su tornado simulati, effettuando simulazioni idealizzate a simmetria assiale. I parametri fondamentali sono uno swirl ratio $S_r$ (relativo alla rotazione del sistema) e un numero di Reynolds $R_e$ (relativo alla diffusione). Le condizioni semi-slip sono realizzate imponendo una forza di attrito alla superficie; ciò ha consentito di introdurre il coefficiente di attrito ($C_d$) come parametro, fornendo condizioni più realistiche rispetto alle condizioni no-slip e free-slip solitamente impiegate. L'interesse per questo argomento è dovuto alla sensibilità della struttura dei tornado presenti in natura alle condizioni al contorno al suolo per l'attrito, da cui segue la necessità di condizioni più realistiche.

I risultati indicano che il potential vortex boundary layer è preservato per condizioni semi-slip in un ampio range di valori di $C_d$ ($C_d = 0.2 - 0.005$). Una diminuzione di $C_d$ causa un assottigliamento dello strato inferiore del boundary layer, che scompare tra $C_d = 0.005$ e $C_d = 0.001$. La diminuzione di $C_d$ per $S_r$ e $R_e$ costanti comporta gli stessi cambiamenti nella struttura del vortice osservati in studi precedenti per simulazioni no-slip con $S_r$ crescente e $R_e$ costante. Questi risultati mostrano che lo spazio dei parametri fondamentali è tridimensionale ($C_d - S_r - R_e$). Infine, nell'intervallo $C_d = 0.2 - 0.035$, una diminuzione dell'attrito può portare ad un'intensificazione del vortice; ciò è dovuto all'intensificazione e allo spostamento dell'inflow verso il centro del vortice, unito alla ridotta dissipazione di momento angolare.

**Abstract**

The fluid dynamics of tornadoes is often investigated using idealized axisymmetric simulations, isolating supercell features relevant to tornadogenesis. The vortices produced by these simulations are potential vortices, characterized by a region of constant angular momentum $\Gamma$. No-slip lower boundary conditions are usually employed in numerical simulations, leading to the formation of a potential vortex boundary layer, with a two-tiered structure and a radially inward flow towards the center of the vortex (inflow).

The purpose of this study is to investigate the effects of semi-slip boundary conditions on simulated tornadoes, performing idealized axisymmetric simulations. The governing parameters are a swirl ratio $S_r$ (related to the system's rotation) and a Reynolds number $R_e$ (related to diffusion). The semi-slip conditions are obtained by imposing a surface drag, allowing the introduction of a friction coefficient parameter ($C_d$), providing conditions more realistic than the no-slip and free-slip conditions usually employed in numerical simulations. The motivation for this work is that the structure of natural tornadoes is sensitive to the lower boundary conditions for friction, hence the importance of more realistic conditions.

The results show that the potential vortex boundary layer is preserved for semi-slip conditions under a wide range of $C_d$ values ($C_d = 0.2 - 0.005$). A decrease in $C_d$ causes a narrowing of the lower frictional tier of the boundary layer, which vanishes between $C_d = 0.005$ and 0.001. The decrease in $C_d$ for fixed $S_r$ and $R_e$ results in the same changes in the vortex's structure previously observed for no-slip simulations under increasing $S_r$ and fixed $R_e$. This shows that the governing parameter space is three-dimensional ($C_d - S_r - R_e$). Finally, within the range $C_d = 0.2 - 0.035$, a decrease in friction can lead to a vortex intensification due to the enhancement and shift of the inflow towards the vortex's center, combined with the reduced dissipation of $\Gamma$.

# Contents

# Chapter 1

# Introduction

Tornadoes are intense columnar vortices associated with cumulus and cumulonimbus clouds ([How13], [Rot13]). Tornadoes are often visible as funnel clouds, with the pressure drop inducing the condensation of water vapor, as can be seen in figure 1.1. Almost all tornadoes arise from a particular type of thunderstorm cell: the supercell ([Dav15]). Supercell thunderstorms are long-lived, quasi-steady, severe storms characterized by a rotating updraft (mesocyclone) ([WH06]). Tornadoes can last from a few seconds to more than one hour, a typical tornado lasting approximately $\sim$ 10 minutes, while the wind speeds can range from $\sim$ 20 m/s to $\sim$ 140 m/s ([How13]).

These complexities pose challenges for performing direct measures on tornadoes. As a result, the fluid dynamics of tornadoes is studied through a combination of laboratory experiments and numerical simulations. There is a significant scale disparity between tornadoes and their mesocyclone: tornadoes have a median radius of maximum wind of roughly 150 meters [AW08], while the diameter of the parent mesocyclone is of the order of kilometers. Consequently, both investigation approaches aim to isolate the features of supercell thunderstorms that are important for tornado formation and for the characteristics of mature tornadoes. The primary example of a laboratory experiment following this approach is [War72]. In his setup, as well as in the updated version by [CSA77], the updraft of the supercell is represented by an upward-directed fan that produces an upward volume flux, while the rotation of the mesocyclone is replicated by a rotating screen, which transfers angular momentum to the upward flow. The geometry of the apparatus is designed to replicate the flow in a supercell. The solutions are determined by two nondimensional parameters, a swirl ratio $S_r$, related to the angular momentum imparted by the rotating screen to the updraft, and a Reynolds number $R_e$, related to diffusion effects. The vortices produced by the experimental setups display different structures for increasing values of $S_r$ ([War72]), replicating the structures observed in natural tornadoes: the structures range from single-celled, laminar vortices with a central updraft for low values of $S_r$, to two-celled vortices with an updraft surrounding a central downdraft for larger $S_r$, while for even larger $S_r$ the vortex breaks down into

**Figure 1.1:** Example of a tornado. Courtesy of Hank Schyma.

satellite vortices swirling around a common axis.

As explained in [DTB01], analysts attempting to employ a three-dimensional cloud model to numerically simulate a tornado are faced with challenging requirements, among which are the need for a very fine grid resolution (grid spacing of 10 meters or less), lower boundary conditions capable of reproducing the interaction of the surface with the turbulent flow, and the inclusion of rotational damping in the turbulence parameterization. As a result, most of the current knowledge on the fluid dynamics of tornadoes comes from axisymmetric idealized simulations. A prominent example is the work of [Fie95], who proposed the idealization of the mesocyclone as an axisymmetric, rotating, closed-domain cylinder with a prescribed upward forcing at the center in lieu of the supercell's updraft. Analogously to the laboratory experiments of [War72], the solutions to this approach are determined by a swirl ratio and a Reynolds number. These idealized simulations replicate the effect of increasing swirl ratio on the vortex structure only under no-slip lower boundary conditions, whereas for free-slip conditions the simulated tornadoes are large two-celled vortices over a wide range of $S_r$ values ([Rot13]). These findings emphasize the importance of the lower boundary layer conditions on simulated tornadoes.

As highlighted by [Rot14], the interaction between atmospheric vortices of every size, from dust devils to midlatitude cyclones, and the lower frictional boundary gives rise to a special kind of boundary layer, a rotating-flow boundary layer. The distinctive feature of rotating-flow boundary layers is the presence of a secondary circulation (a flow in

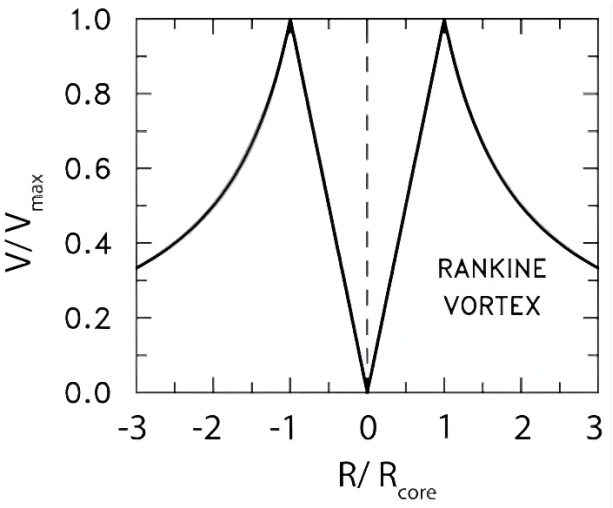


**Figure 1.2:** Schematic diagram of a Rankine vortex.

the radial-vertical plane) that affects the primary circulation (the swirling flow in the azimuthal direction). For instance, the secondary circulation is fundamental in transporting heat and angular momentum in the interior of hurricanes and tropical cyclones ([Ema86]). For tornadoes, the secondary circulation is represented by a radially inward flux (inflow), directed towards the center of the vortex, which feeds into the updraft of the vortex. Mobile Doppler radar measurements ([Tan+07]) indicate that tornadoes exhibit radial profiles of azimuthal wind similar to the Rankine vortex. The Rankine vortex, of which a diagram is shown in figure 1.2 (from [How13]), is a combination of a solid-body rotation flow for $0 \leq r \leq R_{core}$, characterized by a linear increase of azimuthal velocity $v$ with radius, and a potential vortex for $r > R_{core}$, characterized by constant angular momentum $\Gamma$, and thus a $v \propto 1/r$ profile of the tangential wind speed. [Rot13] has shown that the intense swirling motion close to the ground can be understood by analyzing the boundary layer of the outer flow under no-slip boundary conditions, hence focusing on the potential vortex boundary layer. The boundary layer of a potential vortex under no-slip conditions was shown to exhibit a two-tiered structure ([BSB71]), with the lower frictional tier below an inviscid upper tier. The tiers are delimited by the maximum in $-ru$, where $u$ is the radial velocity.

The structure of tornadoes is sensitive to lower boundary conditions. Although no-slip conditions are a convenient choice, allowing to exploit the results of [BSB71], a more physically consistent representation of the lower boundary for friction is needed. In the present work, we aim to investigate the effects of semi-slip boundary conditions on mature simulated tornadoes. The use of a surface drag approach as semi-slip boundary conditions allows us to introduce a friction coefficient parameter $C_d$. Exploring a wide range of $C_d$ values, we can investigate lower boundary conditions that are more realistic

than the no-slip and free-slip conditions normally employed in storm models.

### Aims of the study

We explore the impact of surface drag on the potential vortex boundary layer, assessing if the boundary layer is preserved under no-slip conditions and how the two-tiered structure evolves for decreasing $C_d$. The findings can provide insights not only into the science of tornadoes, but more generally they can offer information on the boundary layer of potential vortices. For instance, in tropical cyclones the tangential winds decrease approximately following a potential vortex radial profile, although the decay exponent of $v \propto r^{-\alpha}$ has been found to vary between $\alpha = 0.5 - 0.7$ ([MMW05]).

The adoption of semi-slip lower boundary conditions allows us to study the role of surface drag on the structure of mature tornadoes. [Rot+16] have shown that under no-slip conditions the solutions are determined by the combination of $S_r - R_e$, hence the structure of the vortex depends on the position in the two-dimensional parameter space defined by $S_r$ and $R_e$. The goal of this study is to find whether the introduction of the friction coefficient parameter plays a role in determining the structure of the vortex, turning the two-dimensional parameter space into a three-dimensional $C_d - S_r - R_e$ parameter space.

The use of no-slip conditions forces the wind speeds to be identically zero at the surface. As a result, the simulated vortices have limited intensities right above the surface, near the vortex center. Clearly, the extensive socioeconomic impact of tornadoes ([AS16], [SM15]) stems from the intense winds that occur at the lowest levels ($< 15$ meters). Therefore, it is crucial to employ lower boundary conditions that allow a better representation of the intense near-surface winds of natural tornadoes. In the present work, we investigate the capability of semi-slip conditions to provide results more representative of natural tornadoes at the lowest levels. This goal is even more important considering the recent findings of [KW23], whose Doppler on wheels measurements indicate that the strongest winds are found at the lowest observed levels. In particular, restricting the analysis to those samples containing measurements at very low levels ($< 15$ meters above radar level), they found that nearly all the vertical profiles of $v$ exhibited the strongest winds near the lowest level. Similar results were obtained by [KW13], which used a combination of radar, anemometer, and ground-based velocity-track display method to investigate the wind field of a tornado near Russell, Kansas, finding the peak wind intensity at $\sim 5$ meters above ground level. These findings provide further motivation for the present study.

### Method of analysis

The work is carried out by performing idealized axisymmetric simulations of tornadoes. The design of the experiment is based on the approach of [Rot+16], with a closed do-

main rotating cylinder representing the full extent of the supercell, while the buoyancy is simulated using a prescribed upward forcing. The use of a closed domain provides unambiguous boundary conditions, but it can lead to spurious effects of the domain size on the dynamics of the simulated vortex. This problem is tackled by employing a very large domain size compared to the dimension of a typical tornado, along with a linear damping layer near the domain top, which blocks disturbances generated by the impermeable top boundary layer. While [Rot+16] employ the conventional no-slip bottom boundary conditions, we make use of semi-slip conditions, with a drag force formulation of the surface shear stresses. This allows the introduction of the friction coefficient $C_d$, which determines the solutions along with the swirl ratio $S_r$ and the Reynold number $R_e$. The definitions of $S_r$ and $R_e$ are provided in section 2. It is worth mentioning that in our simulations the Reynolds number is $R_e = 10000$, while [Rot13] estimates an atmospheric Reynolds number of $10^{10}$ for a typical supercell. Our goal is to gain insights into an unsteady and turbulent process using idealized, laminar, and steady-state solutions. Clearly, the present work does not attempt to give the most realistic representation of a tornado, but rather to understand its dynamics working within a simplified framework. The validity of this approach is confirmed by the resulting radial profile of tangential winds, which displays a potential vortex behavior from the vortex core outward, in agreement with the radial profiles of natural tornadoes ([Tan+07]).

**The present work in the contex of previous studies**

To the best of our knowledge, [Fie17] is the only other work where semi-slip conditions are used as lower boundary conditions for simulations of mature tornadoes. While [Fie17] employs three $C_d$ values and a linear approach for the drag force formulation of the surface shear stresses, we explore sixteen $C_d$ values within a more refined nonlinear approach. As mentioned before, the no-slip conditions have been the standard choice for idealized axisymmetric tornado simulations. [Rot+16] have thoroughly explored the $S_r - R_e$ space under no-slip conditions, and their solutions replicate the vortex structures obtained in laboratory experiments ([War72], [CSA77], [Chu+79]).

Previous studies have used semi-slip lower boundary conditions to investigate the role of surface drag in tornadogenesis. [Rob+16] have described three mechanisms by which surface drag influences the generation of a tornado by a supercell, while [CP17] used semi-slip three-dimensional simulations to compare tornadic and nontornadic supercell environments.

Another approach, complementary to the method employed in this work, is to perform three-dimensional simulations using a Large Eddy Simulation (LES) framework for turbulence. For instance,[Nol+17] used this approach to obtain various measures of tornado intensity, while [LLX00] showed that a LES model is capable of reproducing the structures obtained with axisymmetric models and laboratory experiments.

On the opposite side of the spectrum compared to the idealized approach followed

in this work, some attempts have been made at running simulations of supercells at resolutions fine enough to explicitly solve tornadoes. Notably, [Orf+17] ran a simulation with 1.84 billion grid points, with an inner mesh with a grid spacing of 30 meters, simulating the evolution of a long-track, damaging tornado.

# Chapter 2

# Physical problem

In the present work, the investigation of the effects of semi-slip boundary conditions on supercell tornadoes is carried out idealizing the supercell thunderstorm, simplifying and isolating the characteristics that are important for tornado formation and features. We follow the Fiedler chamber approach ([Fie95]), of which a schematic diagram is shown in figure 2.1. The supercell's rotating updraft column is idealized as a cylinder of radius $R$ and height $Z$. In the meteorological context, $R$ represents the radius of the thunderstorm's updraft, while $Z$ the height of the tropopause. The domain rotates at the rate $\Omega$, producing an angular momentum distribution $\Omega r^2$. The role of the thunderstorm's buoyancy acceleration is played by a prescribed upward force per unit mass $F(r, z)$. The Fiedler chamber approach allows us to assume axial symmetry, reducing the physical problem to only two dimensions, the radial and vertical ones.

A schematic diagram of the domain used for the simulations is presented in figure 2.2. The present work shares the same physical problem with [Rot+16], except for the lower boundary layer conditions. A summary of the parameters characterizing the problem is

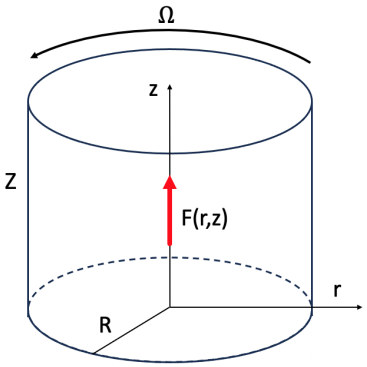


**Figure 2.1:** Schematic diagram of the Fiedler chamber. R is the radius of the chamber, Z its height, $\Omega$ its rotation rate, and $F(r, z)$ the prescribed upward force per unit mass.

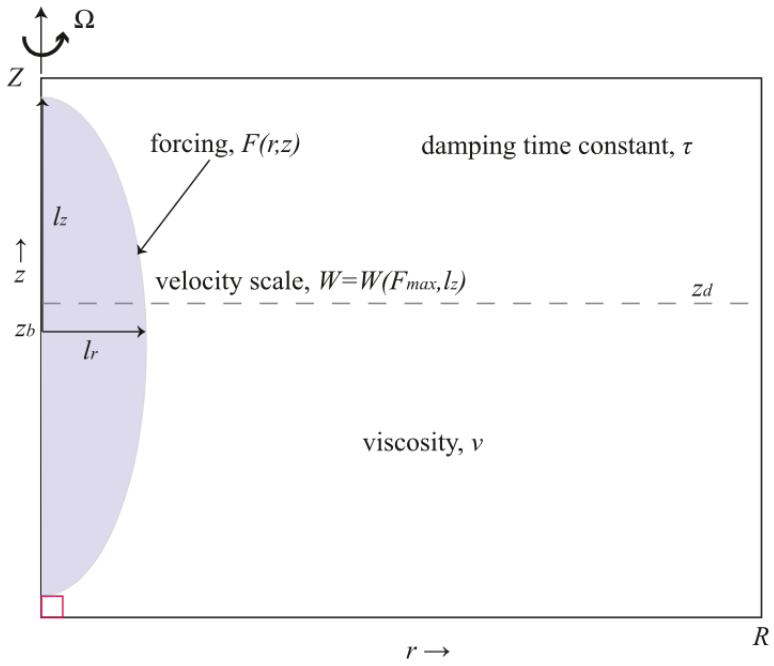


**Figure 2.2:** Schematic diagram of the computational domain employed for the numerical simulations. (After [Rot+16])

| R | Z | $z_b$ | $l_z$ | $l_r$ | $z_d$ | $\tau$ | W | $W_e$ | Ω | $\nu$ | $C_d$ |
|---|---|---|---|---|---|---|---|---|---|---|---|
| 20 km | 15 km | 8 km | 7 km | 3 km | 8 km | 100 s | 80 m/s | 66 m/s | Variable | Variable | Variable |

**Table 2.1:** Parameters settings for the domain shown in figure 2.2. $C_d$ is the friction coefficient, $W_e$ the effective forcing velocity.

presented in table 2.1. The $r = 0$ and $r = R$ boundaries are impermeable free-slip walls, while the domain top boundary ($z = Z$) is an impermeable no-slip wall. We employed semi-slip conditions for the domain bottom boundary, where semi-slip refers to the usage of a drag force formulation of the surface shear stresses:

$$\tau_{i3} = \rho C_d u_i V = \rho C_d u_i \sqrt{u^2 + v^2} \tag{2.1}$$

with $C_d$ the drag coefficient, and $V$ the surface velocity. We note how the present formulation is non-linear, in contrast with the linear approach of [Fie17], who employed a constant $V = V_H$.

The prescribed upward forcing is active in an elliptically shaped region of vertical and horizontal axes $l_z$ and $l_r$, respectively. The maximum forcing is located at the center of the ellipse, $(r, z) = (0, z_b)$. Integrating vertically the upward force per unit mass for

$r = 0$:

$$W^2 = \int_{z_b - l_z}^{z_b + l_z} 2F(0, z)\, dz, \tag{2.2}$$

where $W$ is the forcing velocity, also called thermodynamic speed limit, as it is the velocity that a parcel at rest at the bottom of the forcing region and for $r = 0$ would acquire at the top of the forcing region if buoyancy was the only force acting on it ([Fie94]). The forcing $F(r, z)$ is tuned so that $W = 80$ m/s.

To prevent numerical disturbances produced at the domain top from reaching the vortex, a damping layer is introduced above the height $z_d$. In particular, the damping is a linear relaxation, with time constant $\tau$. Figure 2.2 shows that the updraft forcing region and the damping layer overlap; this implies that the forcing velocity must be corrected, taking into account the role of the damping layer. The effective forcing velocity $W_e$ has been estimated to be $W_e = 66$ m/s in [Rot+16]. Measurements made by armored aircrafts and balloons indicate that updrafts in supercells can exceed 50 m/s ([How13] chapter 3, page 139, figures 3.14, 3.15), hence the value of $W_e$ is in agreement with observed supercells' updrafts. The large radial extension of the domain plays a role in blocking the domain top disturbances from being fed back into the vortex traveling along the outer boundary. In fact, the radial size of the domain, $R = 20$ km, is much larger than the median radius of maximum wind of tornadoes, estimated to be approximately $\approx 150$ meters from Doppler on wheels radar observations ([AW08]). The red square in figure 2.2 represents the 1 km $\times$ 1 km window of the domain, hereafter called corner region, where some of the following analysis will be carried out.

We note from table 2.1 that all the parameters have a fixed value except for $\Omega$, $\nu$ (kinematic viscosity), and $C_d$. The fixed parameters have values that fulfill the requirement of similarity to a supercell. The two dimensional variable parameters $\Omega$ and $\nu$ can be made nondimensional, obtaining the swirl ratio $S_r = \Omega l_r / W$, related to the system's rotation, and the Reynolds number $R_e = W l_r / \nu$, representing diffusive effects. The set $S_r$ - $R_e$ - $C_d$ of nondimensional variable parameters determines the solution. The combinations of $S_r$ - $R_e$ - $C_d$ employed in the present work are listed in table 2.2. Following the notation of [Fie17], we will refer to the no-slip conditions as $C_d = \infty$, and to the free-slip conditions as $C_d = 0$. We kept $R_e$ fixed to 10000, and for each of the three $S_r$ values we performed sixteen semi-slip simulations, with the $C_d$ values presented in table 2.2. Along with the semi-slip cases, we performed simulations with no-slip and free-slip boundary conditions, in order to validate the semi-slip simulations for very high and very low friction. Additionally, the no-slip simulations provided the necessary benchmark for the semi-slip cases. Free-slip conditions are numerically obtained from semi-slip conditions with $C_d = 10^{-10}$.

For the purpose of the present study, it is fundamental to describe the behavior of the solution under no-slip conditions in the $S_r$ - $R_e$ parameter space. The dependence of vortex structure on increasing swirl ratio for fixed Reynolds number is illustrated in figure

| $R_e = 10000$ kept constant | $S_r = 0.005$ | $S_r = 0.01$ | $S_r = 0.04$ |
|---|---|---|---|
| $C_d = \infty$ | no-slip | - | - |
| $C_d = 0.2$ | - | - | - |
| $C_d = 0.1$ | - | - | - |
| $C_d = 0.08$ | - | - | - |
| $C_d = 0.07$ | - | - | - |
| $C_d = 0.06$ | - | - | - |
| $C_d = 0.05$ | - | - | - |
| $C_d = 0.04$ | - | - | - |
| $C_d = 0.035$ | - | - | - |
| $C_d = 0.03$ | - | - | - |
| $C_d = 0.025$ | - | - | - |
| $C_d = 0.02$ | - | - | - |
| $C_d = 0.015$ | - | - | - |
| $C_d = 0.01$ | - | - | - |
| $C_d = 0.005$ | - | - | - |
| $C_d = 0.001$ | - | - | - |
| $C_d = 0.0001$ | - | - | - |
| $C_d = 0$ | free-slip | - | - |

**Table 2.2:** Combinations of $S_r$ - $R_e$ - $C_d$ employed in the present work. We use the dash symbol to indicate that every $S_r - C_d$ combination has been used in the simulations. The $C_d = \infty$ are no-slip simulations, the $C_d = 0$ are free-slip simulations.

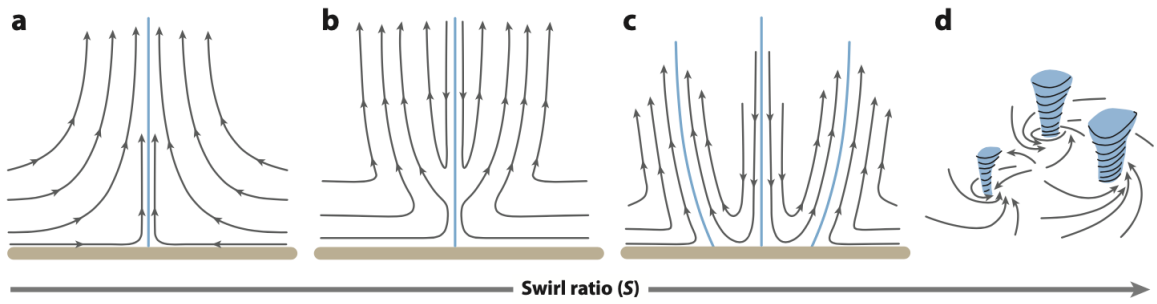


**Figure 2.3:** Evolution of vortex structure for increasing swirl ratio: a) single-celled b) transition/optimal vortex c) two-celled d) multiple vortices. (After [Rot13])

2.3. For a small value of swirl ratio, the solution is a single-celled vortex, characterized by a central updraft (panel a). Increasing $S_r$, the vortex tightens and intensifies, until it undergoes a transition, with a single-celled vortex that abruptly becomes two-celled above a certain height, with a centerline downdraft surrounded by an updraft (panel b). For increasing swirl ratio, the interface between the single-celled and two-celled vortices gradually shifts downward. At a certain value of $S_r$, the downdraft reaches the ground, and the vortex attains a complete two-celled structure (panel c). A further increase in swirl ratio enlarges the vortex, until for even larger $S_r$ the two-celled vortex breaks into multiple vortices revolving around a common center (panel d).

The transition described in figure 2.3b is a vortex breakdown event. This phenomenon is essentially a hydraulic jump: for certain values of swirl ratio, the single-cell vortex is supercritical, and disturbances cannot propagate upstream (downward) against the axial updraft, hence the transition to the downstream (upward) flow must be abrupt ([Rot13]). Vortices displaying a structure like the one in figure 2.3b are defined optimal vortices, characterized by a peak in pressure drop, and strong swirling motion in the one-celled portion of the vortex ([Rot+16]).

The $S_r$ - $R_e$ parameter space has been thoroughly explored in [Rot+16]. They observed that optimal vortices (and vortex breakdown events) occur for $S_r \propto R_e^{-1/3}$. Solutions for $S_r$ lower than this proportionality are single-celled vortices, while those for $S_r$ larger than this proportionality are two-celled vortices. The solution matrix reported in [Rot+16] allowed us to direct the investigation of the effect of semi-slip conditions on solutions that in their no-slip counterpart showed structures like those of panels a,b, and c of figure 2.3. Indeed, for $(R_e = 10000, S_r = 0.005)$ the no-slip solution is one-celled, for $(R_e = 10000, S_r = 0.01)$ it is very close to transition, while for $(R_e = 10000, S_r = 0.04)$ the no-slip solution is two-celled.

# Chapter 3

# Governing equations and model setup

## 3.1 Governing equations

The dynamics of the physical problem presented in section 2 can be described by the axisymmetric, constant-density, incompressible Navier-Stokes equations in a rotating frame of reference in cylindrical coordinates,

$$\begin{cases} \dfrac{\partial u}{\partial t} = -u\dfrac{\partial u}{\partial r} - w\dfrac{\partial u}{\partial z} - \dfrac{\partial \phi}{\partial r} + 2\Omega v + \dfrac{v^2}{r} + \dfrac{1}{\rho}\left(\dfrac{\partial \tau_{rr}}{\partial r} + \dfrac{\partial \tau_{rz}}{\partial z}\right) - \alpha(z)\dfrac{u}{\tau} & \text{(3.1a)} \\ \dfrac{\partial v}{\partial t} = -u\dfrac{\partial v}{\partial r} - w\dfrac{\partial v}{\partial z} - 2\Omega u - \dfrac{uv}{r} + \dfrac{1}{\rho}\left(\dfrac{\partial \tau_{r\theta}}{\partial r} + \dfrac{\partial \tau_{\theta z}}{\partial z}\right) - \alpha(z)\dfrac{v}{\tau} & \text{(3.1b)} \\ \dfrac{\partial w}{\partial t} = -u\dfrac{\partial w}{\partial r} - w\dfrac{\partial w}{\partial z} - \dfrac{\partial \phi}{\partial z} + F(r,z) + \dfrac{1}{\rho}\left(\dfrac{\partial \tau_{rz}}{\partial r} + \dfrac{\partial \tau_{zz}}{\partial z}\right) - \alpha(z)\dfrac{w}{\tau} & \text{(3.1c)} \\ \dfrac{\partial \phi}{\partial t} = -c_s^2\left[\dfrac{1}{r}\dfrac{\partial (ru)}{\partial r} + \dfrac{\partial w}{\partial z}\right] & \text{(3.1d)} \end{cases}$$

where $u$, $v$, $w$ are the radial, tangential (azimuthal), and vertical velocities respectively, $\phi = p/\rho$, $p$ is the pressure and $\rho$ a constant density, $\Omega$ the domain's rotation rate, $\tau_{ij}$ the stress tensor, $\alpha(z)$ is the damping function, $F(r,z)$ the prescribed upward forcing, and $c_s = 300$ m/s is the speed of sound in air. Since $V_{max}/c_s \ll 1$, where $V_{max}$ indicates the maximum simulated wind speeds, the flow is effectively solenoidal ($\nabla \cdot \vec{u} = 0$), and it can be considered effectively incompressible ([Bat00] chapter 3.6, pages 183-184). The choice of constant density reflects the fact that we focus primarily on the lowest $\sim 1$ km above ground level, where the constant-density assumption is valid. Moreover, it allows us to employ the split-explicit time integration technique for compressible flows

([WS02]), already existing within the framework of the Cloud Model 1 (CM1) numerical model employed in this study.

The updraft forcing $F(r, z)$ is defined following [Nol05],

$$F(r,z) = \begin{cases} F_{max} \cos\left(\frac{\pi}{2}\chi\right) & \text{for } \chi < 1 \\ 0 & \text{for } \chi \geq 1 \end{cases} \tag{3.2}$$

where

$$\chi = \left[\frac{(z-z_b)^2}{l_z^2} + \frac{r^2}{l_r^2}\right]^{\frac{1}{2}}. \tag{3.3}$$

is a modified distance from the center of the ellipse.

The last terms on the right-hand sides of equations (3.1a), (3.1b), and (3.1c) are the linear damping terms. The coefficient $\alpha(z)$ governs the distance over which full damping with time constant $\tau$ is achieved.

$$\alpha(z) = \begin{cases} \frac{1}{2}\left[1 - \cos\left(\pi\frac{z-z_d}{Z-z_d}\right)\right] & \text{for } z > z_d \\ 0 & \text{for } z \leq z_d \end{cases} \tag{3.4}$$

## 3.2 Numerical implementation and model setup

The numerical model used in this study is Cloud Model 1 (CM1) ([BF02],[BR09]) in its 19.10 release. CM1 represented an optimal choice, as it provided a framework used in previous studies in the field ([Rot+16]). Additionally, CM1 offers the possibility to perform idealized axisymmetric simulations, as well as the option to employ semi-slip bottom boundary conditions. CM1 is a software written in FORTRAN 90.

The two-dimensional physical problem, described in figure 2.2, is numerically obtained by taking a one-grid-cell slice of the cylindrical domain and imposing periodic boundary conditions at the azimuthal boundaries.

The constant density assumption is obtained by following this rationale: we impose a dry adiabatic base state, with potential temperature $\theta = 300$ K and surface pressure $p_{00} = 1000$ hPa, this base state is in hydrostatic balance and is kept constant in time. Since the base state is in balance, and exploiting the assumption of solenoidal flow, all the terms referred to the pressure base state give no contribution to the tendencies of the fields integrated in time. Therefore, we can simply consider the perturbation pressure $p'(t) = p(t) - p(0)$, which behaves as a pressure divided by a constant density $p'(t) = \phi(t)$. Along with the pressure base state, we employed a zero-winds initial condition.

The numerical scheme used to integrate in time equations (3.1a-3.1d) is the third-order Runge–Kutta scheme described in [WS02], which uses Klemp-Wilhelmson ([KW78]) split-time steps for acoustic modes, with explicit treatment of the acoustic terms in both

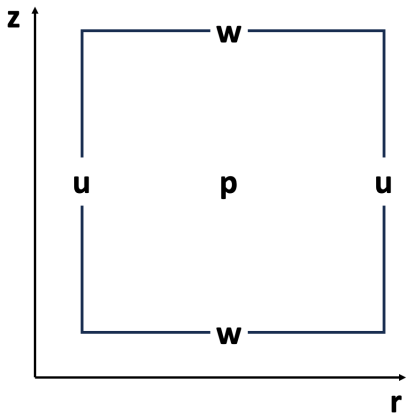


**Figure 3.1:** Bidimensional slice of a grid cell showing the arrangement of the variables on the staggered grid. The scalars are at the centroid of the cell.

vertical and horizontal directions. To improve the stability of the split-time integration scheme, a weak artificial damping of acoustic waves is introduced, following the three-dimensional divergence damper of [SK92]. An adaptive time step is used, to maintain numerical stability. We employ fifth-order advection schemes in both vertical and horizontal directions for scalars and vectors. The advection of velocities is performed using a fifth-order WENO (weighted essentially non-oscillatory) scheme on the final Runge-Kutta step ([Bor+08]). No turbulence parameterization is employed in the present work.

The model employs a staggered grid, and the staggering is as in figure 3.1. The scalar variables are located at the centroids of the cell. The equations are solved on a stretched

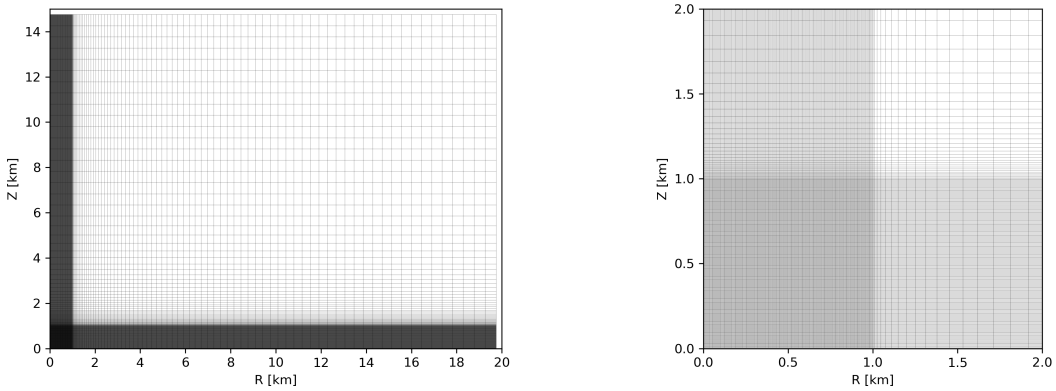


**(a)** **(b)**

**Figure 3.2:** Visualization of the centroids of the computational grid for a) the full domain, and b) the region $[(0,0),(2,2)]$.

grid with 276 radial grid points and 266 vertical grid points. The radial grid spacing is 5 meters for $r < 1$ km, and it gradually increases to 495 meters at $r = 20$ km. The vertical grid spacing is 5 meters for $z < 1$ km, gradually increasing to 495 meters at $z = 15$ km. The visualization of the centroids of the computational grid is presented in figure 3.2a, along with a windowed-in view of the grid in the region $[(0, 0), (2, 2)]$ in figure 3.2b.

# Chapter 4

# Results

## 4.1 Preliminary results and validation

### 4.1.1 Model output overview

Before moving to the research outcomes, let us examine the outputs of a generic simulation. In the present work, steady-state solutions are the objects of the investigation. The nature of the steadiness is related to the nature of the vortex: one-celled vortices achieve an asymptotic steady state, while transitional and two-celled vortices reach a statistically steady state. Therefore, every simulation has been carried out until a stationary state was reached. Moreover, all data and plots represent an average over 10000 seconds (10 model outputs), to further eliminate any remaining unsteadiness.

For simplicity, the pressure divided by a constant density $\phi$ will be referred to simply as pressure. Figure 4.1 shows the tangential, radial, and vertical velocities, along with the pressure for a simulation with $S_r = 0.01$, $R_e = 10000$ and no-slip boundary conditions. The plots show the whole vertical extent of the domain and most of its radial extent. The most noticeable feature is the confinement of the vortex to a small fraction of the domain, near $r = 0$, while the rest of the domain is almost featureless. This behavior is expected, as the domain size has been intentionally chosen to be large compared to the vortex in order to prevent disturbances generated near the domain's top from being fed back into the inflow of the vortex. The domain size combined with the linear relaxation in the damping layer inhibits disturbances from reaching the inflow region traveling along the outer boundary, as well as downward from the domain top. Consequently, the study focuses primarily on the vortex core (defined as the region where the vortex attains the strongest rotation, in figure 4.1 $0 < r \lesssim 1$km) and its inflow (defined as the area of the domain where air flows inward, towards $r = 0$). We note how the damping layer reduces the tangential and vertical velocities near the domain top, while there is an outflow (air flowing radially outward, away from $r = 0$) due to the effect of the upper boundary. The overall circulation then describes an in-up-and-out flow, schematically illustrated in

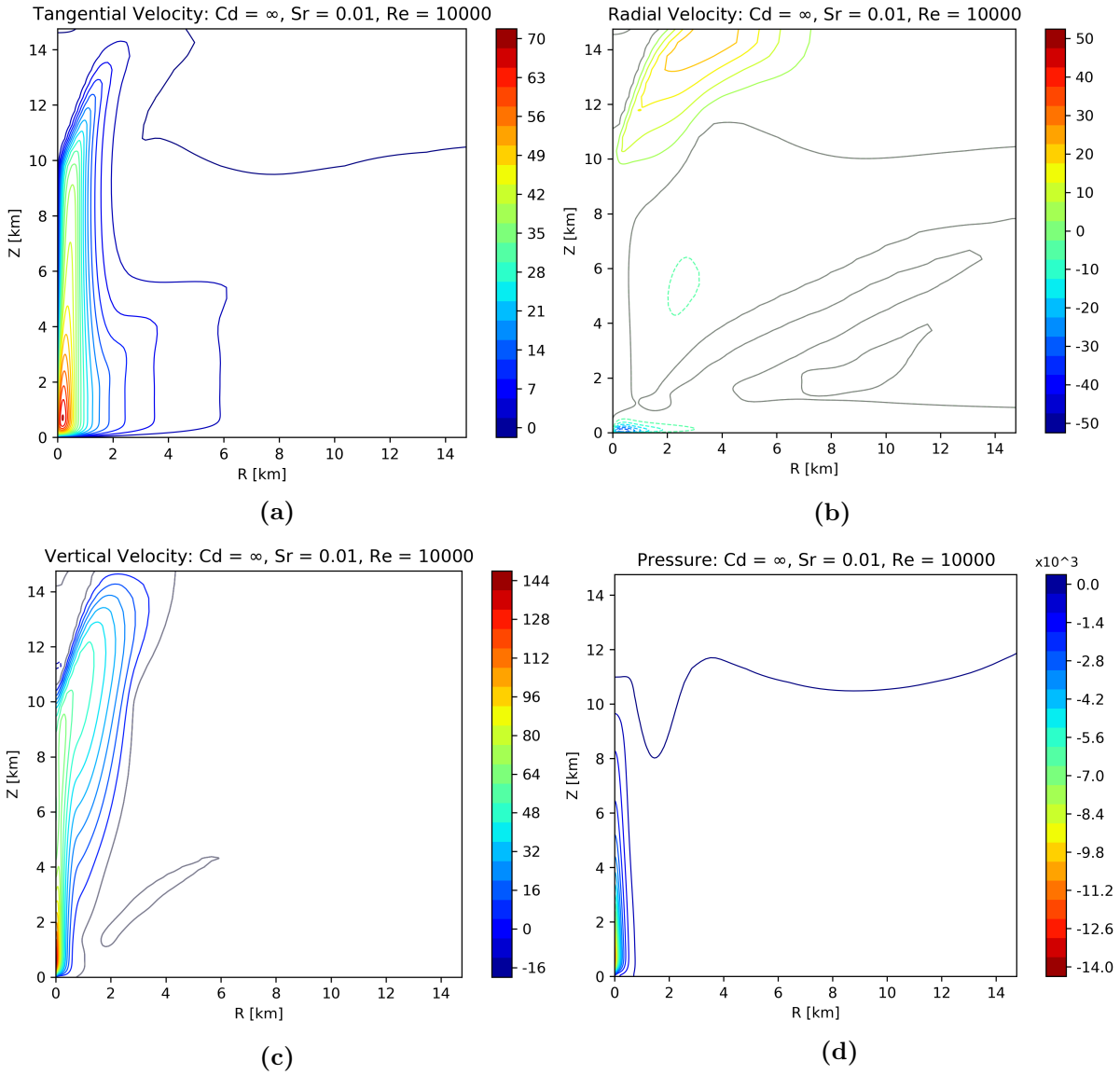


**Figure 4.1:** Contourlines of a) tangential, b) radial, c) vertical velocity [m/s], and d) pressure [Pa·$m^3$/kg] for $S_r = 0.01$, $R_e = 10000$ and no-slip ($C_d = \infty$) boundary conditions. For the radial and vertical velocities the zero contourline is in grey.

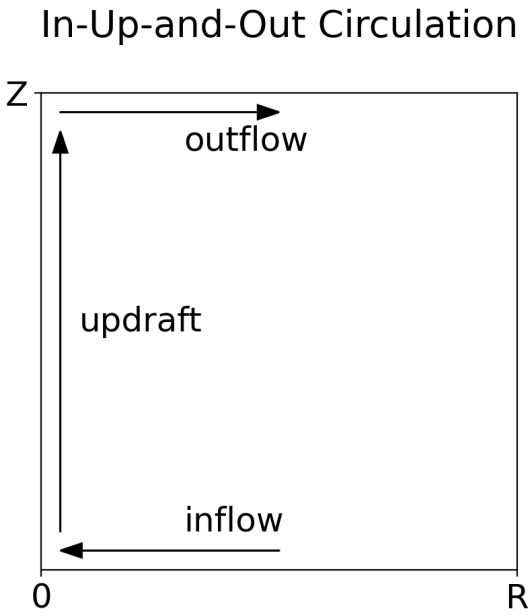


**Figure 4.2:** Schematic diagram of the in-up-and-out circulation.

figure 4.2.

### 4.1.2 No-slip simulations

To verify that the model is able to reproduce the main features of interest, we compare the no-slip simulations with the expected results ([Rot13]). In particular, these simulations can be evaluated against those presented in [Rot+16]. This comparison is particularly significant since the present model setup is very similar to the one of [Rot+16]: the domain size, the grid spacings, the updraft forcing, and the linear damping are the same. The main difference is that the present study is based on CM1 in its 19.10 version, while [Rot+16] employs the 17.0 release. On top of the validation purpose, the description of the no-slip simulations allows us to introduce concepts and terms that will be extensively used in the following chapters, where the effects of the semi-slip boundary conditions will be discussed.

As can be seen from [Rot+16], the vortex type changes varying the swirl ratio with fixed Reynolds number. For a given Reynolds number, a low swirl ratio implies a single-celled vortex, a swirl ratio $S_r \propto R_e^{-1/3}$ yields an optimal vortex [Fie09], while larger values of $S_r$ lead to the vortex transitioning into a two-celled structure. Empirically, in the present work the Reynolds number is the parameter that most greatly influences the computation time. Consequently, it has been fixed to the highest value that allowed a reasonable computation time to reach steadiness, $R_e = 10000$. However, it is important to note that the use of an adaptive timestep based on the maximum velocities in

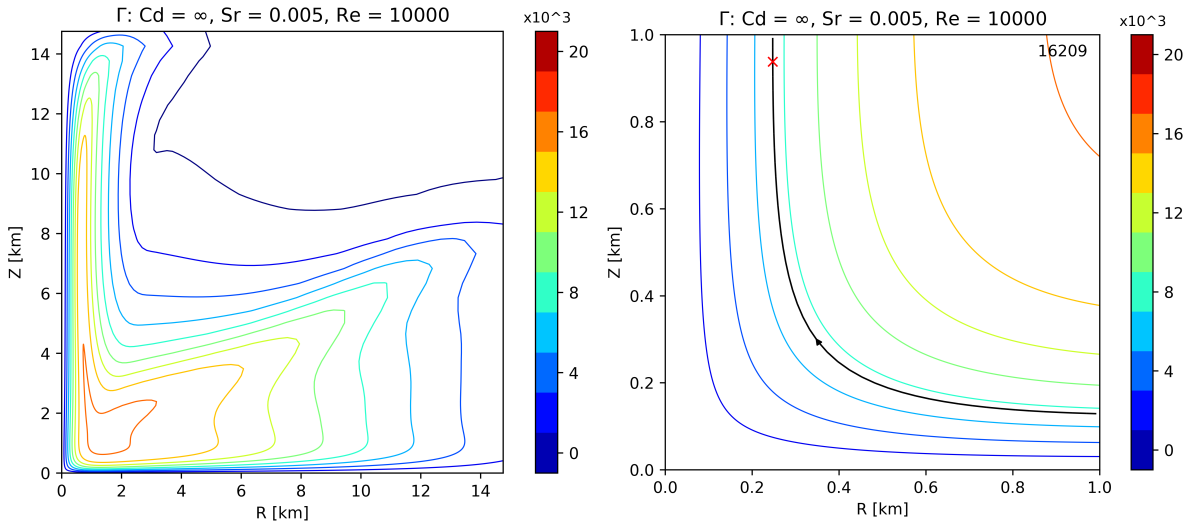


**Figure 4.3:** Angular momentum contourlines $[m^2/s]$ in a) the region [(0,0),(15,15)] of the domain, and b) window into the corner region [(0,0),(1,1)] for $S_r = 0.005$, $R_e = 10000$ and no-slip ($C_d = \infty$) boundary conditions. In the b panel, the red x is the position of the maximum tangential velocity, and the solid black line is the streamline referring to that position.

the simulation meant that the run time was case-dependent. Guided by this rationale, the parameters for the simulations have been chosen to lead to three different no-slip situations: a single-celled vortex ($S_r = 0.005$), a vortex very close to the transition to two-celled ($S_r = 0.01$), and a two-celled vortex ($S_r = 0.04$). A summary of all the parameter combinations employed in the simulations is provided in table 2.2; the no-slip cases are indicated by $C_d = \infty$.

### Potential vortex analysis for $S_r = 0.005$

Since the defining property of the potential vortex is that the angular momentum per unit mass (hereafter simply angular momentum) $\Gamma = rv$ is constant with $r$ (thus $v \propto 1/r$), let us start by examining $\Gamma$ for $S_r = 0.005$, the single-celled case. Strictly speaking, the angular momentum includes the contribution from the rotation of the domain $\Gamma = rv + \Omega r^2$, but once the simulation reaches a steady state $rv \gg \Omega r^2$, and we can consider $\Gamma = rv$. It is worth noting that the potential vortex is a theoretical concept, there is no quantitative criterion to verify a clear-cut region of the vortex where the $\Gamma = const$ property is satisfied. For the purpose of this work, we only need to identify a region where the potential vortex assumption is reasonably true, to direct the related analysis to this region. Figure 4.3a shows a region, roughly delimited by $1 \lesssim r \lesssim 4$ km and $1 \lesssim z \lesssim 2$ km, where the angular momentum remains nearly constant, hence we can

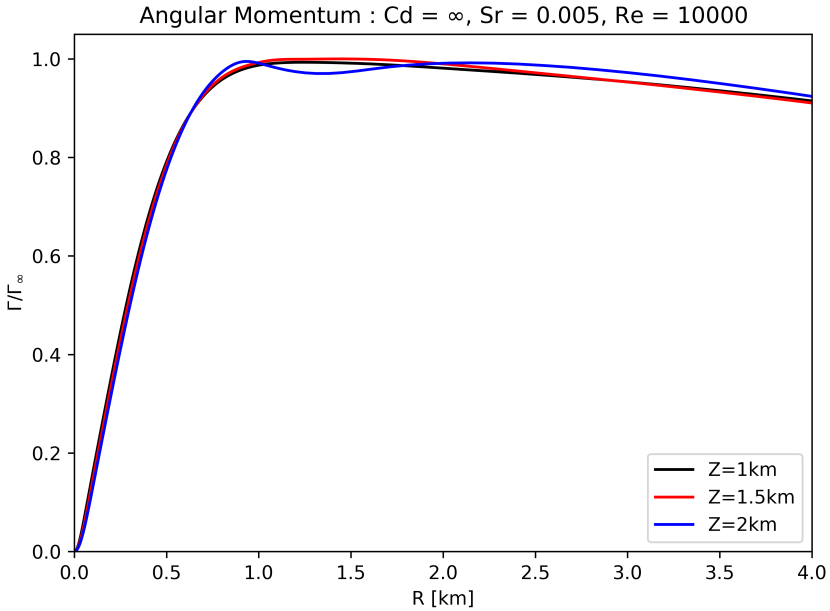


**Figure 4.4:** $S_r = 0.005$, $R_e = 10000$ and no-slip boundary conditions: radial profiles of $\Gamma$ normalized by $\Gamma_\infty$ sampled at three different heights.

refer to this region as the potential vortex region. For $r > 4$ km the assumption of constant $\Gamma$ slowly loses validity. The angular momentum goes to zero for $z \to 0$, due to the no-slip conditions. Figure 4.3b shows the windowed-in view of the $0 \leq r \leq 1$ km, $0 \leq z \leq 1$ km region. This area of the vortex is called the corner region. The windowed-in view clearly shows that $\Gamma$ goes to zero towards the no-slip boundary. The streamline that passes through the position of maximum tangential velocity illustrates how air flowing radially towards the origin is turned and redirected upwards.

We can further characterize the $\Gamma = const$ property analyzing the extension of the potential vortex area and quantifying the variation of $\Gamma$ across this region. Figure 4.4 shows the radial profiles of $\Gamma/\Gamma_\infty$ at various heights, where $\Gamma_\infty$ is the outer angular momentum, i.e. the maximum value of $\Gamma$ within the potential vortex region. Qualitatively, it is evident that there is an area, roughly delimited by $1 \lesssim r \lesssim 2$ km and $1 \lesssim z \lesssim 2$ km, where $\Gamma$ is nearly constant, and the assumption of potential vortex is fully satisfied. The profile sampled at $z = 2$ km shows a lesser degree of agreement, and the $\Gamma = const$ is degraded for $z > 2$ km (not shown). Therefore, we limit the region where we can safely assume that the potential vortex assumption is valid to $1 \lesssim z \lesssim 2$ km. For $2 \lesssim r \lesssim 4$ km the angular momentum tends to diminish, and the decrease becomes steeper for increasing $r$. It is worth pointing out the similarity of the $z = 1$ km and $z = 1.5$ km radial profiles. This confirms that there exists a region where the potential vortex assumption holds very well. Quantitatively, $\Gamma(r = 1, z = 1.5) - \Gamma(r = 2, z = 1.5) = 0.0037 \cdot \Gamma_\infty$,

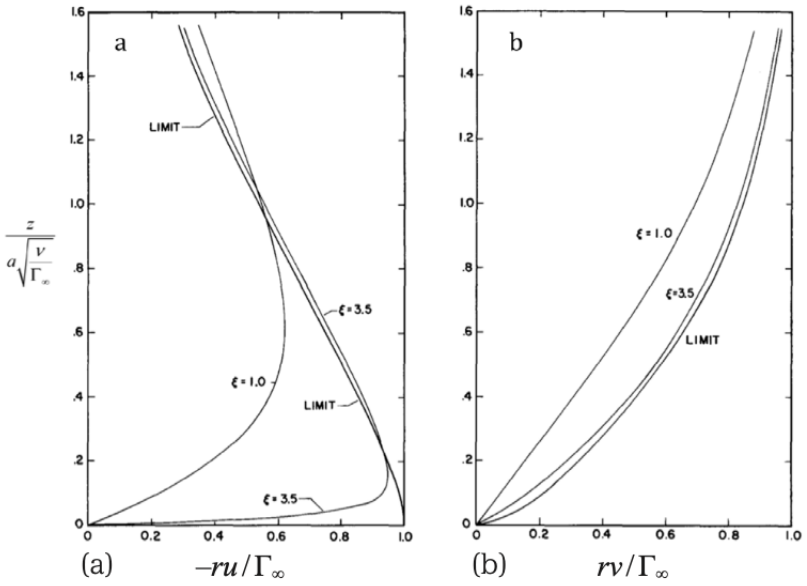


**Figure 4.5:** Boundary layer profiles of a) radial and b) tangential velocities for a potential vortex at different radii, along with the limit $r \to 0$ (for increasing $\xi$). (After [BSB71])

while $\Gamma(r = 1, z = 1.5) - \Gamma(r = 4, z = 1.5) = 0.087 \cdot \Gamma_\infty$. This shows that the model correctly simulates a potential vortex, and the property of constant $\Gamma$ only slowly loses validity with increasing $r$.

The boundary layer of a potential vortex has been found to display a two-tiered structure [BSB71]. The structure is usually visualized by plotting the $-ur/\Gamma_\infty$ and $vr/\Gamma_\infty$ vertical profiles sampled at various radii. Figure 4.5 (from [BSB71], who employ nondimensional coordinates, $a$ is the radial extension of the domain, $\nu$ the kinematic viscosity, and $\xi = -\ln(r/a)$, hence $\xi$ increases for decreasing radius) shows that $-ur/\Gamma_\infty$ increases from zero at $z = 0$ (due to the no-slip condition) to a maximum value at a given height, and then it decreases. The maximum magnitude of $-ur/\Gamma_\infty$ becomes larger and shifts downward as the radius decreases. As a result, the lower tier becomes vanishingly narrow and finally disappears in the limit $r \to 0$, leaving only the upper tier. $vr/\Gamma_\infty$ increases from zero to almost 1, the increase is faster for smaller radii. Figure 4.6 presents the same plots for $S_r = 0.005$. The results are in excellent agreement with those obtained in [BSB71]. The two-tiered structure is retrieved, and the lower tier becomes narrower for smaller $r$, while the maximum of $-ur/\Gamma_\infty$ increases. The plot of $vr/\Gamma_\infty$ well illustrates how the profile of $\Gamma$ tends to $\Gamma_\infty$ as $r$ decreases. There is one major difference with [BSB71]: the limit $r \to 0$ cannot be reached. As noted previously, the assumption of potential vortex does not hold in the corner region, so the potential vortex boundary layer is restricted to the region previously identified as the potential vortex region.

More can be said about the boundary layer of a potential vortex. For instance,

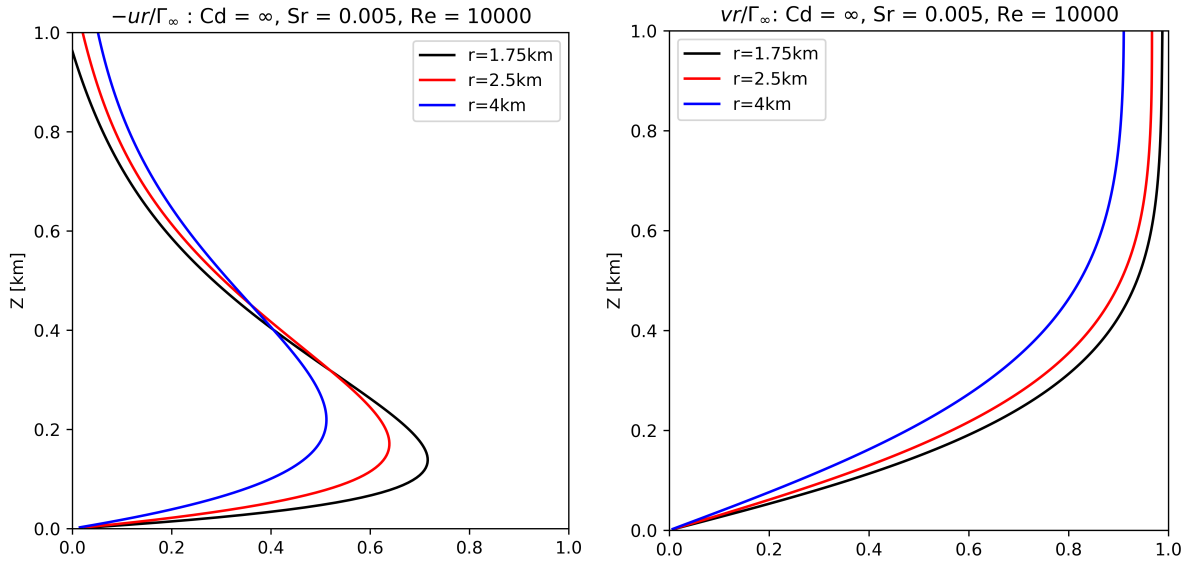


**(a)** **(b)**

**Figure 4.6:** $S_r = 0.005$, $R_e = 10000$ and no-slip boundary conditions: vertical profiles of a) $-ur/\Gamma_\infty$ and b) $vr/\Gamma_\infty$ for three radii.

considering the physical quantity called head

$$H = \frac{u^2}{2} + \frac{v^2}{2} + \frac{w^2}{2} + \phi, \tag{4.1}$$

the upper tier of the boundary layer has the property of having constant head over the depth of the boundary layer ([Rot14]), as expected for frictionless and steady-state conditions (the demostration of this statement is in Appendix 1). Moreover, according to boundary layer theory ([Bat00] chapter 5.7), the vertical variation of the radial pressure gradient $\frac{\partial \phi}{\partial r}$ is negligible and thus the pressure field is approximately uniform across the boundary layer. This behavior can be used to analytically retrieve the existence of an inflow in the boundary layer of the potential vortex. The radial pressure gradient is balanced by the centrifugal force in the inviscid region, hence the upper tier is in cyclostrophic balance, while, as the tangential velocity diminuishes approaching the surface, the pressure gradient is balanced by the vertical diffusion ([Rot13]):

$$\frac{\partial \phi}{\partial r} = \nu \frac{\partial^2 u}{\partial z^2}, \tag{4.2}$$

where $\nu$ is the kinematic viscosity. Since there is a central drop in pressure, $\frac{\partial \phi}{\partial r} > 0$, then $\frac{\partial^2 u}{\partial z^2} > 0$. Given that $u_{z=0} = 0$, the only possible solution is $u < 0$, as the solution

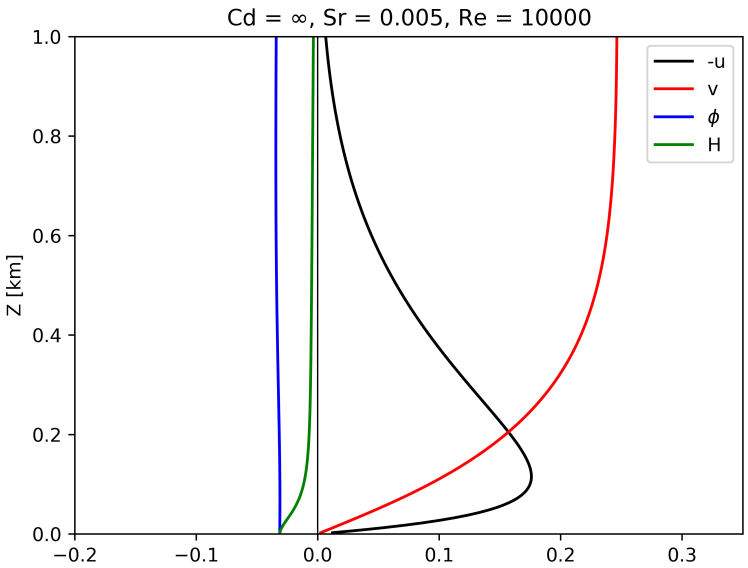


**Figure 4.7:** $S_r = 0.005$, $R_e = 10000$ and no-slip boundary conditions: vertical profiles at $r = 1$ km of $-u, v, H, \phi$. Velocities are normalized by the effective forcing velocity $W_e = 66$ m/s, $H$ and $\phi$ by $W_e^2$.

with $u > 0$ diverges for growing $z$. Using boundary layer theory we have retrieved the existence of an inflow in the boundary layer of the potential vortex.

Figure 4.7 displays the vertical profiles of $-u, v, H$, and $\phi$ at $r = 1$ km. At this radius, the pressure is clearly constant with height, while $H$ becomes constant above the maximum of $-u$, which indicates the starting point of the upper tier of the potential vortex boundary layer. Hence, the simulation correctly reproduces the boundary layer of a potential vortex. It is worth noting how $H = \phi$ at $z = 0$, as the wind speed is zero at the surface due to the no-slip condition. The cyclostrophic balance of the upper tier is retrieved in figure 4.8, which shows how the radial pressure gradient and the centrifugal force sum to zero at $z = 2$ km.

### Potential vortex analysis for $S_r = 0.01$

Moving to the $S_r = 0.01$ case, we note how the angular momentum configuration (figure 4.9) is very similar to the previous case. However, the area of maximum $\Gamma$ extends very close to the origin, penetrating the corner region (as can be seen in 4.9b). The streamline of figure 4.9b (solid black line) shows how the inflow can reach deeper in the corner region, and is forced to turn more tightly and closer to the origin. This behavior is in clear contrast to the smooth curve described by the streamline of the $S_r = 0.005$

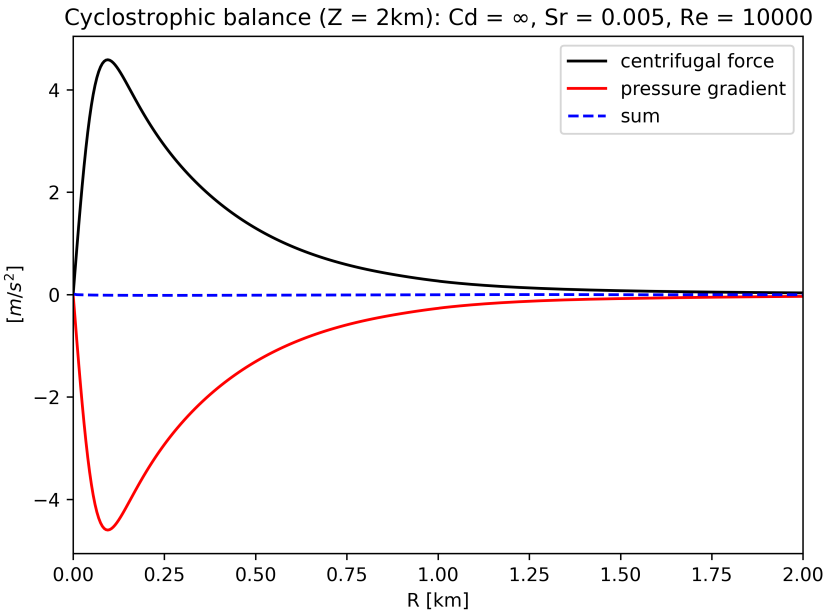


**Figure 4.8:** $S_r = 0.005$, $R_e = 10000$ and no-slip boundary conditions: radial profiles at $z = 2$ km of centrifugal acceleration (black), radial pressure gradient (red) and their sum (blue) $[m/s^2]$.

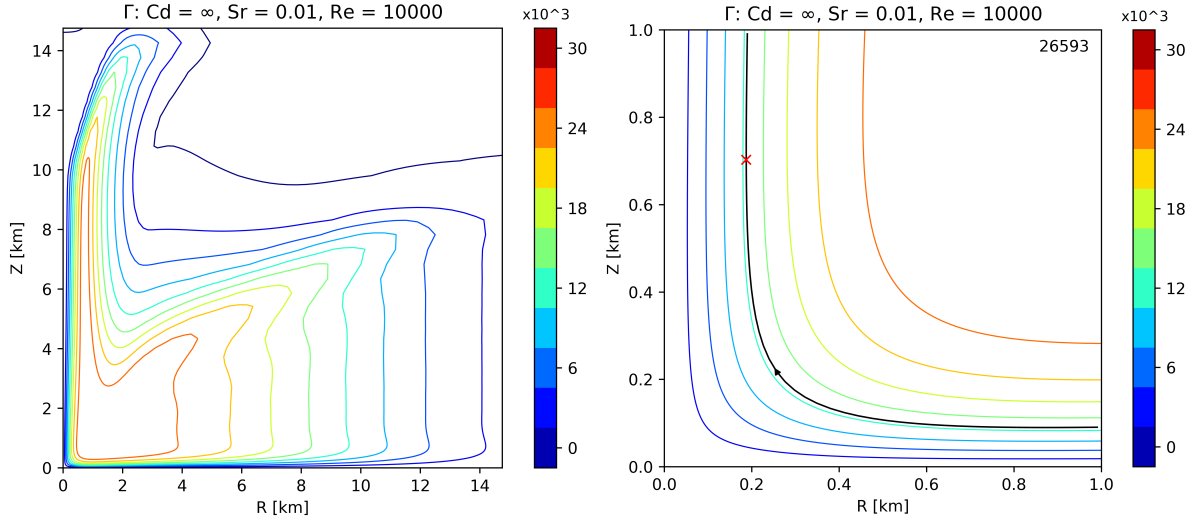


**(a)** **(b)**

**Figure 4.9:** Angular momentum contourlines $[m^2/s]$ in a) the region [(0,0),(15,15)] of the domain, and b) window into the corner region [(0,0),(1,1)] for $S_r = 0.01$, $R_e = 10000$ and no-slip ($C_d = \infty$) boundary conditions. In the b panel, the red x is the position of the maximum tangential velocity, and the solid black line is the streamline referring to that position.

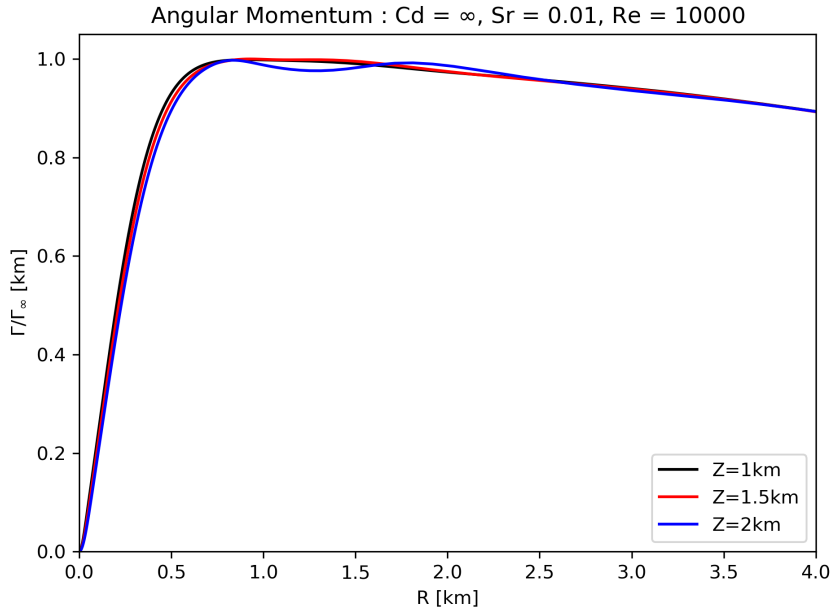


**Figure 4.10:** $S_r = 0.01$, $R_e = 10000$ and no-slip boundary conditions: radial profiles of $\Gamma$ normalized by $\Gamma_\infty$ sampled at three different heights.

case. The $\Gamma$ field indicates that for $S_r = 0.01$ the vortex is a more intense version of the single-celled vortex. The tightening of the structure seems to have enlarged the $\Gamma = const$ area, extending roughly from $1 \lesssim r \lesssim 4$ km and $1 \lesssim z \lesssim 3$ km.

Figure 4.10 shows the radial profiles of angular momentum sampled at different heights. The results are very similar to the ones of $S_r = 0.005$, with $\Gamma$ almost constant from $r = 1$ km to $r = 2$ km, and then slowly diminishing up to $r = 4$. Quantitatively, $\Gamma(r = 1, z = 1.5) - \Gamma(r = 2, z = 1.5) = 0.026 \cdot \Gamma_\infty$, while $\Gamma(r = 1, z = 1.5) - \Gamma(r = 4, z = 1.5) = 0.11 \cdot \Gamma_\infty$.

The two-layered structure of the boundary layer is retrieved for $S_r = 0.01$ in figure 4.11, which cleary shows the lower layer becoming thinner for lower radius, while the maximum of $-ur/\Gamma_\infty$ grows larger. Interestingly, the lower tier seems to be narrower compared to the $S_r = 0.005$ case. As expected, $vr$ asymptotically reaches $\Gamma_\infty$, and the approximation is better for lower $r$. The behavior is in accordance with the one described in [BSB71] for a potential vortex. The same can be said relatively to the vertical profiles of $\phi$ and $H$ (figure 4.12a), as the former remains constant throughout the whole boundary layer, while the latter is approximately constant in the upper tier. Moreover, figure 4.12b clearly shows that the upper tier is in cyclostrophic balance.

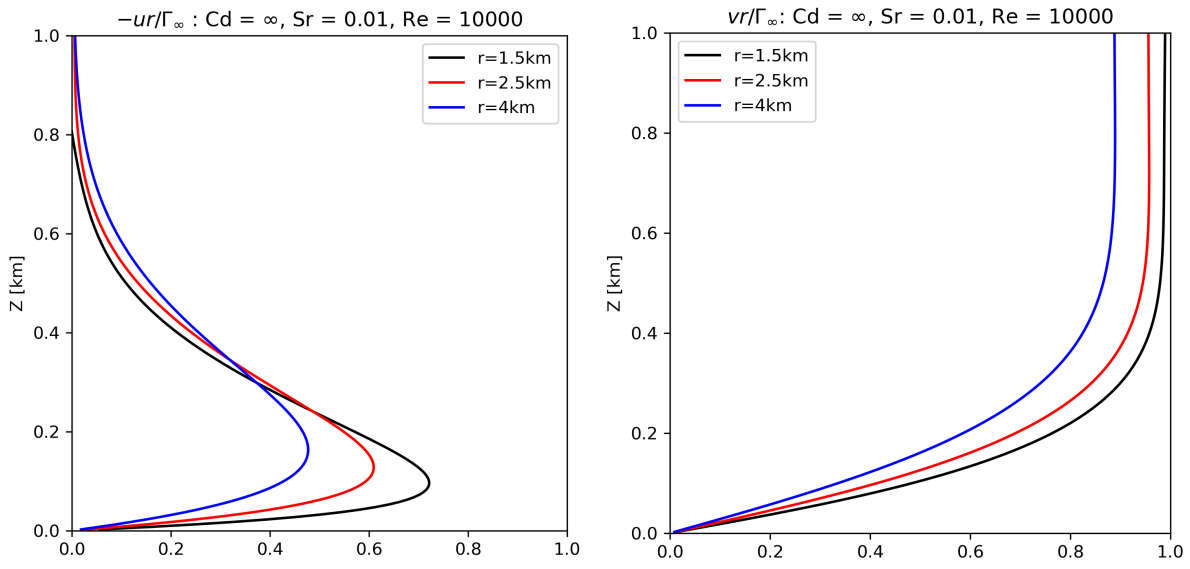


**(a)** **(b)**

**Figure 4.11:** $S_r = 0.01$, $R_e = 10000$ and no-slip boundary conditions: vertical profiles of a) $-ur/\Gamma_\infty$ and b) $vr/\Gamma_\infty$ for three radii.

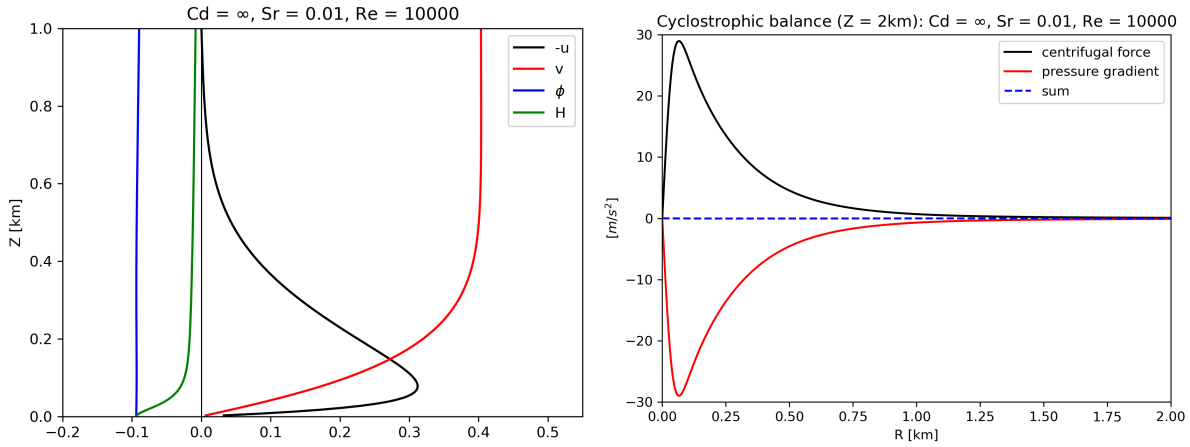


**(a)** **(b)**

**Figure 4.12:** $S_r = 0.01$, $R_e = 10000$ and no-slip boundary conditions: a) vertical profiles at $r = 1$ km of normalized $-u, v, H, \phi$ and b) radial profiles at $z = 2$ km of centrifugal acceleration (black), radial pressure gradient (red) and their sum (blue) $[m/s^2]$.

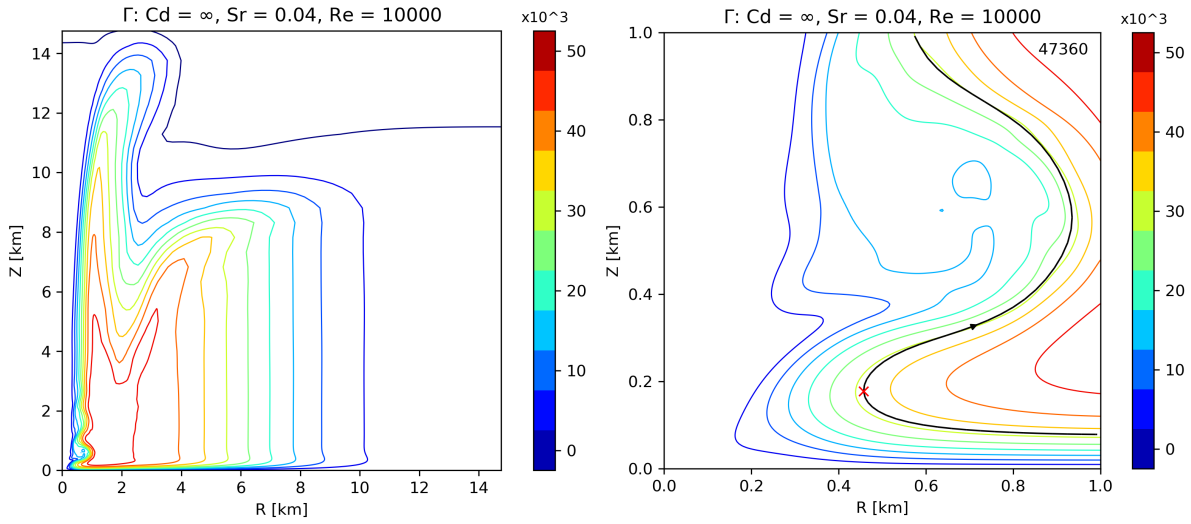


**(a)** **(b)**

**Figure 4.13:** Angular momentum contourlines $[m^2/s]$ in a) the region [(0,0),(15,15)] of the domain, and b) window into the corner region [(0,0),(1,1)] for $S_r = 0.04$, $R_e = 10000$ and no-slip ($C_d = \infty$) boundary conditions. In the b panel, the red x is the position of the maximum tangential velocity, and the solid black line is the streamline referring to that position.

### Potential vortex analysis for $S_r = 0.04$

The angular momentum field for $S_r = 0.04$ is evidently different from the previous two cases. Figure 4.13 shows that the region close to $r = 0$ has reduced angular momentum, a gap has formed between $r = 0$ and the vortex, a clear indication of the two-celled nature of the vortex. Furthermore, $\Gamma$ decays much more rapidly with $r$. It is, therefore, safe to assume that the potential vortex region is reduced in extent, and is now broadly found between $1 \lesssim r \lesssim 2$ km and $1 \lesssim z \lesssim 2$ km. The magnification of the corner region (figure 4.13b) emphasizes the differences with the previous one-celled vortices. There is a column of low $\Gamma$ for $r < 0.2$ km, and the vortex that follows is no longer narrow and vertically aligned. Instead, it forms a meandering vortex, with high $\Gamma$ wedging under a broad area of reduced angular momentum. The maximum tangential velocity is reached at a much lower height, and its streamline clearly shows the meandering.

The radial profiles of angular momentum, represented in figure 4.14, confirm that the decrease of $\Gamma$ is steeper for $r > 2.5$ km. There is still an area where the angular momentum is approximately constant between $r \sim 1$ and $r \sim 2$ km. Quantitatively, $\Gamma(r = 1, z = 1) - \Gamma(r = 2, z = 1) = 0.013 \cdot \Gamma_\infty$, $\Gamma(r = 1, z = 1) - \Gamma(r = 2.5, z = 1) = 0.063 \cdot \Gamma_\infty$, while $\Gamma(r = 1, z = 1) - \Gamma(r = 4, z = 1) = 0.171 \cdot \Gamma_\infty$ due to the steep decay of $\Gamma$. We observe that for $r < 1$ km the three profiles diverge, whereas for the one-celled vortex they appeared close to identical. This can be understood by noting

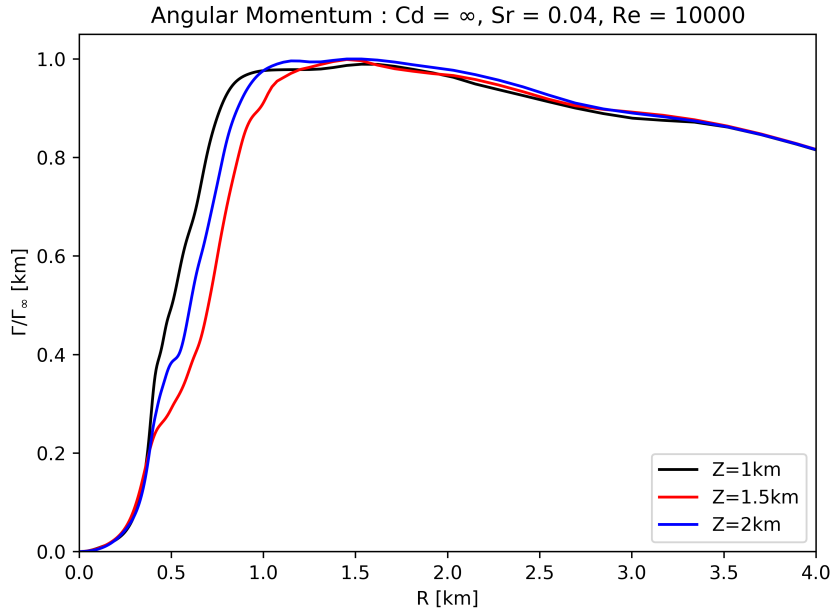


**Figure 4.14:** $S_r = 0.04$, $R_e = 10000$ and no-slip boundary conditions: radial profiles of $\Gamma$ normalized by $\Gamma_\infty$ sampled at three different heights.

how the corner region of the two-celled vortex is significantly less homogeneous vertically with respect to the single-cell case.

As can be seen from figure 4.15, the two-tier structure of the boundary layer is preserved for the two-celled vortex. The vertical profile of $-ur/\Gamma_\infty$ at $r = 2.5$ km shows a negative value above $z = 0.4$ km, indicating the presence of an outflow. Recalling that the angular momentum field showed a broad area of low $\Gamma$ above $z = 0.4$ km, this hints at the presence of a pattern of strong tangential winds and an inflow followed by weaker tangential flow and an outflow. The lower tier of the boundary layer profile is even narrower, which can be understood considering the narrow layer of strong $\Gamma$ previously discussed. It is worth remarking that despite the different vortex structure compared to previous cases, the plots of $-ur/\Gamma_\infty$ and $vr/\Gamma_\infty$ describe the same situation, with a two-tiered profile for $-ur/\Gamma_\infty$ and an asymptotic behavior for $vr/\Gamma_\infty$. The same can be said for the dependence of the profiles on $r$: the lower tier gets thinner, the maximum of $-ur/\Gamma_\infty$ increases and $vr/\Gamma_\infty$ approximates $\Gamma_\infty$ better for decreasing radius. The narrowing of the lower tier is quantitatively confirmed by table 4.1, which presents the width of the lower layer for $r = 1.75$ km. The first column, showing the results for the three $S_r$ values under no-slip conditions, clearly evidences a progressive narrowing of the lower layer.

Further confirmation of the presence of a potential vortex boundary layer for $S_r = 0.04$ is provided by the vertical profiles at $r = 2$ km of $H$ and $\phi$, which agree with

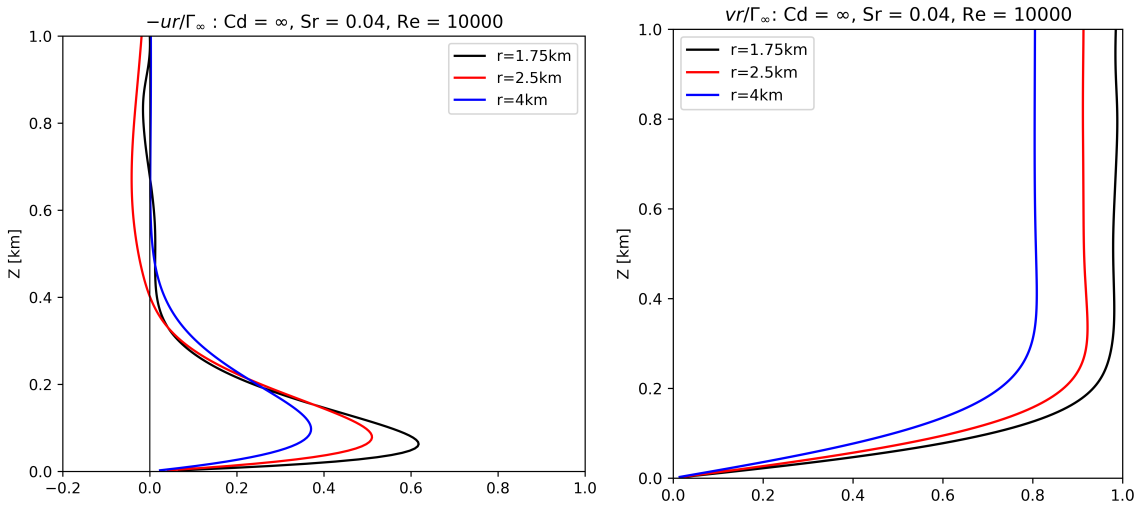


**(a)** **(b)**

**Figure 4.15:** $S_r = 0.04$, $R_e = 10000$ and no-slip boundary conditions: vertical profiles of a) $-ur/\Gamma_\infty$ and b) $vr/\Gamma_\infty$ for three radiuses.

the expected behaviors (figure 4.16a), as the pressure is constant in the whole depth of the boundary layer and the head is approximately unchanged in the upper-tier of the boundary layer. Finally, figure 4.16b shows that the potential vortex region is in cyclostrophic balance, with the radial profiles at $z = 2$ km of pressure gradient and centrifugal force summing to zero for $r > 1$ km. The balance is not valid for $r < 1$ km, but it should be emphasized that the cyclostrophic balance is prescribed for the upper tier of the potential vortex boundary layer, which was previously identified as ranging from $1 \lesssim r \lesssim 2$ km.

| | **No-Slip** | $\mathbf{C_d = 0.2}$ | $\mathbf{C_d = 0.05}$ | $\mathbf{C_d = 0.01}$ |
|---|---|---|---|---|
| $\mathbf{S_r = 0.005}$ | 0.1375 | 0.1275 | 0.1075 | 0.0525 |
| $\mathbf{S_r = 0.01}$ | 0.1025 | 0.0975 | 0.0825 | 0.0425 |
| $\mathbf{S_r = 0.04}$ | 0.0625 | 0.0625 | 0.0525 | 0.0275 |

**Table 4.1:** Thickness of the boundary layer lower tier [km] at $r = 1.75$ km for $S_r = 0.005$, 0.01, 0.04 under no-slip conditions and semi-slip conditions with $C_d = 0.2$, 0.05, 0.01.

### Vortex structure for $S_r = 0.005$, $S_r = 0.01$, and $S_r = 0.04$

Having introduced the typical analysis related to potential vortex boundary layers, and having shown that all the present no-slip simulations include a region of potential vortex,

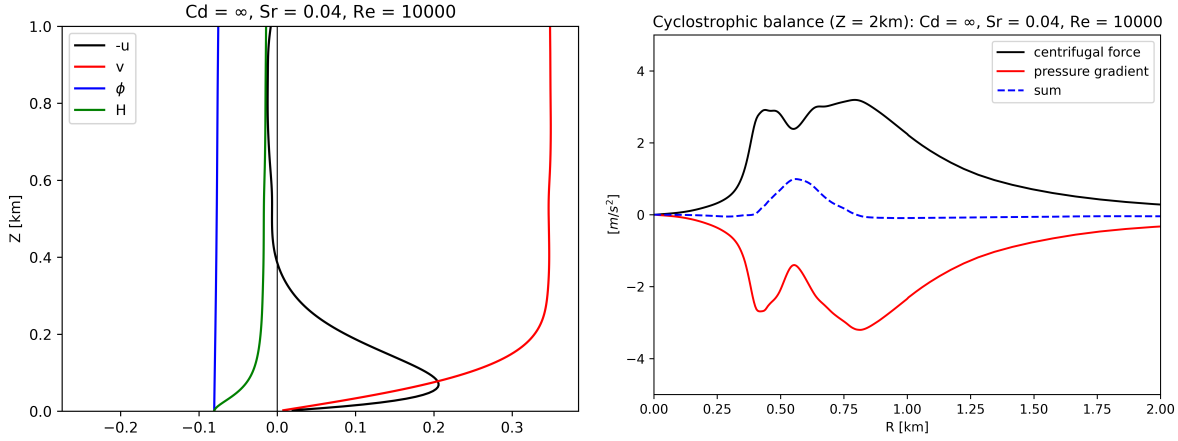


**(a)** **(b)**

**Figure 4.16:** $S_r = 0.04$, $R_e = 10000$ and no-slip boundary conditions: a) vertical profiles at $r = 2$ km of normalized $-u, v, H, \phi$ and b) radial profiles at $z = 2$ km of centrifugal acceleration (black), radial pressure gradient (red) and their sum (blue) $[m/s^2]$.

we proceed to describe how the different kinds of vortices appear in the present work, making use of the outputs of the no-slip simulations previously studied. The structure of the single-celled vortex for $S_r = 0.005$ is presented in figure 4.17. For the remainder of this work, a number in the top-right corner of a plot indicates the extremum of the field in the region of the domain being investigated. In particular, for $w$ it represents the maximum updraft velocity, while for $u$ it represents the maximum inflow velocity (inward, therefore with a negative sign). The tangential flow describes a narrow and elongated vortex. The single-celled nature of the vortex is clear looking at the central updraft, with no downdraft present. The pressure drop is also located at $r = 0$, and is maximum above the surface, resulting in a small radial pressure gradient for $z = 0$. Additionally, the inflow is broad and relatively weak, and the maximum tangential velocity is reached quite high above the surface.

Figure 4.18 shows the structure of the vortex for $S_r = 0.01$. For this value of swirl ratio, the vortex is single-celled and extremely close to the transition, therefore this vortex is almost the strongest single-celled vortex achievable for $R_e = 10000$. We note that compared to the situation for $S_r = 0.005$, the vortex has strengthened significantly, but the overall structure remains the same. There is still a central updraft, but this has intensified substantially, with the maximum vertical velocity more than doubled. The pressure drop too has deepened considerably, while remaining close to $r = 0$. There is still only a small radial pressure gradient for $z = 0$, apart from a slightly larger component for $r < 0.75$ km. The inflow is stronger and closer to the origin. Interestingly, the inflow occupies approximately the same area as for $S_r = 0.005$, thus the gradients of radial velocity are stronger. The extrema of all the fields have moved towards the origin

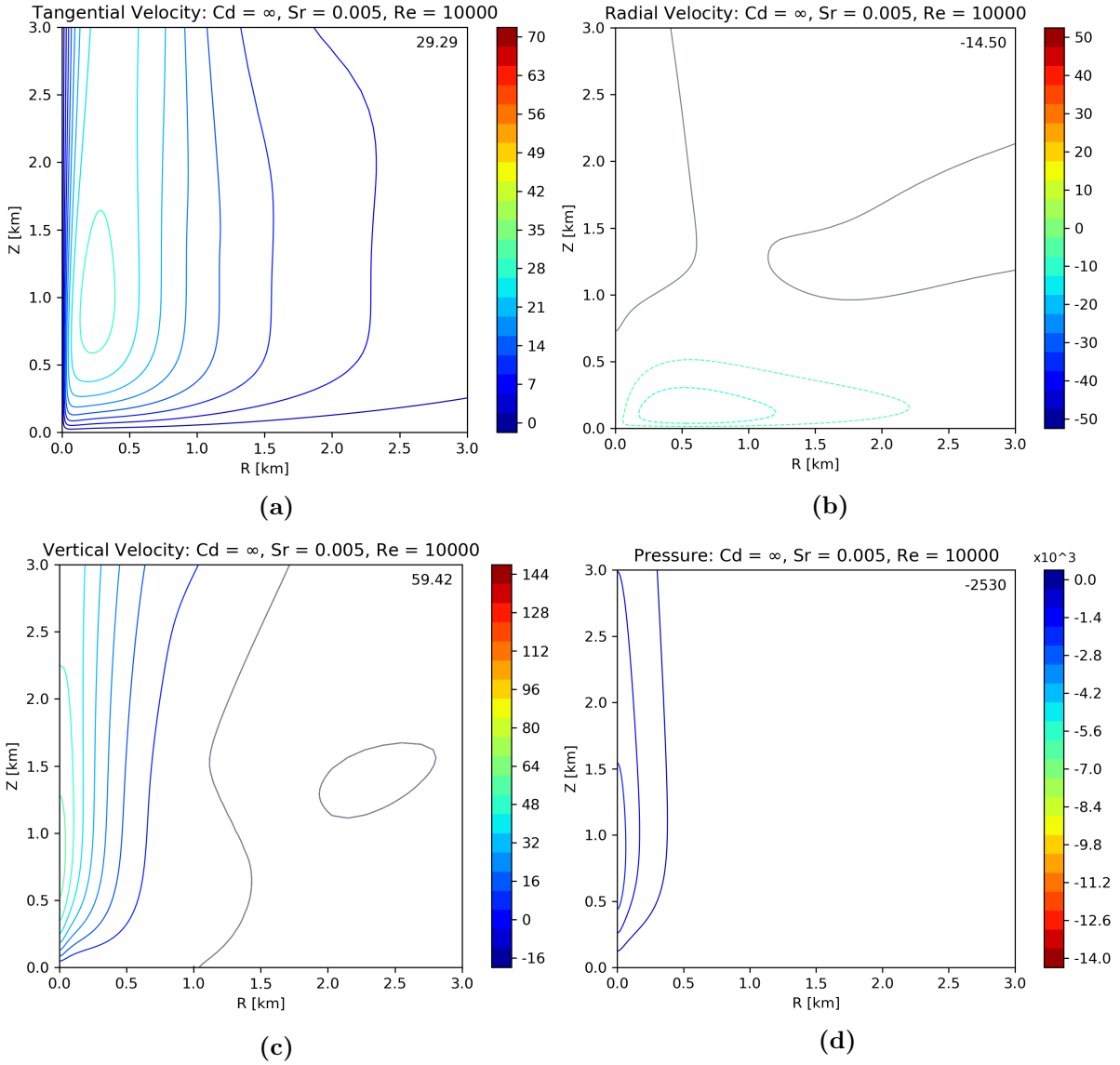


**Figure 4.17:** Contourlines of a) tangential, b) radial, c) vertical velocity [m/s], and d) pressure [Pa·$m^3$/kg] for $S_r = 0.005$, $R_e = 10000$ and no-slip ($C_d = \infty$) boundary conditions in the region [(0,0),(3,3)] of the domain. For the radial and vertical velocities the zero contourline is in grey.

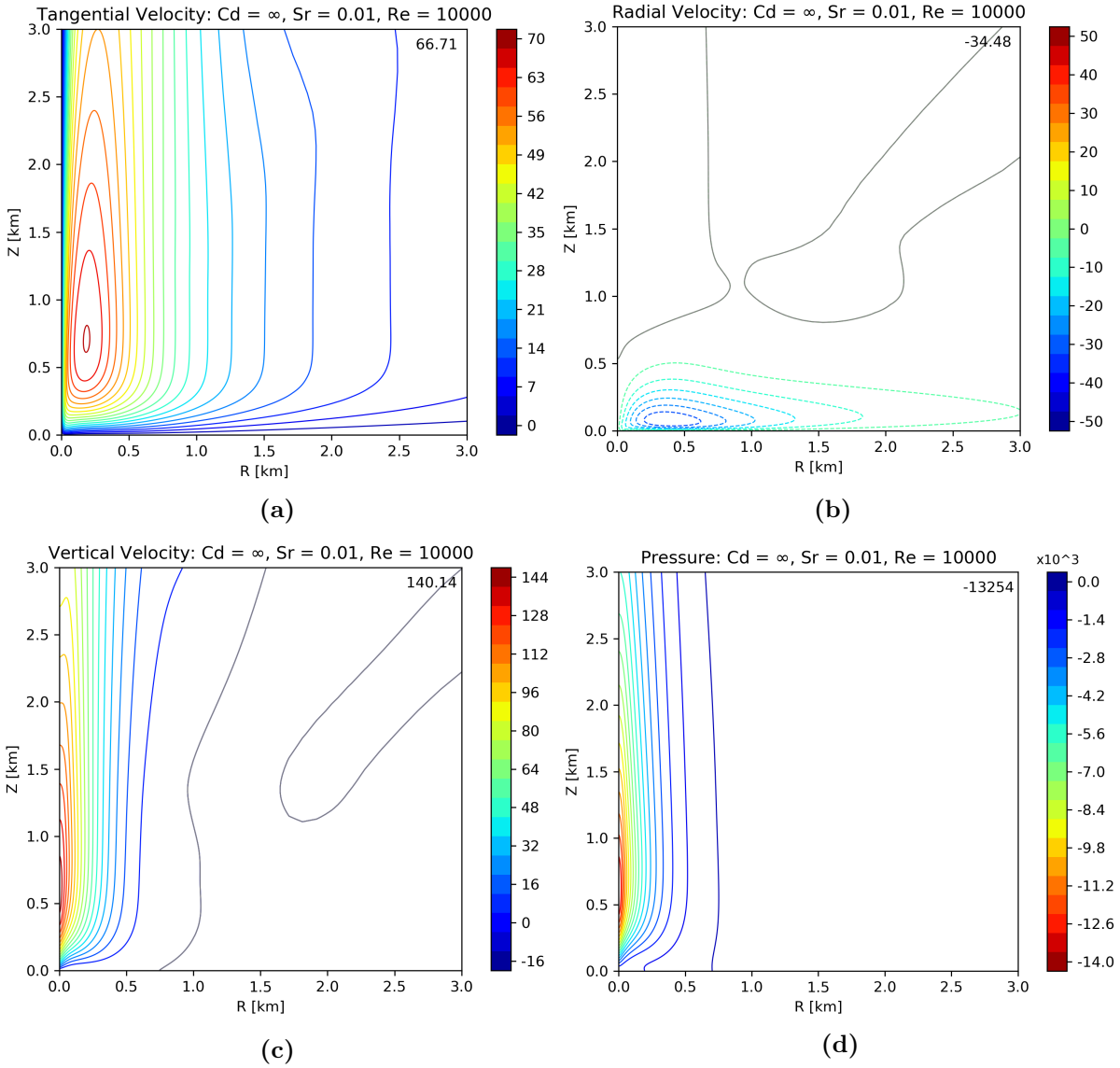


**Figure 4.18:** Contourlines of a) tangential, b) radial, c) vertical velocity [m/s], and d) pressure [Pa·$m^3$/kg] for $S_r = 0.01$, $R_e = 10000$ and no-slip ($C_d = \infty$) boundary conditions in the region [(0,0),(3,3)] of the domain. For the radial and vertical velocities the zero contourline is in grey.

compared to those of $S_r = 0.005$, indicating how the vortex strengthens while attaining a tighter structure.

Figure 4.19 shows that the structure of the two-celled vortex ($S_r = 0.04$) is substantially different from the single-celled one. The vortex presents a central downdraft, and the updraft has moved to larger $r$. Moreover, the updraft has dramatically weakened compared to the one found for $S_r = 0.01$, and the same can be said of the pressure drop. In particular, the pressure drop has transitioned from a slender and intense structure to a broader and weaker one, and now there is non-negligible radial pressure gradient at $z = 0$. The vortex is no longer steady, but rather statistically steady. Axisymmetric instabilities appear on the interface between the downdraft and the updraft. As a consequence of these instabilities and the interaction between the downdraft and the updraft, a pattern appears of regions with very strong tangential winds, followed vertically by zones of much calmer winds, and this pattern weakens with height. A similar pattern exists for radial velocity, with a vertical sequence of inflow and outflow areas. The tangential velocity field reveals a central area of calm winds. The inflow is significantly distorted by the instabilities, and its maximum occurs much further from the origin than in the $S_r = 0.01$ case. This distortion results in a considerably tighter inflow, leading to a higher maximum radial speed than in both previous cases. The drastic difference in updraft intensity is possibly caused by the fact that while for $S_r = 0.01$ the inflow is completely redirected upwards and fully contributes to the updraft, for $S_r = 0.04$ the inflow inverts the direction and becomes a powerful outflow, consequently only a modest fraction of the inflow contributes to the updraft. This simulation represents a vortex that has experienced a complete vortex breakdown. While the present work focuses on the asymptotic behavior of vortices, it is worth noting that the time evolution of this simulation (not shown) shows a central downdraft making its way downwards, and when it reaches the surface, instabilities suddenly appear, and the vortex loses its steadiness (while still being statistically stationary).

### Comparison of the no-slip simulations with previous reseach

We conclude the analysis of the no-slip simulations by presenting the comparison with the analogous simulations of [Rot+16]. In their work, [Rot+16] include the extrema of $v, u$, and $\phi$. The velocities are normalized by $W_e$, while the pressure by $W_e^2$, where $W_e = 66$ m/s is the effective forcing velocity. The results of the comparison are organized in table 4.2. The present simulations show good agreement with those of [Rot+16], as expected considering that the present work utilizes their results as a starting point. This analysis validates the present study's model setup.

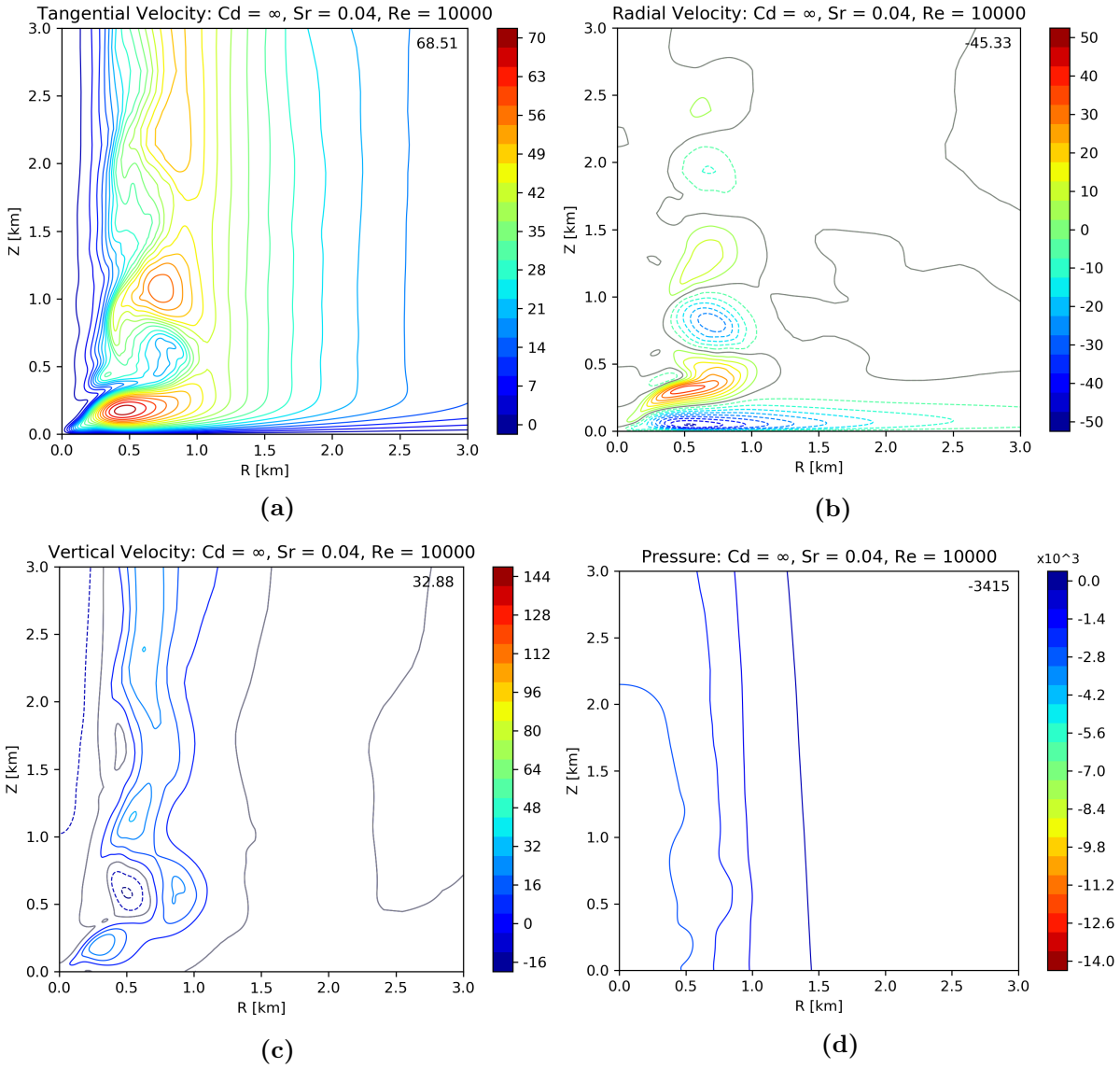


**Figure 4.19:** Contourlines of a) tangential, b) radial, c) vertical velocity [m/s], and d) pressure [Pa·$m^3$/kg] for $S_r = 0.04$, $R_e = 10000$ and no-slip ($C_d = \infty$) boundary conditions in the region [(0,0),(3,3)] of the domain. For the radial and vertical velocities the zero contourline is in grey.

| $\mathbf{S_r = 0.005}$ | **R16** | **Current** |
|---|---|---|
| $\frac{v}{W_e}$ | 0.50 | 0.44 |
| $\frac{w}{W_e}$ | 1.03 | 0.90 |
| $\frac{\phi}{W_e^2}$ | $-0.71$ | $-0.58$ |
| $\mathbf{S_r = 0.01}$ | **R16** | **Current** |
| $\frac{v}{W_e}$ | 1.03 | 1.01 |
| $\frac{w}{W_e}$ | 2.18 | 2.12 |
| $\frac{\phi}{W_e^2}$ | $-3.07$ | $-3.04$ |
| $\mathbf{S_r = 0.04}$ | **R16** | **Current** |
| $\frac{v}{W_e}$ | 1.05 | 1.04 |
| $\frac{w}{W_e}$ | 0.48 | 0.50 |
| $\frac{\phi}{W_e^2}$ | $-0.7$ | $-0.78$ |

**Table 4.2:** Comparison of the no-slip simulations. In the second row the results from [Rot+16], in the third row the results of the present work. Tangential and vertical speed are normalized by $W_e$, pressure is normalized by $W_e^2$.

### 4.1.3 Free-slip simulations

In the following sections, the effect of the semi-slip boundary conditions will be studied performing a series of simulations with friction coefficients ranging from very high to very low. In the limit for $C_d \to 0$ we expect the simulations to tend to the free-slip case. It is therefore crucial to examine the free-slip simulations for the three values of swirl ratio in order to have a reference when checking that the semi-slip simulations behave as expected as $C_d$ goes to zero.

Prior to describing the free-slip simulations, it is important to recall that the presence of boundary layer inflow is a direct consequence of the vertical diffusion and, therefore, of the action of some kind of friction (induced by the no-slip boundary condition). Consequently, we expect to find little to no boundary layer inflow for the free-slip cases. Indeed, this is the case, and the minimum values of $u$ shown in table 4.3 indicate the lack of boundary layer inflow for all three simulations.

Figure 4.20 displays the angular momentum, tangential, and vertical velocities, along with the pressure for $S_r = 0.005$. The structure of the vortex is completely different from its no-slip counterpart. In fact, the vortex now exhibits a two-celled nature, with a noticeable gap of low $\Gamma$ and $v$ between the central axis and the vortex, while a downdraft has appeared at the center of the vortex. The pressure appears to be radially constant where the gap of low $\Gamma$ is present. The maximum vertical velocity is significantly reduced, particularly in the low levels, owing to the lack of inflow. Moreover, the $v$ field shows an almost perfect vertical alignment. We note how, in clear contrast with the no-slip case,

the contours of $\Gamma$ intersect orthogonally with the horizontal axis. There is no variation of angular momentum or tangential velocity approaching the lower limit of the domain, as no boundary layer has developed.

A similar situation is found for $S_r = 0.01$ (figure 4.21) and $S_r = 0.04$ (figure 4.22). Both vortices are clearly two-celled, and it is evident how for increasing swirl ratio the vortex shifts to larger $r$, enlarging the central gap. This feature highlights better how the radial pressure gradient is constant in the gap (4.22d). It is remarkable how different values of swirl ratio, chosen specifically to produce different situations in the no-slip case, end up providing the same two-celled structure, with the only difference being the width of the inner cell. This hints at a simplification of the vortex structure due to the lack of a frictional boundary layer. This simplification is evident comparing the relatively featureless free-slip simulations with the more involved no-slip cases.

We conclude this section by highlighting how for low swirl ratio ($S_r = 0.005$) the maximum tangential velocity is higher in the free-slip case than in the no-slip one, while the opposite is true for intermediate ($S_r = 0.01$) and high ($S_r = 0.04$) swirl ratio. This behavior is consistent with the results of [Fie17] and [Rot13].

| | **v** | **u** | **w** | $\boldsymbol{\phi}$ |
|---|---|---|---|---|
| $\mathbf{S_r = 0.005}$ | 48.80 | −0.55 | 10.50 | −3268.96 |
| $\mathbf{S_r = 0.01}$ | 52.97 | −0.51 | 8.86 | −3139.67 |
| $\mathbf{S_r = 0.04}$ | 51.49 | −2.00 | 6.04 | −3228.10 |

**Table 4.3:** Extrema of $v, u, w$ ([m/s]) and $\phi$ [Pa·$m^3$/kg] for the free-slip simulations.

## 4.2 Maintenance of potential vortex boundary layer under semi-slip boundary conditions

In the present work, numerous values of friction coefficient have been utilized as semi-slip boundary conditions. These values span a wide range, from very high to very low friction coefficient, with the intention of simulating scenarios where the strongest friction coefficients behave almost as $C_d \to \infty$ i.e. no-slip, while the weakest friction coefficients behave almost as $C_d \to 0$ i.e. free-slip. All the $C_d$ values employed are shown in table 2.2. It is essential to verify that the introduction of a semi-slip approach does not disrupt the essential features of the potential-vortex boundary-layer solution. Therefore, we expect to retrieve the two-tiered potential vortex boundary layer, along with the constant vertical profiles of pressure and head, the latter being constant in the upper layer. Additionally, we anticipate that this structure will evolve going to lower values

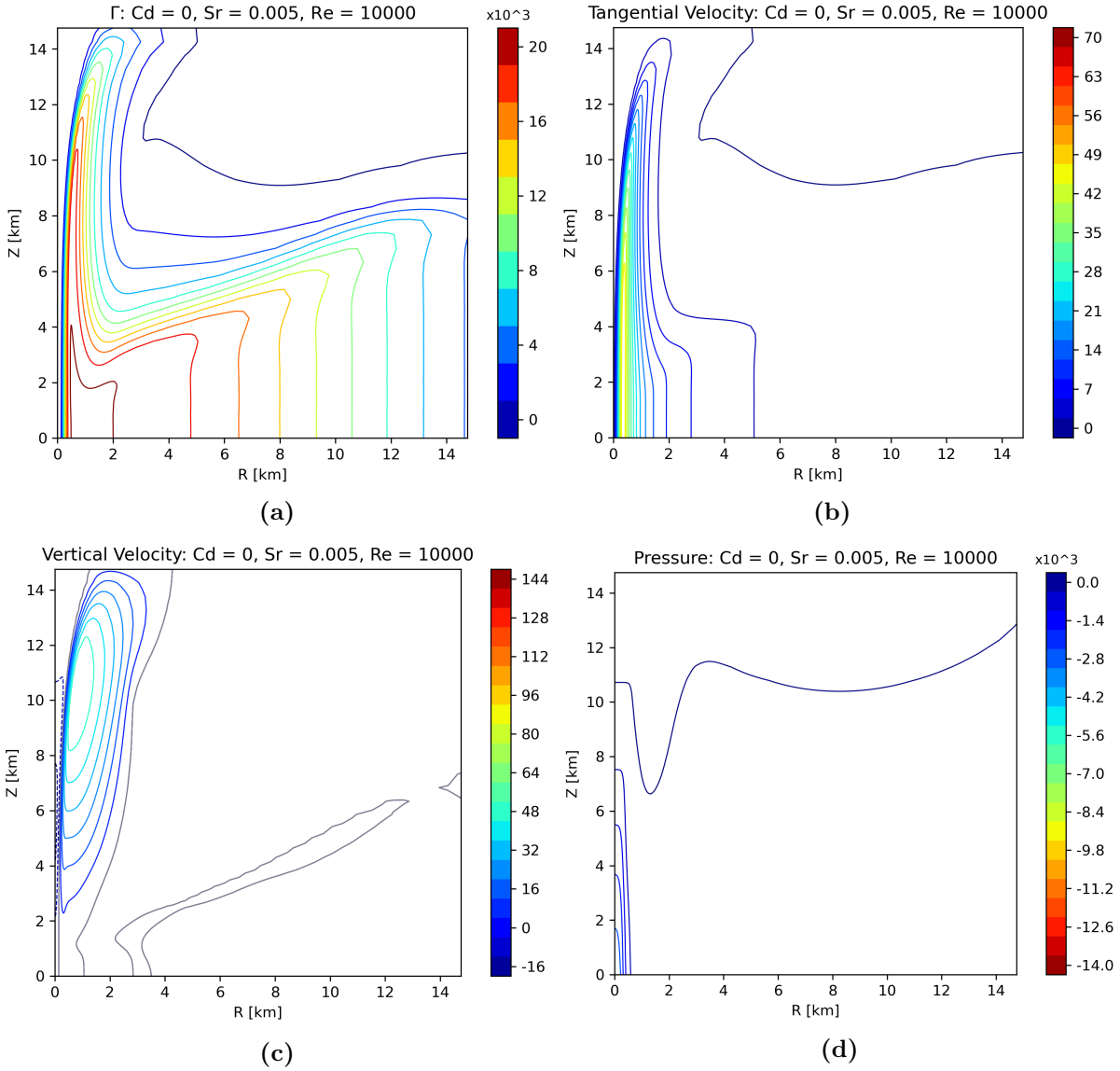


**Figure 4.20:** Contourlines of a) angular momentum, b) tangential velocity, c) vertical velocity and d) pressure for $S_r = 0.005$, $Re = 10000$ and free-slip ($C_d = 0$) boundary conditions. For the vertical velocity the zero contourline is in grey.

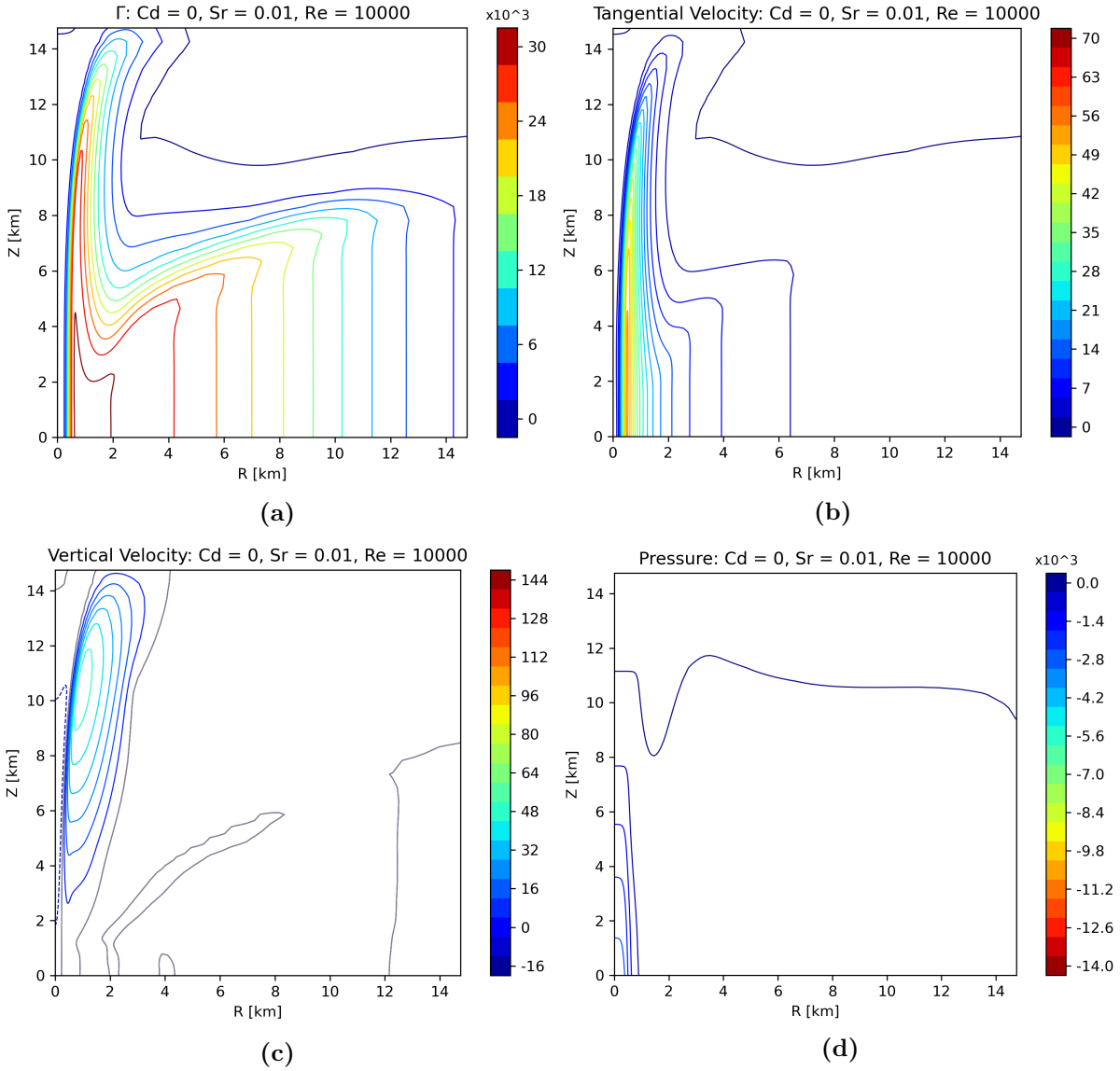


**Figure 4.21:** Contourlines of a) angular momentum, b) tangential velocity, c) vertical velocity and d) pressure for $S_r = 0.01$, $Re = 10000$ and free-slip ($C_d = 0$) boundary conditions. For the vertical velocity the zero contourline is in grey.

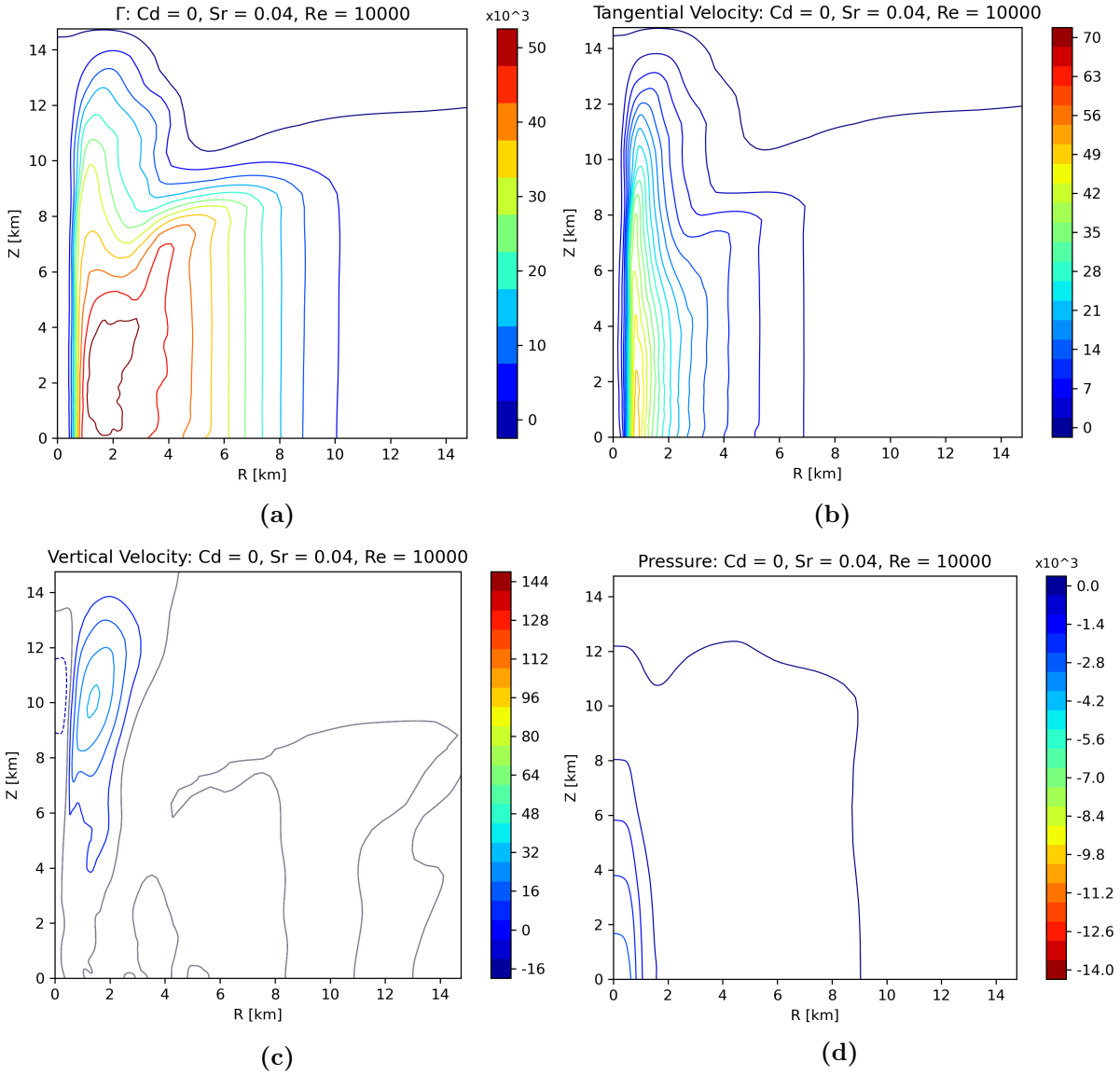


**Figure 4.22:** Contourlines of a) angular momentum, b) tangential velocity, c) vertical velocity and d) pressure for $S_r = 0.04$, $Re = 10000$ and free-slip ($C_d = 0$) boundary conditions. For the vertical velocity the zero contourline is in grey.

of $C_d$, and there will be a value below which the potential vortex boundary layer is no longer maintained.

**Maintenance of the potential vortex under semi-slip conditions for $S_r = 0.005$**

Figure 4.23 shows the vertical profiles of $-ur/\Gamma_\infty$ and $vr/\Gamma_\infty$ at $r = 1.75, 2.5$, and 4 km for simulations with $S_r = 0.005$ and semi-slip boundary conditions. Starting with the strongest friction coefficient employed in this work, i.e. $C_d = 0.2$ (figures 4.23a and 4.23b), it is evident that the radial velocity exhibits a two-tier structure. As the radius decreases, the lower layer becomes shallower, and the magnitude of $-ur$ increases. The vertical profiles of angular momentum display asymptotic growth, and the limiting value of $\Gamma_\infty$ is better approximated as $r$ diminishes. We remark how the highest value of $C_d$ employed causes only minor differences with respect to the corresponding no-slip boundary layer. Notably, the profiles do not start from zero at $z = 0$, whereas the no-slip conditions force $u$ and $v$ to be zero at the surface. Interestingly, the surface value of $-ur$ is significantly larger than the respective $vr$ value. In the corresponding no-slip simulation 4.17, it was observed that the maximum tangential velocity occurred at high levels, while the maximum inflow was found just above the surface. This observation can explain why a larger deviation from a surface value of zero is observed for $u$ compared to $v$. Overall, the profiles evidently describe the boundary layer of a potential vortex.

The boundary layer structure is likewise preserved for a moderate value of friction coefficient, $C_d = 0.05$ (figures 4.23c and 4.23d). The vertical profiles resemble those of the previous case, but we point out how the surface velocities have further increased. The comparison with the corresponding no-slip case highlights that the difference of $-ur/\Gamma_\infty$ between the top and the bottom of the lower layer has halved. Moreover, the thickness of the lower layer is marginally smaller compared to the previous value of friction coefficient, and the magnitude of the maximum is slightly reduced.

Figures 4.23e and 4.23f show the situation for the low-friction case of $C_d = 0.01$. The most striking feature is that the lower tier has become extremely shallow, with only a marginal difference between the top and the bottom of the layer. In fact, the surface values have further increased while the maximum of $-ur$ has decreased. Moreover, while the limiting values of $vr/\Gamma_\infty$ have remained nearly unchanged, the profiles start at around 50% of $\Gamma_\infty$. While these profiles still exhibit all the features characterizing the boundary layer of a potential vortex, it is easy to see how a further decrease in friction will cause the lower layer to vanish, while the profiles of $\Gamma$ will tend to become just vertical lines. Indeed, the lower tier becomes progressively shallower and finally disappears for $C_d = 0.001$. For this value of friction coefficient, the vortex is very similar to the free-slip case, with reduced inflow and updraft. Moreover, the vortex shows increased vertical homogeneity. This analysis shows that the potential vortex boundary layer is maintained over a wide range of $C_d$ values for a swirl ratio of $S_r = 0.005$.

Figure 4.24 presents the vertical profiles at $r = 1$ km of the normalized $-u, v, H$, and

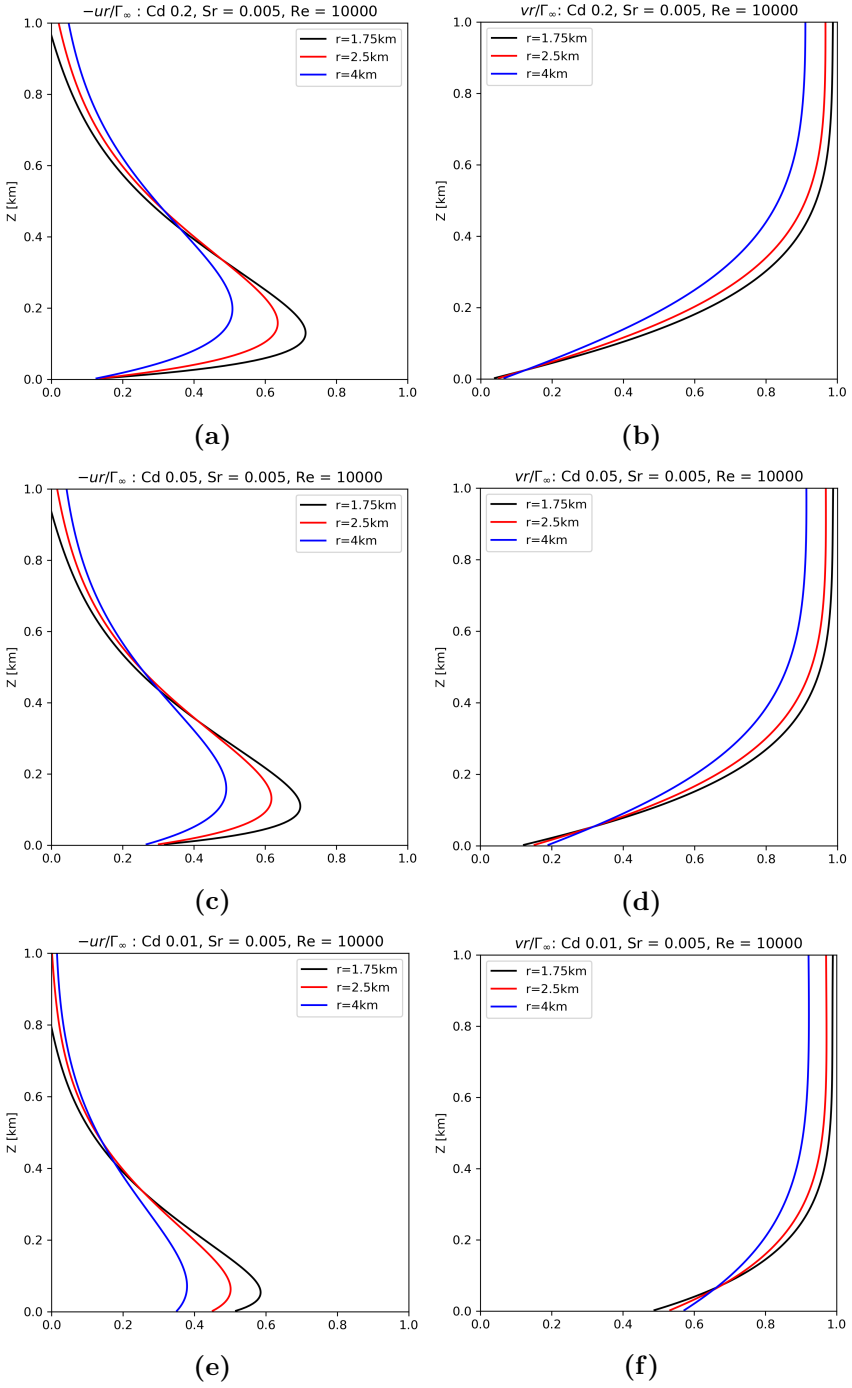


**Figure 4.23:** $S_r = 0.005$, $R_e = 10000$: vertical profiles of $-ur/\Gamma_\infty$ and $vr/\Gamma_\infty$ for three radii. a) and b) for $C_d = 0.2$, c) and d) for $C_d = 0.05$, e) and f) for $C_d = 0.01$ .

$\phi$ for $S_r = 0.005$ and the three values of $C_d$ from the previous plot. The similarity of the $C_d = 0.2$ profiles to those in the no-slip case is evident. The pressure is vertically invariant, while $H$ is nearly constant in the upper layer. The profiles for $C_d = 0.05$ also resemble the no-slip case, but it is easier to appreciate how $u$ and $v$ are non-zero at the surface; this is even more straightforward for $C_d = 0.01$, where the surface velocities are large enough to produce a noticeable difference between $\phi$ and $H$ at $z = 0$. We see again that even though the lower tier is exceptionally thin for $C_d = 0.01$, the situation still represents the boundary layer of a potential vortex. This analysis shows that the vertical profiles of $\phi$ and $H$ are in line with the expectations, confirming the maintenance of potential vortex boundary layer under semi-slip conditions for $Sr = 0.005$.

**Maintenance of the potential vortex under semi-slip conditions for $S_r = 0.01$**

The profiles of $-ur/\Gamma_\infty$ and $vr/\Gamma_\infty$ for $S_r = 0.01$ are presented in figure 4.25. For consistency, the same three values of friction coefficient have been analyzed throughout this section. Scanning figure 4.25 from top to bottom (diminishing $C_d$), we notice how the lower tier of the boundary layer becomes progressively shallower. This effect is further enhanced by the simultaneous increase of the surface value of $-ur$ and the decrease in magnitude of the maximum for decreasing $C_d$. The profiles of $vr/\Gamma_\infty$ display asymptotic growth, providing a better approximation of $\Gamma_\infty$ for smaller radii. The decrease of friction coefficient raises significantly the surface values of $vr$. Similar to the previous value of swirl ratio, it is remarkable how narrow the lower tier of the boundary layer becomes for $C_d = 0.01$. Moreover, $\Gamma$ reaches the asymptotic value from as low as 0.4 km. The profiles demonstrate how the potential vortex boundary layer is maintained under a wide range of friction coefficients even for a single-celled vortex whose no-slip case is very close to the transition to two-celled vortex. Indeed, the three simulations clearly show a two-layered vertical profile of $-ur$ and an asymptotic growth for $vr$, and the behavior for decreasing radius aligns with the expectations. As for $S_r = 0.005$, $C_d = 0.001$ exceeds the threshold value under which this structure is no longer preserved, and the vortex tends to exhibit free-slip features.

Figure 4.26 shows the vertical profiles of normalized head and pressure for $S_r = 0.01$ and semi-slip conditions, sampled at $r = 2$ km. The results are consistent with the development of a potential vortex boundary layer for all three values of friction, with $\phi$ being vertically constant, while $H$ nearly constant in the upper layer. As with the semi-slip $S_r = 0.005$ case, the decrease of $C_d$ gradually raises the surface values of $u$ and $v$. As for the corresponding low-swirl case, the head for $C_d = 0.01$ shows a non-negligible contribution of surface wind speed.

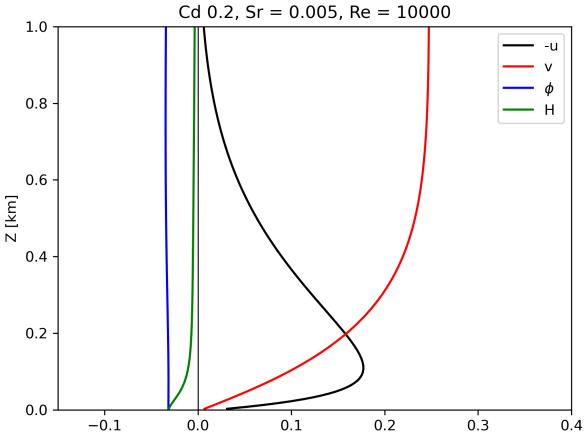


**(a)**

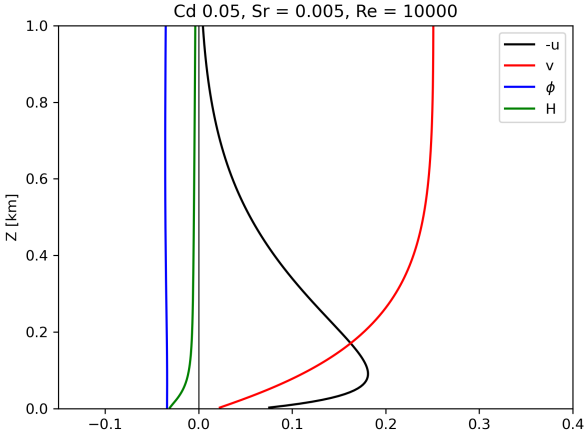


**(b)**

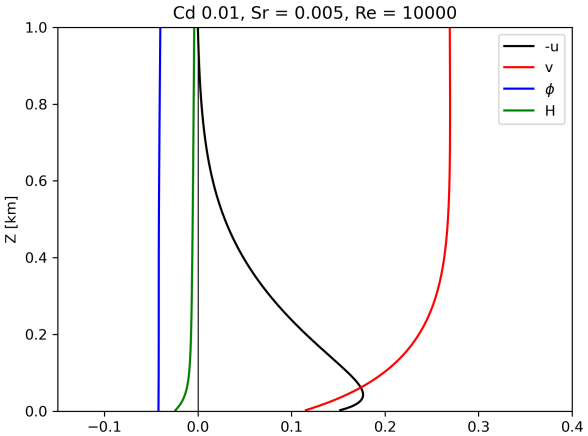


**(c)**

**Figure 4.24:** $S_r = 0.005$, $R_e = 10000$: vertical profiles at $r = 1$ km of normalized $-u, v, H, \phi$ for a) $C_d = 0.2$, b) $C_d = 0.05$, and c) $C_d = 0.01$ .

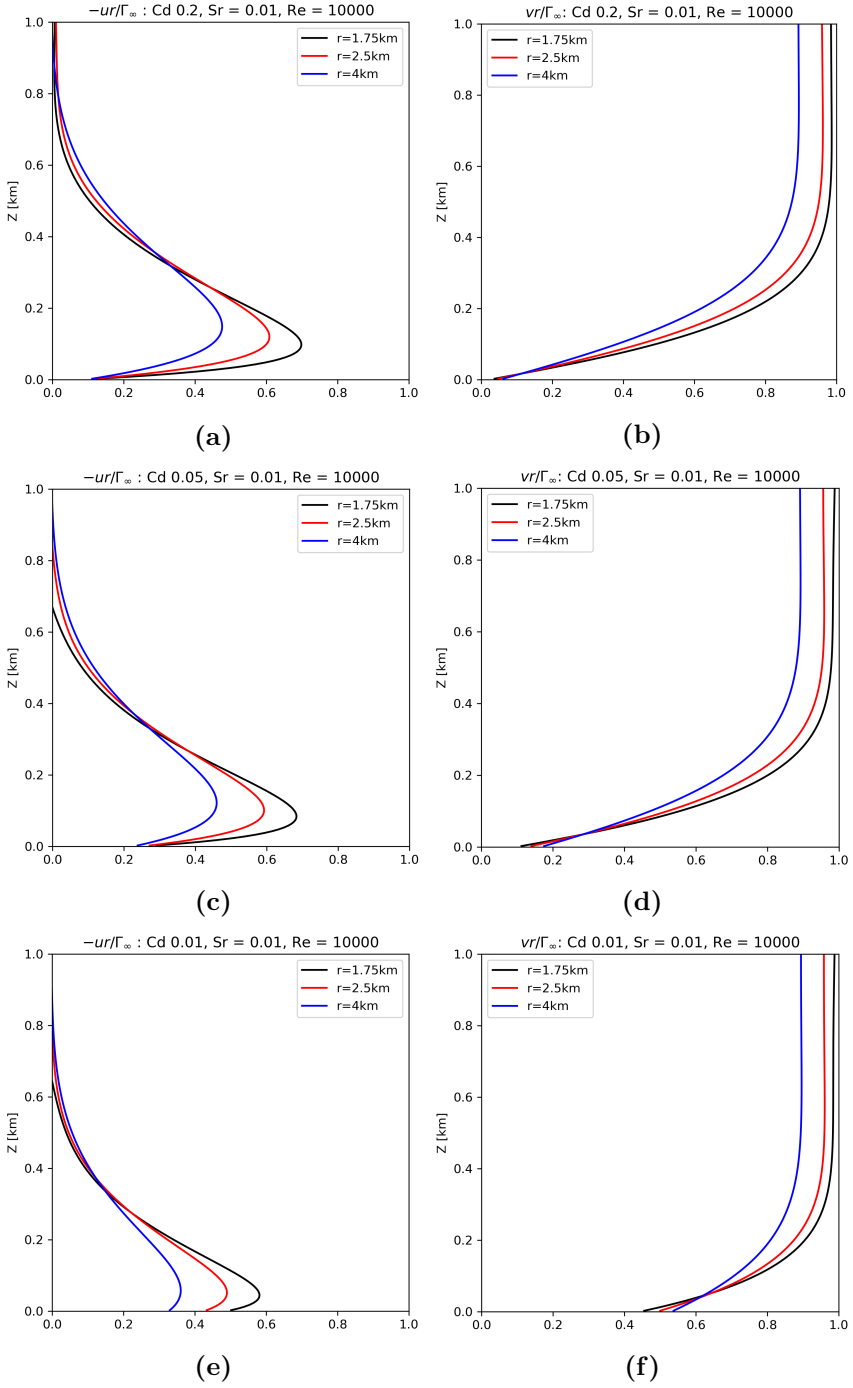


**Figure 4.25:** $S_r = 0.01$, $R_e = 10000$: vertical profiles of $-ur/\Gamma_\infty$ and $vr/\Gamma_\infty$ for three radii. a) and b) for $C_d = 0.2$, c) and d) for $C_d = 0.05$, e) and f) for $C_d = 0.01$ .

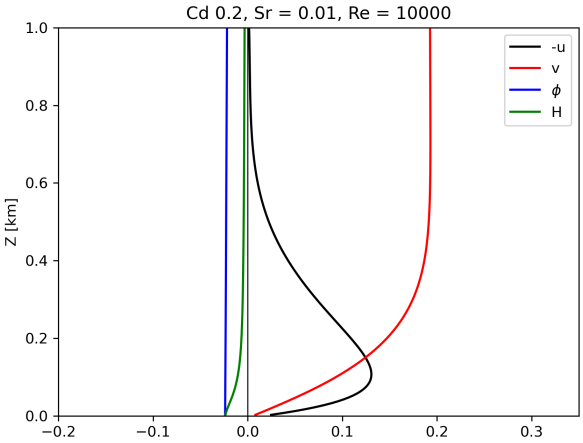


**(a)**

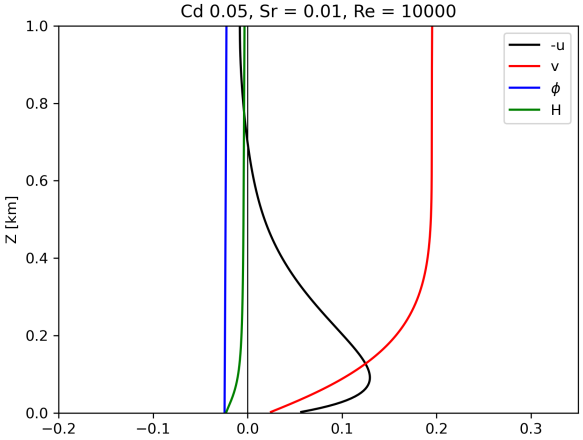


**(b)**

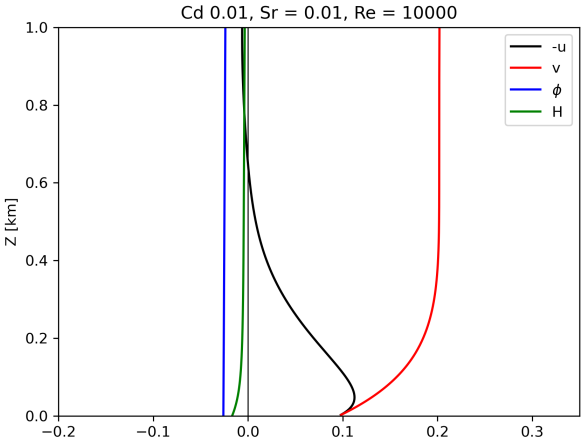


**(c)**

**Figure 4.26:** $S_r = 0.01$, $R_e = 10000$: vertical profiles at $r = 2$ km of normalized $-u, v, H, \phi$ for a) $C_d = 0.2$, b) $C_d = 0.05$, and c) $C_d = 0.01$ .

### Maintenance of the potential vortex under semi-slip conditions for $S_r = 0.04$

In section 4.1.2, studying the no-slip simulations, we noted how the lower tier of the boundary layer was markedly shallower for the two-celled vortex compared to the single-celled one. In light of this observation, it is especially important to investigate the effect of employing a semi-slip approach. Based on the previous analysis of the $S_r = 0.005$ and $S_r = 0.01$ semi-slip cases, it is clear that a decrease in $C_d$ causes the lower layer to become thinner, eventually disappearing for values of friction below a certain threshold. It is therefore important to investigate whether the potential vortex boundary layer is maintained for a narrower range of friction coefficients. Figure 4.27 shows the vertical profiles of radial and tangential velocities for various radii for $S_r = 0.04$. The $-ur/\Gamma_\infty$ profiles describe a two-tiered structure for all three values of $C_d$. We note that, similarly to the previous cases, the lower layer becomes shallower as friction decreases, with the surface values of $-ur$ increasing while the maximum values at the top of the layer diminish. For some values of $r$ and $z$ the radial velocity exhibits positive values, describing the presence of an outflow. This is akin to the respective no-slip case, for which it was found how the outflow was a consequence of the two-celled nature of the vortex. The profiles of $vr/\Gamma_\infty$ show the typical behavior of a potential vortex boundary layer, with $vr$ monotonically increasing to $\Gamma_\infty$. The behavior with decreasing radius for both radial and tangential velocities is in line with the theoretical results, as well as with the behavior of the corresponding no-slip case. Note how for $C_d = 0.01$ the lower layer is the shallowest of all the ones examined so far. While this would suggest that the threshold $C_d$ value could be lower for $Sr = 0.04$, the simulation with $C_d = 0.005$ still presents a two-tiered structure, and the first value of friction coefficient for which this structure is lost is once again $C_d = 0.001$.

The vertical profiles at $r = 2$ km of $\phi$ and $H$ describe a situation very similar to the previous two $S_r$ cases (figure 4.28). The pressure is constant with height, while the head is nearly constant above the maximum of $-u$, which marks the upper layer's lower edge. As for the previous cases, the increase in surface velocities gradually amplifies the difference between $\phi$ and $H$ at the surface.

### Final remarks on the role of semi-slip conditions on the potential vortex boundary layer

The results obtained indicate that a decrease in friction coefficient leads to a reduction in thickness of the lower tier of the boundary layer. This finding can be appreciated quantitatively in table 4.1, which displays the thickness of the boundary layer lower tier for the three values of swirl ratio and the $C_d$ values taken into consideration. Scanning the table along the rows, it is clear that a decrease in friction causes the lower layer to become thinner. In particular, for $C_d = 0.01$ the layer is remarkably thin, with a depth of only 27.5 meters for $S_r = 0.04$. Reading the table along the columns, we notice that

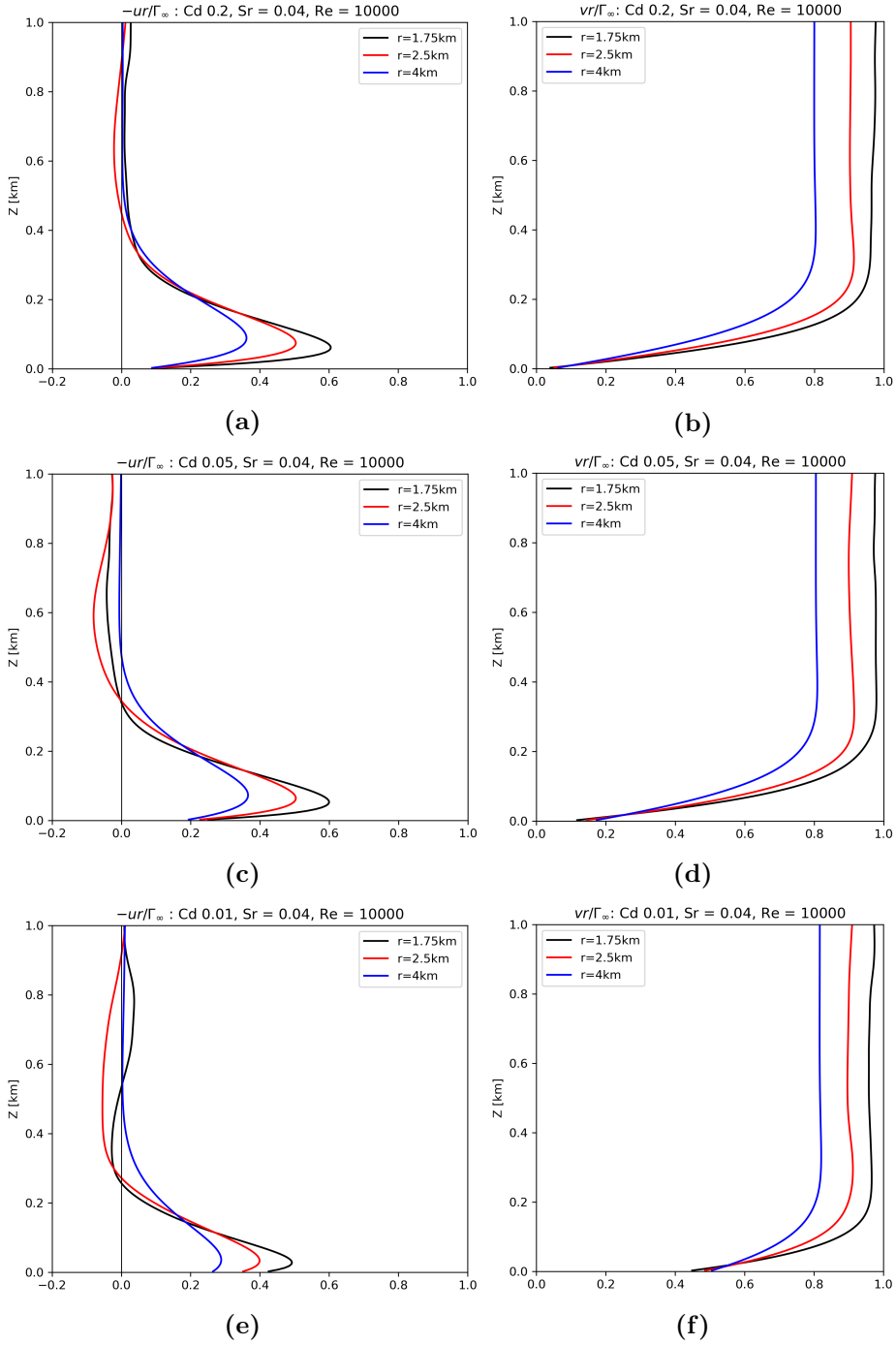


**Figure 4.27:** $S_r = 0.04$, $R_e = 10000$: vertical profiles of $-ur/\Gamma_\infty$ and $vr/\Gamma_\infty$ for three radii. a) and b) for $C_d = 0.2$, c) and d) for $C_d = 0.05$, e) and f) for $C_d = 0.01$ .

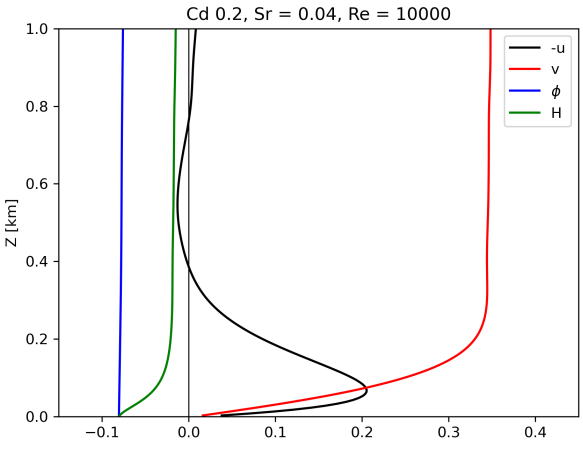


**(a)**

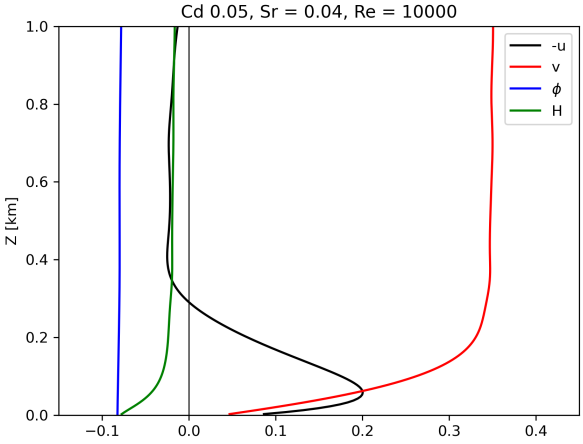


**(b)**

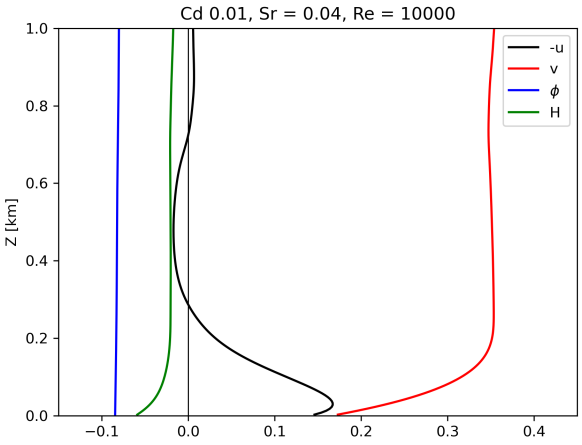


**(c)**

**Figure 4.28:** $S_r = 0.04$, $R_e = 10000$: vertical profiles at $r = 2$ km of normalized $-u, v, H, \phi$ for a) $C_d = 0.2$, b) $C_d = 0.05$, and c) $C_d = 0.01$ .

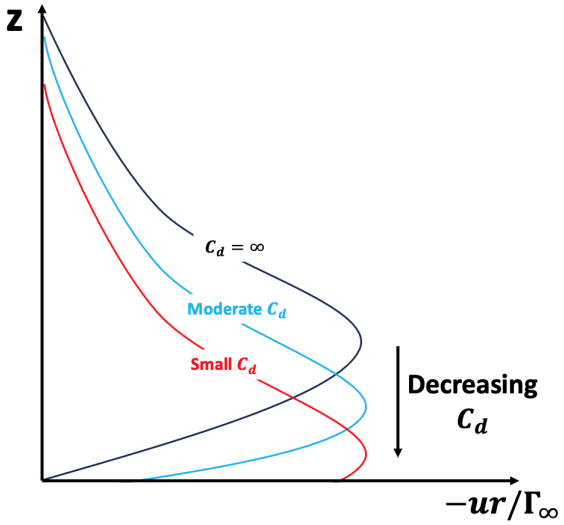


**Figure 4.29:** Schematic diagram of the role of decreasing friction on the lower tier of the boundary layer: the lower tier becomes narrower for diminishing $C_d$.

the lower layer tightens for increasing swirl ratio, as previously observed for the no-slip simulations.

A schematic diagram of the role of $C_d$ is presented in figure 4.29: a decrease in friction from no-slip conditions ($C_d = \infty$) reduces the thickness of the lower tier of the boundary layer, while simultaneously increasing the values of $-ur/\Gamma_\infty$ at the surface, until for very low friction the lower tier vanishes and the potential vortex boundary layer is no longer maintained.

This analysis demonstrates that the potential vortex boundary layer is preserved under semi-slip boundary conditions over a broad range of friction coefficients. The lower part of the boundary layer becomes narrower as friction decreases, ultimately vanishing below a threshold $C_d$, which in the present case falls between 0.005 and 0.001.

## 4.3 The role of the friction coefficient on the structure of the vortex

As previously mentioned, the structure of a potential vortex with no-slip boundary conditions depends on two parameters: the swirl ratio and the Reynolds number. This dependence has been thoroughly explored in [Rot+16]. They found out that the combination $S_r \propto R_e^{-1/3}$ yields an optimal vortex, defined as the combination for which the greatest pressure drop is simulated. They argued that the constant of proportionality may be dependent on the the specific details of the simulation (such as domain size,

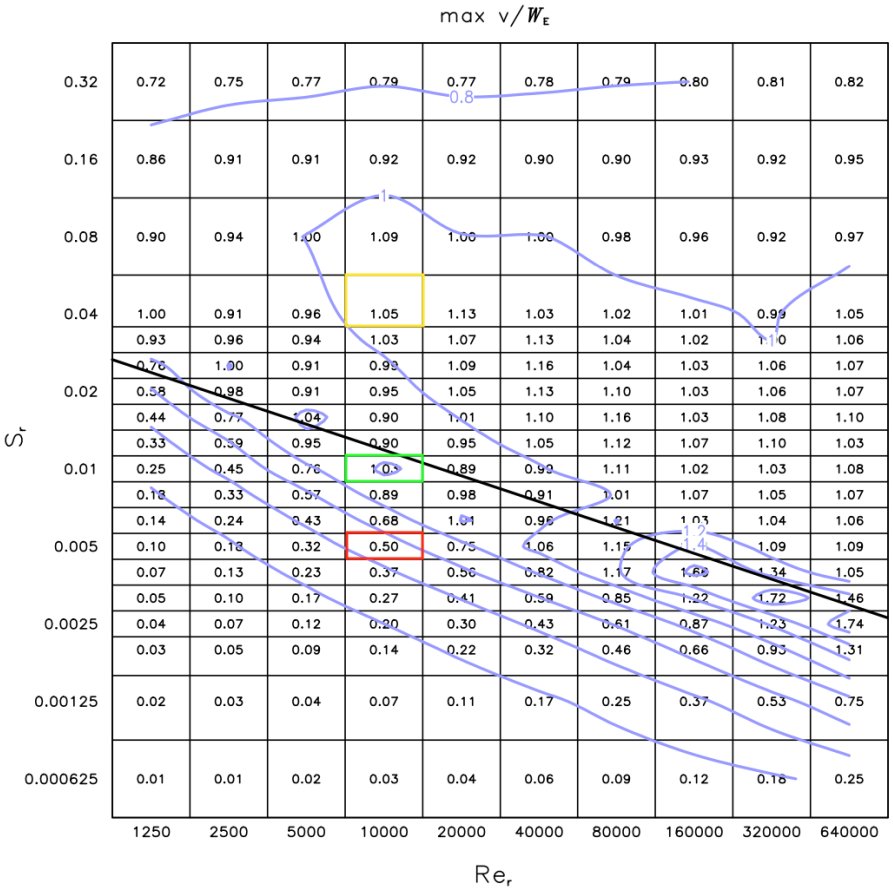


**Figure 4.30:** Solution matrix in $S_r - R_e$ space for the maximum tangential velocity, normalized by $W_e$. (After [Rot+16])

upper-layer damping, etc.), but the proportionality should be universal. On a log-log $S_r - R_e$ space, the proportionality appears as a diagonal line, with single-celled vortices below the line, whereas those above are two-celled solutions (figure 4.30). In the present work, the use of semi-slip boundary conditions introduces another parameter, the friction coefficient $C_d$. It is therefore natural to ask if this additional parameter plays a role in defining the nature of a vortex. We turn then our attention to investigating the effect of semi-slip boundary conditions on the structure of the vortex, examining the fields for a wide range of $C_d$ values. A summary of all the simulations performed is presented in table 2.2.

### The effect of $C_d$ on the structure of the vortex for $S_r = 0.005$

Before analyzing the simulations for $S_r = 0.005$, we note that figure 4.30 indicates that for $S_r = 0.005$ (red rectangle) the no-slip vortex is firmly below the line, hence it is a single-celled vortex far from vortex breakdown. This is in line with the findings in section 4.1.2.

Figure 4.31 shows the angular momentum in the corner region for various values of $C_d$, along with the position of the maximum tangential velocity, and the streamline passing through that point. Scanning the plot from left to right and from top to bottom, the friction coefficient employed in the simulations is progressively lower. The top row shows the no-slip (left) and $C_d = 0.1$ (middle) simulations. While it can be seen that the $\Gamma$ field shifts closer to the origin, and the maximum $v$ translates to a lower height, it is evident how for high friction ($C_d = 0.1$ is the second highest value used in this study) the situation is very similar to the no-slip case.

The next two panels, for $C_d = 0.05$ and $C_d = 0.035$, show that the angular momentum field shifts even closer to the origin. The maximum $v$ shifts significantly closer to the origin, and especially close to the $r = 0$ axis. These remarks hint at a progressive tightening of the vortex structure, with a more intense swirling motion close to the vertical axis. It is interesting to note how the streamlines perform a much tighter turn considerably closer to the origin, suggesting that the inflow penetrates deeper in the corner region.

With a minimal reduction of friction to $C_d = 0.03$, a peculiar feature emerges: a bulge of low $\Gamma$ is present in the upper part of the corner region. This feature can be understood by comparing it with the $C_d = 0.025$ case, where the gap of low $\Gamma$ reaches as low as 0.2 km. This suggests that the vortex is undergoing a vortex breakdown event, dividing it into a two-celled vortex above, and a single-celled one below. This hypothesis can be confirmed examining the vertical velocity field (figure 4.33), which clearly shows the central updraft abruptly transitioning to a downdraft near $z = 0.7$ km for $C_d = 0.03$, while this downdraft extends deeper for $C_d = 0.025$, reaching almost $z = 0.2$ km. The position of the maximum tangential velocity shifts even lower, reaching $z \approx 60$ m for $C_d = 0.025$. The streamline for $C_d = 0.03$ passes very close to the origin; it follows the inflow extremely close to the surface, makes a sharp turn upwards very near the origin, and then follows the updraft centrally until the vortex breakdown causes a deviation of the updraft. The streamline for $C_d = 0.025$ follows the inflow remaining at the lowest vertical grid point, before performing an exceptionally tight turn very near the origin. The increased shallowness of the inflow (figure 4.34) produces a strong radial flow at very low levels, while the extreme vertical pressure gradient (figure 4.35) causes the abrupt deviation of the streamline, directing it from the inflow into the updraft. The same behavior is observed for $C_d = 0.02$ and $C_d = 0.015$.

The vortex breakdown progressively descends for decreasing friction. The gap of low $\Gamma$ reaches very close to the lower boundary for $C_d = 0.02$, and it finally reaches the

surface for $C_d = 0.015$. For both friction values, the maximum of $v$ is strikingly close to the origin, with the minimum height above the surface of 12.5 meters for $C_d = 0.02$, which represents the third vertical grid point.

The last panel illustrates that the vortex is a fully-developed two-celled vortex for $C_d = 0.005$, as the gap has broadened significantly. The vertical gradient of angular momentum is sensibly reduced, and the contours of $\Gamma$ intersect with the lower boundary with values appreciably different from zero, indicating that the vortex is starting to show some free-sleep characteristics. Despite this, the streamline clearly shows the presence of an inflow. Comparing all the simulations, we note that as friction decreases, the contours of angular momentum gradually approach the horizontal axis, before eventually intersecting with it. With even lower friction, higher-valued contours intersect with the horizontal axis, due to the tendency of the $\Gamma$ field to become vertically aligned in the limit $C_d \to 0$.

The analysis of the angular momentum suggests that a decrease in friction coefficient for a vortex originally displaying a single-celled structure eventually leads to a vortex breakdown event. The breakdown splits the vortex into a two-celled region on top of a single-celled one, and the interface between the two regions moves downward for a further reduction in friction. When the vortex breakdown reaches the surface, the vortex exhibits a complete two-celled structure. It is remarkable how this behavior mirrors the transition from single-celled to two-celled vortex for increasing swirl ratio under no-slip conditions.

The tangential velocity field (figure 4.32) confirms that for high $C_d$ the semi-slip simulations behave similarly to the no-slip case. Indeed, the first two panels exhibit minimal differences, with the $v$ contours moving slightly closer to the origin, while the maximum intensifies. The successive two panels indicate that a further decrease in friction greatly enhances these differences. While the maximum rotational velocity has significantly intensified, the contours of $v$ have moved towards the vertical axis. This implies that the vortex has tightened while intensifying. Interestingly, the contours tend to distort towards the origin, where non-negligible values of tangential velocity are simulated. These observations help us understand the position shift of the maximum tangential velocity previously described.

The rotational velocity field for $C_d = 0.03$ clearly shows that the vortex is undergoing a vortex breakdown event. The strong and slender single-cell vortex suddenly transitions into a wider and weaker two-celled vortex near $z = 0.7$ km. The two-celled region progresses downward for $C_d = 0.025$. The vortex breakdown has sensibly constrained the single-cell section, which shows very high values of $v$. In fact, the maximum tangential velocity is nearly twice as intense as the no-slip case. The single-celled region of the vortex attains its smallest extension for $C_d = 0.02$, displaying an extremely slender shape. Due to the presence of the two-celled vortex, the contours of tangential velocities tilt outward.

Recalling that the optimal vortex is defined as the vortex that produces the strongest pressure drop while exhibiting a two-celled above/single-celled below structure ([Rot+16],

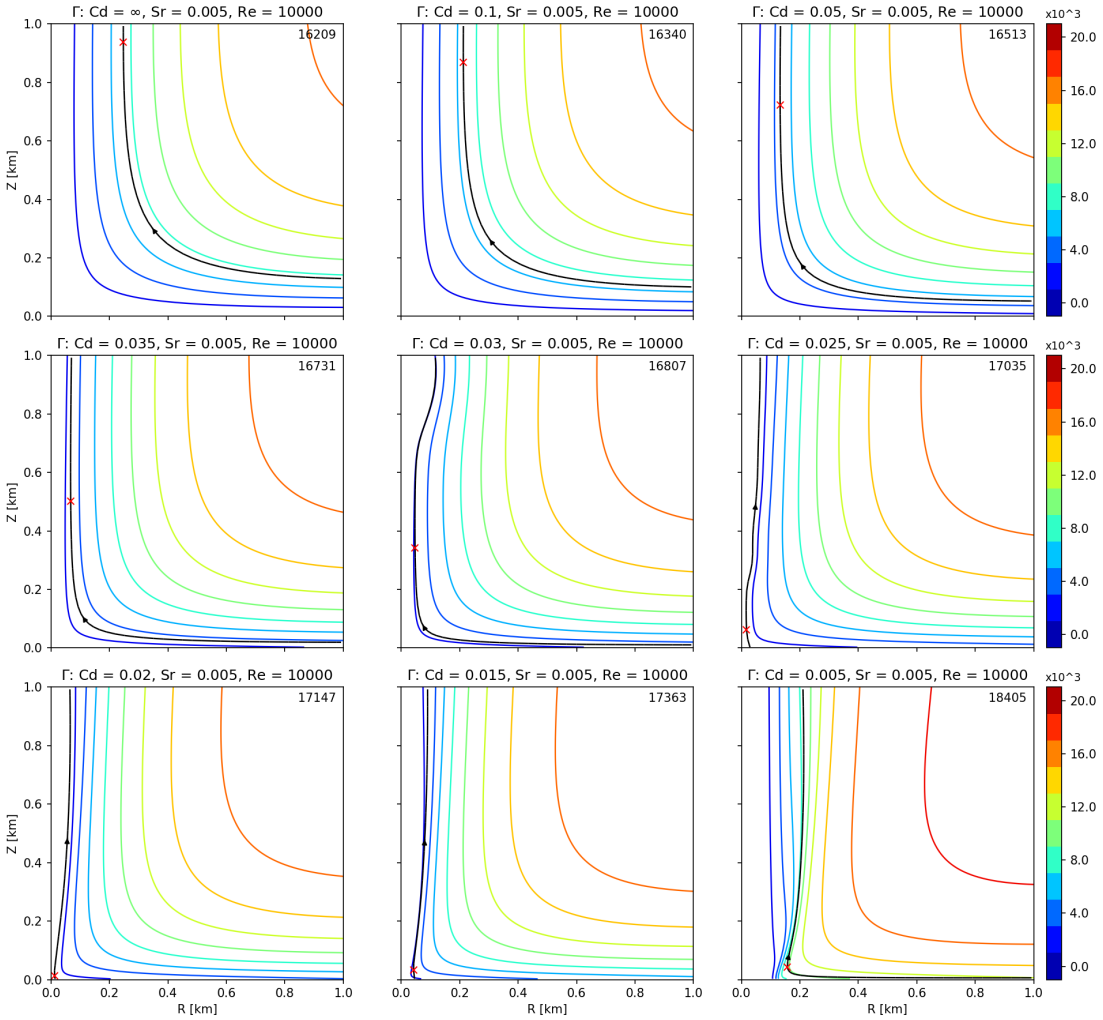


**Figure 4.31:** Angular momentum contourlines in the corner region $[(0,0),(1,1)]$ for $S_r = 0.005$, $R_e = 10000$ and semi-slip boundary conditions. The red x is the position of the maximum tangential velocity, and the solid black line is the streamline referring to that position. $C_d$ diminishes from left to right and from top to bottom.

[Rot13]), it is natural to ask if the vortices for $C_d = 0.03, 0.025, 0.02$ are optimal vortices. Examining the pressure field (figure 4.35), we note that the three simulations show the largest pressure drop, with $C_d = 0.025$ and $C_d = 0.02$ exhibiting particularly deep drops and similar values. With a peak in swirling velocity and pressure drop, along with their characteristic structure, the vortices for $C_d = 0.025$ and $C_d = 0.02$ appear to be optimal vortices. We remark how the occurrence of an optimal vortex for $C_d$ values just above the transition to two-celled structure is analogous to the occurrence of such vortices for swirl ratios just below the transition under no-slip conditions.

A further decrease in friction leads to a broadening of the vortex, in complete correspondence to the behavior of a two-celled vortex under increasing swirl ratio. Notably, both simulations for $C_d = 0.015$ and $C_d = 0.005$ show a slight increase in maximum tangential velocity. A possible explanation is that, since the maximum is found near the surface, a decrease in friction leads to an increase in velocity, until the vortex starts exhibiting free-slip features, after which the maximum tangential velocity diminishes towards the value of the free-slip case (table 4.3). It is not possible to verify this hypothesis at the present stage. However, it is noteworthy that for $C_d = 0.001$, the first value to produce a vortex with significant free-slip features, the maximum tangential velocity diminishes to 57.19 m/s (not shown).

Figure 4.33 shows the vertical velocity for $S_r = 0.005$ under semi-slip conditions. Once again, the situation for $C_d = 0.1$ is very similar to the no-slip case. The third and fourth panels show the updraft strongly intensifying while remaining central. Moreover, for decreasing $C_d$, the updraft starts at lower levels, as indicated by the contours stacking near the origin. As mentioned before, for $C_d = 0.03$ the solution undergoes a vortex breakdown, leading to the appearance of a downdraft that descends further as the friction coefficient decreases. For $C_d = 0.025$ the structure of the optimal vortex is clearly evident, with a strong, central updraft that abruptly deviates at the interface with the central downdraft, near $z = 0.2$ km. In contrast with the $v$ and $\phi$ field, where both the $C_d = 0.025$ and $C_d = 0.02$ simulations seemed to describe the structure of a potential vortex, the $w$ field for $C_d = 0.02$ indicates a weakening of the updraft. This can be understood considering the effect of the downdraft piercing downward. The vortex for $C_d = 0.025$ is therefore the optimal vortex.

The downdraft reaches the surface for $C_d = 0.015$, indicating that the vortex is two-celled for this friction coefficient. From theory, laboratory experiments, and simulations ([Rot13], [Chu+79], [Rot+16]), it is known that the transition to a two-celled structure significantly weakens a vortex's updraft. Therefore, the case for $C_d = 0.015$ describes a vortex that has just barely reached a two-celled structure, as demonstrated by the lack of weakening of the updraft. The weakening occurs for immediately lower values of friction, as shown in the last panel: the updraft of the simulation for $C_d = 0.005$ is severely weakened, the maximum being roughly half the value for $C_d = 0.015$

We can investigate the effect of semi-slip boundary conditions on the inflow of the vortex by examining the $u$ field (figure 4.34). We notice that for $C_d = 0.1$, the inflow

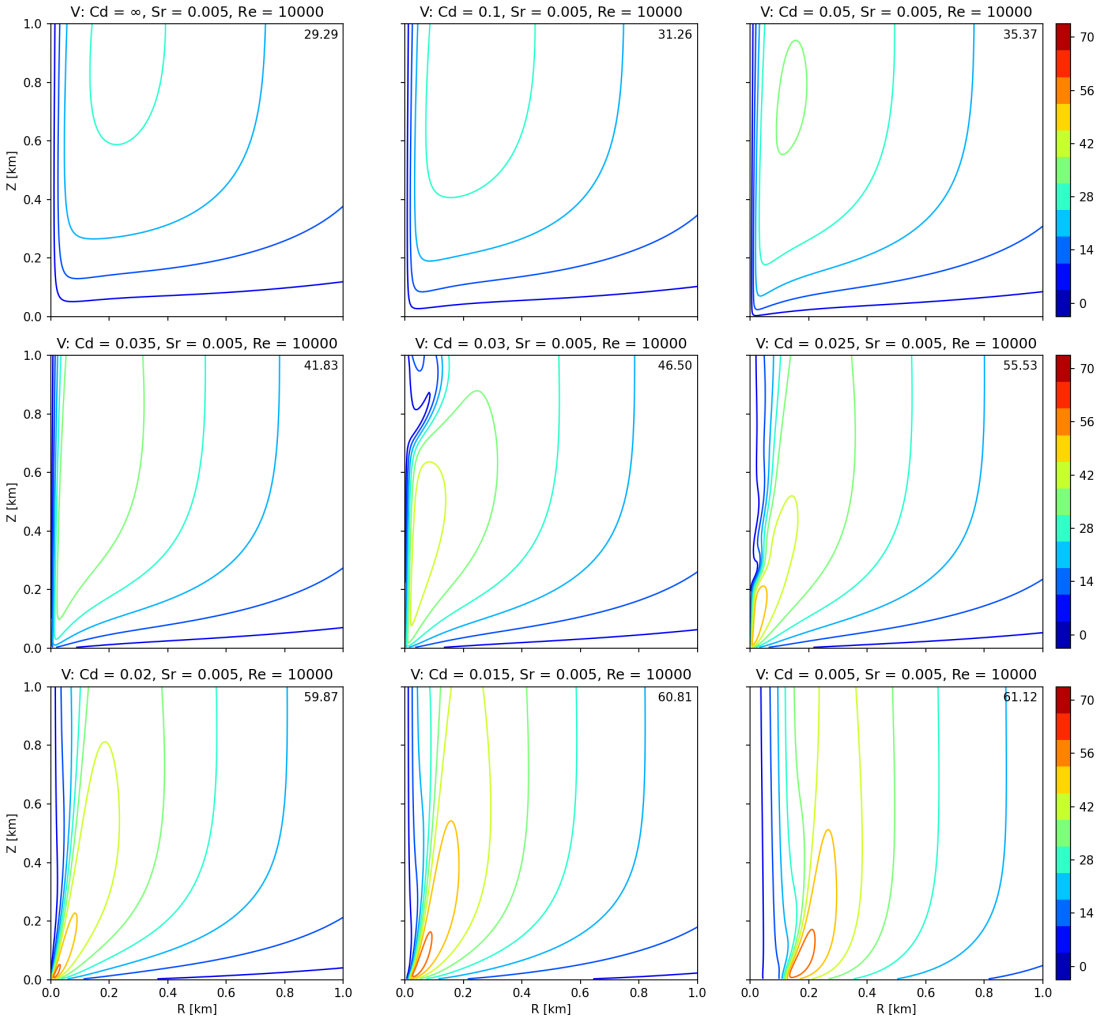


**Figure 4.32:** Tangential velocity contourlines in the corner region $[(0,0),(1,1)]$ for $S_r = 0.005$, $R_e = 10000$ and semi-slip boundary conditions.

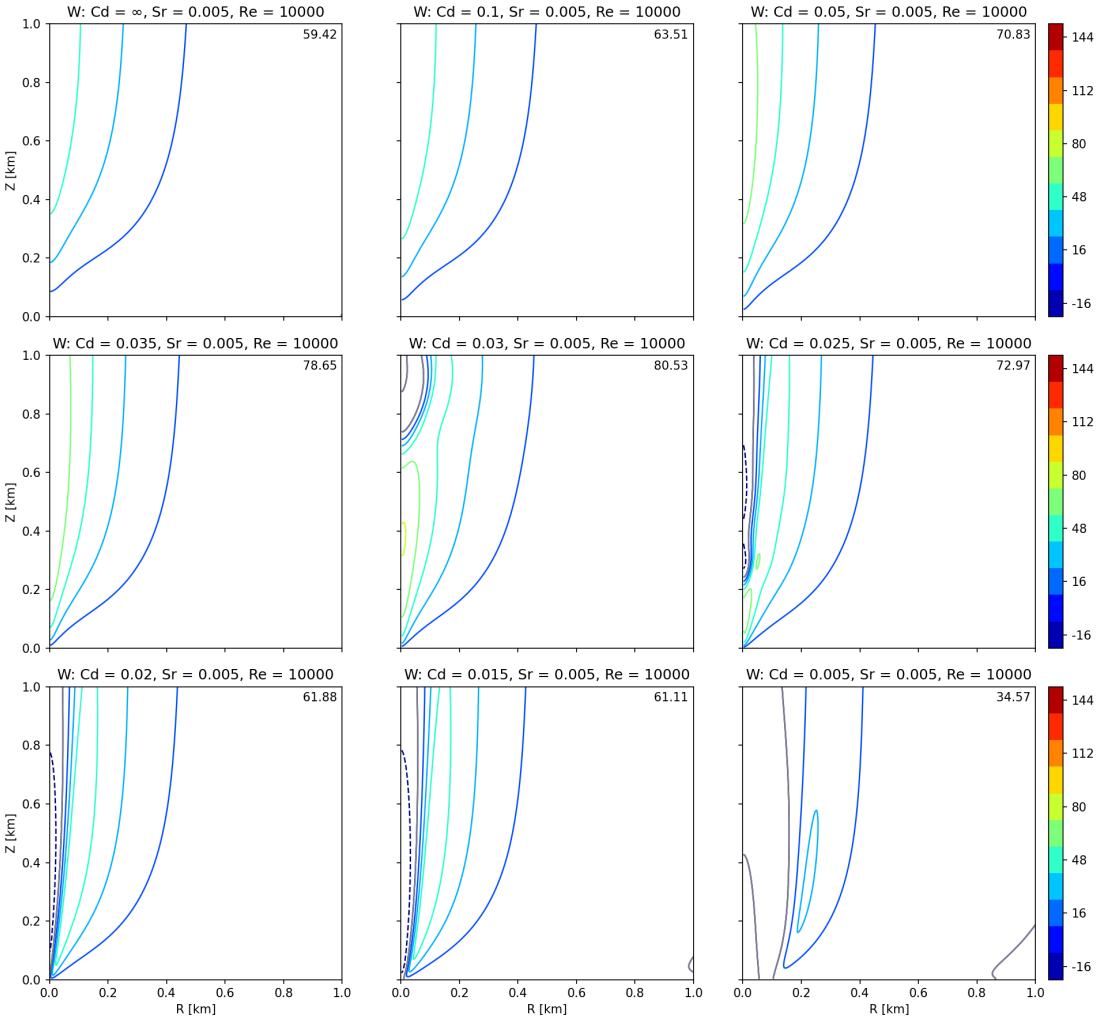


**Figure 4.33:** Vertical velocity contourlines in the corner region $[(0,0),(1,1)]$ for $S_r = 0.005$, $R_e = 10000$ and semi-slip boundary conditions. Zero contourline in grey.

experiences a marginal intensification and moves closer to the ground compared to the no-slip simulation. This behavior becomes more pronounced as $C_d$ decreases, as evidenced by the simulations for $C_d = 0.05$ and $C_d = 0.035$. It is worth highlighting how the inflow shifts closer to the origin, similarly to the behavior previously described for the updraft. This marks a significant difference with the no-slip simulations: while the zero surface velocity condition of no-slip simulations forces velocity to be essentially zero in the vicinity of the origin, semi-slip conditions allow the velocity to differ from zero even very close to the origin. Consequently, the stagnation area (the region in the vicinity of the origin where the inward flow is forced to decelerate and turn upward) must distort, and the stopping and upward turning of the inflow must be significantly more abrupt.

The occurrence of the vortex breakdown for $C_d = 0.03$ is indicated by the presence of an outflow near $z \approx 0.7$ km, denoted by an area of positive radial velocity. As previously noted, the updraft is forced to deviate outward by the presence of the centerline downdraft. This outflow shifts downward for $C_d = 0.025$ and $C_d = 0.02$, while the inflow continues to intensify and move closer to the origin. Additionally, the inflow appears narrower, while the radial velocity values at the surface keep growing. The descent of the vortex breakdown enlarges the region of the two-celled vortex at the expense of the single-celled one. As a result, the outflow occupies a considerably larger area, reducing the funneling of the updraft and thus decreasing the maximum values of the outflow. An example of this behavior is provided by the streamlines of figure 4.31. The deviation of the updraft is more abrupt for $C_d = 0.03$, and the outflow is concentrated in the area around the interface between the two-celled and single-celled vortices, where it shows strong values. On the other hand, for lower friction the transition is less sudden, and the outward motion is redistributed to a larger area. As stated while analyzing the $w$ field, the vortex for $C_d = 0.015$ has just reached a two-celled structure; hence the inflow still does not show any sign of weakening, as one would expect for a transition to a two-celled vortex. The weakening is retrieved for $C_d = 0.005$, along with the shift of the inflow to larger radii.

Figure 4.35 shows the pressure field for $S_r = 0.005$ under semi-slip conditions. The pressure drop intensifies for a decrease in friction, as evidenced by the progression of $\phi$ in the first four panels. The maximum pressure drop grows substantially, while the area of reduced pressure gradually extends downward, displaying a narrow and elongated shape. The vortex breakdown for $C_d = 0.03$ caps the pressure drop below 0.7 km, within the single-celled region of the vortex. As previously mentioned, for $C_d = 0.025$ and $C_d = 0.02$, the vortex attains the maximum pressure drop, while the area of reduced pressure appears pinned to the origin. The transition to a two-celled vortex ($C_d = 0.015$, 0.005) results in a significant weakening of the pressure drop, and the previously narrow and elongated shape transforms into a broad and vertically invariant one.

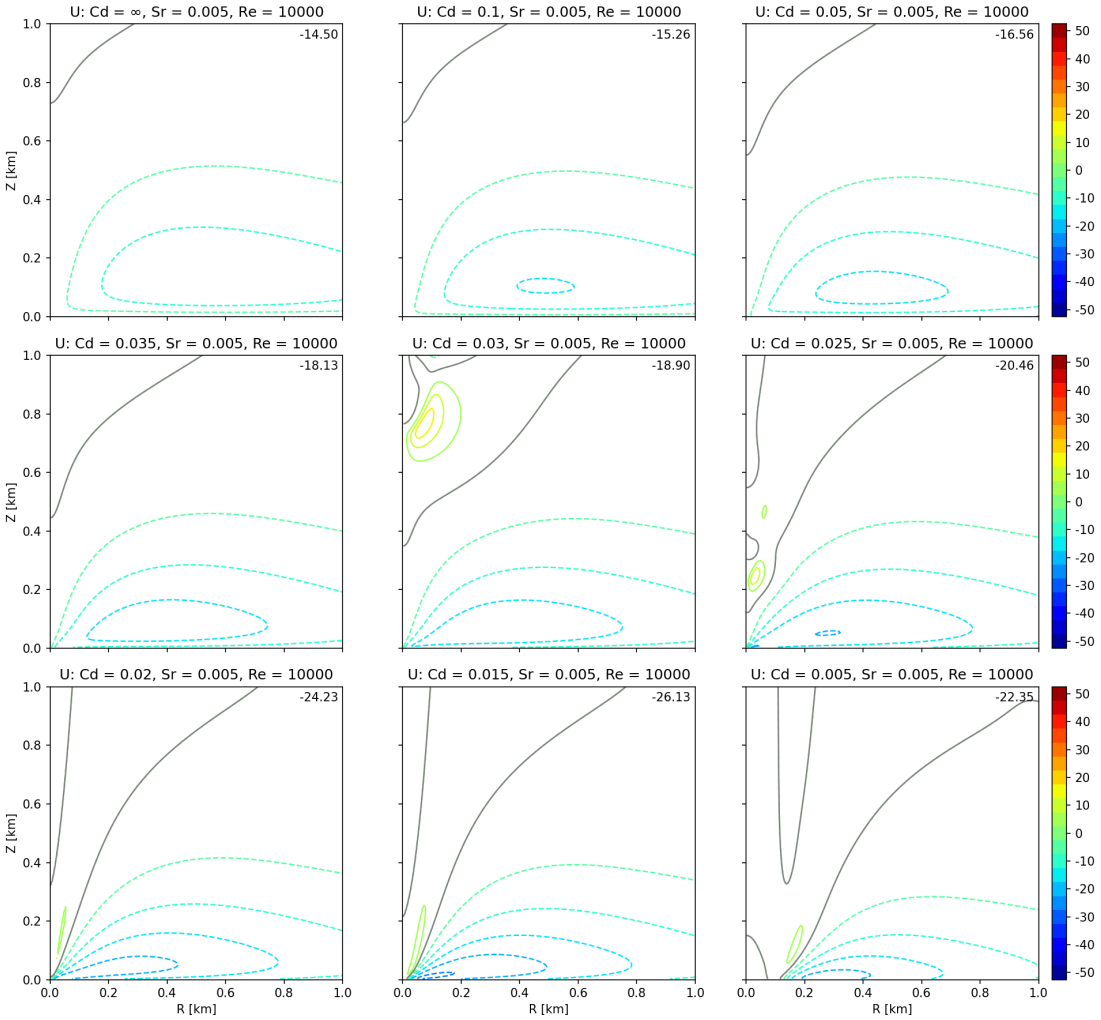


**Figure 4.34:** Radial velocity contourlines in the corner region $[(0,0),(1,1)]$ for $S_r = 0.005$, $R_e = 10000$ and semi-slip boundary conditions. Zero contourline in grey.

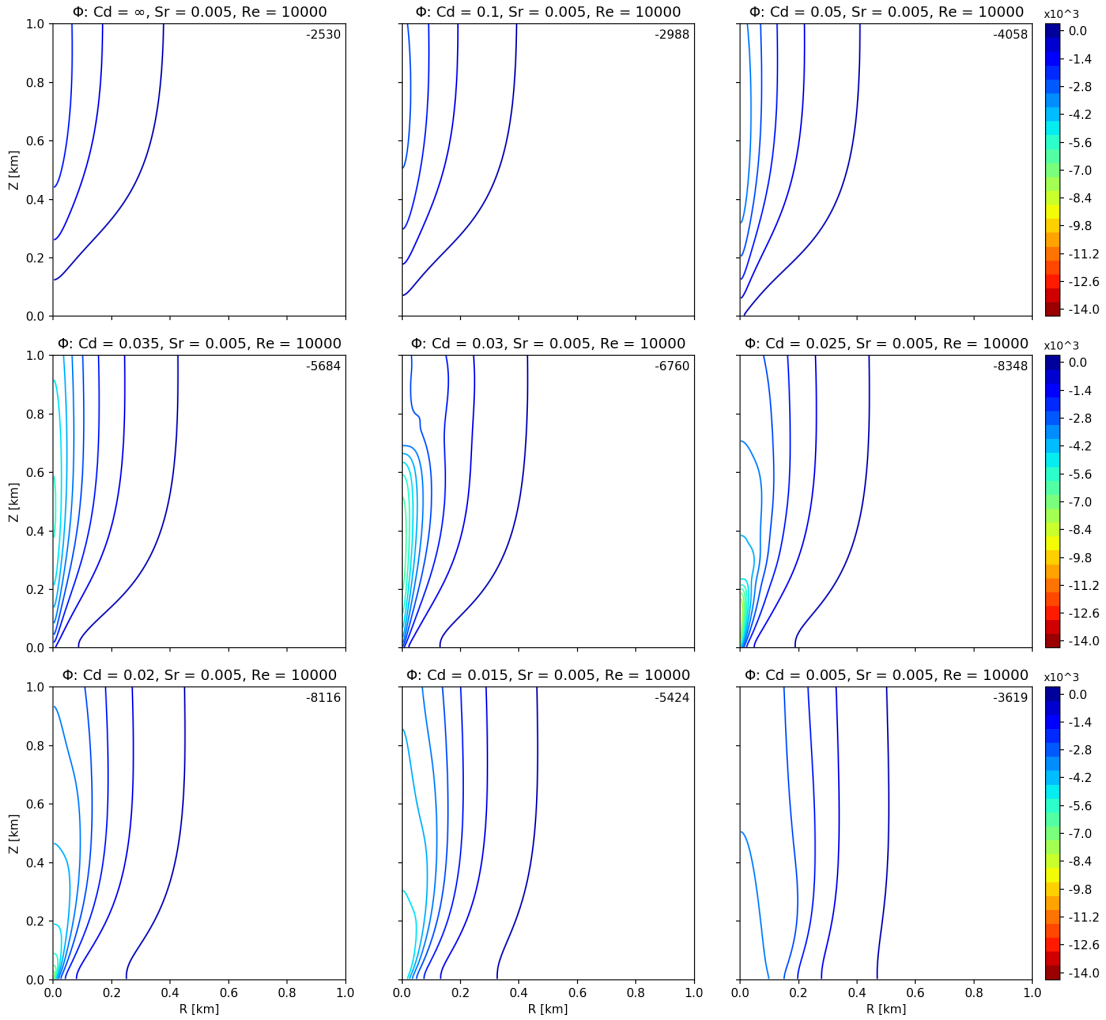


**Figure 4.35:** Pressure conturlines in the corner region $[(0,0),(1,1)]$ for $S_r = 0.005$, $R_e = 10000$ and semi-slip boundary conditions.

### Analysis of the $S_r = 0.005$ field extrema for decreasing $C_d$

In order to further investigate the role of the friction coefficient on vortex structure, the extrema of $v$, $u$, $w$, $\phi$, $-u \cdot r$, $H$ and their positions are plotted in figure 4.36 for all $C_d$ values employed in this work.

The maximum tangential velocity increases for decreasing friction coefficient, the increase being more intense as it approaches the maximum, reached for $C_d = 0.01$, before sharply diminishing to the free-slip value. The behavior of the radial position of the maximum $v$ is a clear indication of the process that undergoes for decreasing friction: the radius gradually diminishes from no-slip conditions, as the structure of the vortex tightens, it reaches a minimum value for $C_d = 0.02$ just before the transition, then it rapidly increases as the vortex attains a two-celled structure. The behavior is similar for the height of the maximum, the only difference being that the maximum remains at low levels after the transition to two-celled, and it increases only for $C_d = 0.0001$ and free-slip conditions.

It is remarkable how closely this behavior mirrors the effect of increasing swirl ratio for a fixed Reynolds number and no-slip conditions. In fact, we can compare these results with those of [Rot+16], who performed simulations for $R_e = 640000$ and small increments of $S_r$ around the transition (figure 4.37). We note the rapid increase of $v$, the peak for the optimal vortex at $S_r = 0.0025$, and the even sharper decrease of $v$ caused by the transition to a two-celled vortex. It is worth emphasizing that our aim is not to demonstrate that a variation of $C_d$ under semi-slip conditions is completely equivalent to a variation of $S_r$ under no-slip conditions, but rather that under semi-slip conditions the friction coefficient is an important parameter, playing a fundamental role in determining the structure of the vortex. Therefore, while comparing the present simulations with the results of [Rot+16], the focus is not on the numerical values of the extrema (which may depend on the specific position in the now three-dimensional parameter space), but on the shared features of these plots, such as the presence of a peak, or a sharp variation for small increments of the driving parameter.

The minimum radial velocity (maximum inflow), in the second panel, shows a similar behavior. The minimum of $u$ monotonically decreases for diminishing $C_d$ starting from no-slip conditions, the decrease becomes more intense approaching the peak, occurring for $C_d = 0.01$, then $u$ rapidly goes to zero. The position of the maximum inflow shows a similar behavior as the one of the maximum rotational velocity, approaching the origin as $u$ reaches its peak. The same difference between $r$ and $z$, observed for $v$, is present.

Moving to the maximum vertical velocity, we obtain further confirmation of the transition from one-celled to two-celled vortex for diminishing $C_d$, as the maximum updraft intensifies, reaches a peak for $C_d = 0.03$, then plummets as the vortex assumes a two-celled structure. Figure 4.37b shows a similar peaking behavior under no-slip simulations for varying swirl ratio, although the peak of $w$ is nearly four times the values that preceed the optimal vortex, while for the present semi-slip simulations the

increase is around 36%. The radial position of the maximum provides an even more straightforward demostration of the process, with the updraft remaining firmly centered until vortex breakdown, then $r$ increases as the vortex broadens its two-celled structure. The height of the maximum decreases towards the peak, then increases for $C_d \to 0$. It is important to note that for free-slip conditions and very low $C_d$, the updraft becomes very weak, broad, and vertically invariant, hence the height of the maximum $w$ loses significance.

The fourth panel shows the minimum of $\phi$ (maximum pressure drop). The pressure drop deepens significantly for decreasing friction, reaches a minimum in the optimal vortex configuration, and then rises for $C_d \to 0$. This behavior evidences that a decrease in friction, starting from a single-celled vortex, leads to an optimal vortex, in accordance with the behavior observed for no-slip simulations, for which the driving parameter is the swirl ratio (figure 4.37c). It goes without saying that the minimum pressure is always found at the center of the vortex ($r = 0$). Both the semi-slip simulations (figure 4.35) and the no-slip ones (figure 4.19d) reveal that while the pressure drop broadens significantly moving to a two-celled structure, the pressure continues to exhibit a radial increase from the minimum at $r = 0$. We observed from figure 4.35 how the vortex breakdown caps the pressure drop in the lower, one-celled section of the vortex. This behavior clearly emerges from the height of the minimum pressure, which consistently decreases as $C_d$ diminishes.

The fifth panel describes the behavior of $-u \cdot r$, which is related to the inflow mass flux (the demonstration is carried out in Appendix 2). The maximum of this quantity remains approximately constant from no-slip conditions to $C_d = 0.005$, before sharply decreasing to about half the previous value for $C_d = 0.001$ and lower. This behavior is consistent with the findings of section 4.2. A reduction in friction causes the frictional lower tier of the boundary layer to become narrower, without degrading the potential vortex structure of the boundary layer. Since it is the vertical diffusion that sustains the inflow, as soon as the lower tier vanishes, the inflow is almost completely suppressed, and the inflow mass flux plummets. The steep decrease in maximum mass flux is observed for $C_d = 0.001$, confirming that for this value the potential vortex structure of the boundary layer is lost, and the simulation exhibits free-slip features. Moreover, the vertical position of the maximum of $-u \cdot r$ descends towards the surface as the boundary conditions go from no-slip to semi-slip with $C_d = 0.005$, clearly illustrating the narrowing of the frictional layer.

The last panel of figure 4.36 shows that the extremum of $H$ is essentially driven by its pressure component, as the behavior of $H$ and its position for decreasing friction closely mirrors the one of $\phi$.

Overall, the analysis of the simulations for $S_r = 0.005$ and semi-slip boundary conditions revealed that a decrease in friction coefficient for a vortex firmly single-celled under no-slip conditions causes the vortex to intensify and tighten its structure. A further decrease in friction leads to the occurrence of a vortex breakdown, with the coexistence

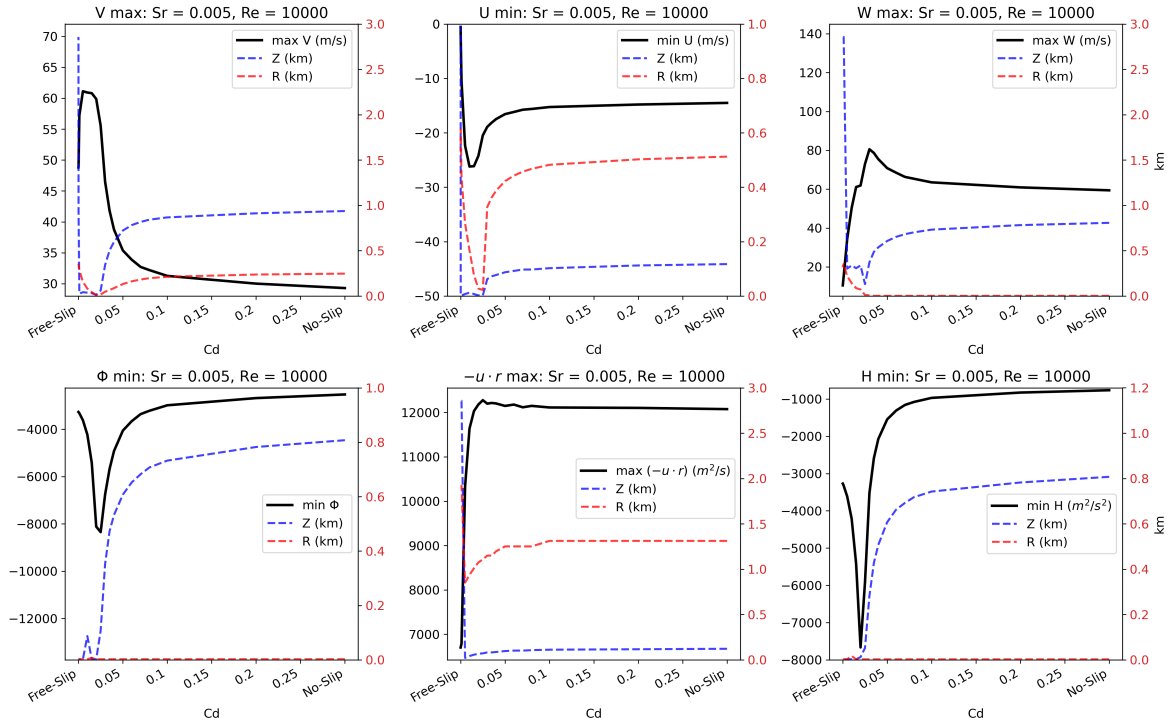


**Figure 4.36:** $S_r = 0.005$, $R_e = 10000$: extrema of $v$, $u$, $w$, $\phi$, $-u \cdot r$, $H$, and their position ($r$, $z$) for boundary conditions ranging from no-slip to free-slip.

of a two-celled vortex at upper levels, and a single-celled vortex right below. Specific values of $C_d$ within this transitional regime result in a maximum pressure drop, a feature that identifies the optimal vortex. The interface between the two types of vortices shifts downward for even lower values of $C_d$, resulting in the transition to a complete two-celled structure. As stated before, this behavior is analogous to what is observed when increasing the swirl ratio for fixed Reynolds number under no-slip conditions, the vortex experiences the same structural modifications.

### The effect of $C_d$ on the structure of the vortex for $S_r = 0.01$

In light of the results of the semi-slip simulations for $S_r = 0.005$, it is natural to expect that for $S_r = 0.01$ the vortex undergoes breakdown for much larger values of friction coefficient, as the vortex is very close to the transition under no-slip boundary conditions. In fact, figure 4.30 shows that the combination $S_r = 0.01$ - $R_e = 10000$ (green rectangle) sits right below the line indicating the optimal vortex (and therefore the vortex breakdown). Indeed, the breakdown for $S_r = 0.01$ is already observed for the largest value of friction employed in this study, $C_d = 0.2$, as evidenced by figure 4.38, showing the angular momentum, along with the position of maximum swirling velocity, and its

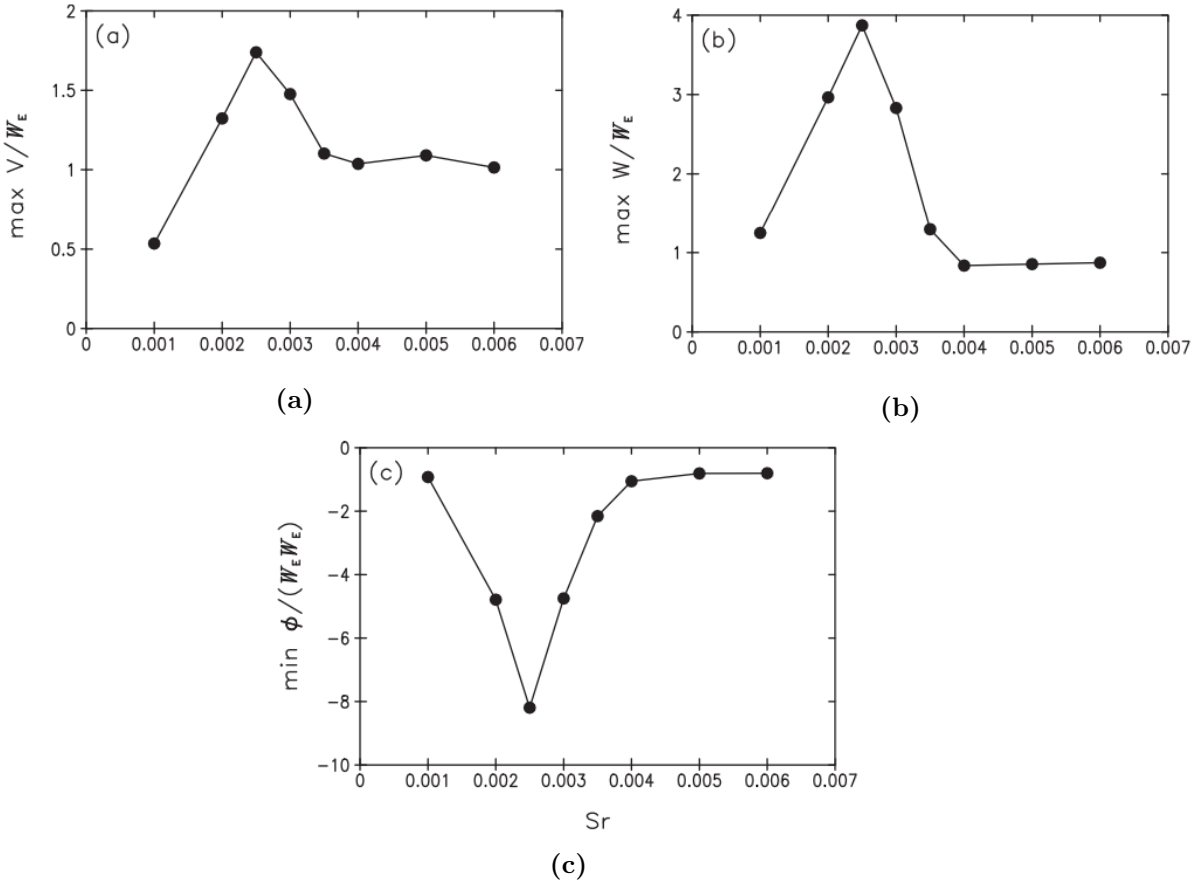


**Figure 4.37:** $R_e = 640000$ and no-slip conditions: a) normalized tangential velocity, b) normalized vertical velocity, and c) normalized pressure for various $S_r$ values. (After [Rot+16])

streamline. The choice of the simulations to display has been guided by the goal of providing the clearest representation of the vortex structure's evolution. Therefore, for $S_r = 0.01$, we choose to represent simulations under different $C_d$ values compared to the $S_r = 0.005$ case. The vortex breakdown is evident from the presence of a bulge of low $\Gamma$ extending above $z = 0.8$ km, as well as the deviation of the streamline. Similarly to the previous case, the breakdown progresses downward for decreasing friction. Notably, this progression occurs over a larger range of values, as the first friction value for which the breakdown reaches the surface is $C_d = 0.02$ (not shown), very close to the $C_d = 0.015$ value for $S_r = 0.005$. Moreover, it is evident that the bulge of low angular momentum is considerably larger compared to the $S_r = 0.005$ case. The position of the maximum tangential velocity moves closer to the origin for decreasing friction up to $C_d = 0.05$, whereas for lower values of $C_d$ the position shifts to larger radii. For $C_d = 0.015$, the vortex shows a two-celled structure, with a gap of low $\Gamma$ elongating all the way to the

surface. As evidenced by the first two panels of the last row, a further decrease in friction results in the expansion of the vortex, exhibiting now a broad central area of reduced angular momentum. The last panel, for $C_d = 0.001$, shows that for $C_d \to 0$ the $\Gamma$ field becomes more vertically invariant, and the simulation behaves increasingly like a free-slip one.

The vortex breakdown for $C_d = 0.2$ is evident from figure 4.39, as the streamlined shape described by the $v$ field of the no-slip simulation is truncated by the vortex breakdown, restricting the single-cell portion of the vortex below $z = 0.8$ km. The first two panels of the second row show that a further decrease in friction reduces even more the one-celled portion of the vortex, as the interface with the two-celled portion descends towards the surface. The situation for $C_d = 0.035$ explains why the maximum $v$ is found further from the origin, as the vortex tends to display a structure more akin to a two-celled vortex, with a vertical column of strong swirling flow extending from $r = 0.2$ to $r = 0.6$ km, eventually connecting with the small single-celled vortex close to the surface. The successive panels show the expansion of the vortex for decreasing $C_d$, along with the tendency of the $v$ field to be more vertically aligned. It is noteworthy that, in contrast with the $S_r = 0.005$ case, the maximum tangential velocity exhibits modest variation across the entire range of $C_d$ values. In particular, there is no evidence of a peak of rotational velocity, a possible indication of the optimal vortex. Considering that the simulation for the highest friction represents already a vortex breakdown event, and how close the corresponding no-slip case is to transition, the optimal vortex may occur for higher values of $C_d$ than those explored in this study. A continuation of this work, including more semi-slip simulations for vortices close to transition, might shed some light on this topic.

Figure 4.40 presents the vertical velocity for $S_r = 0.01$. The first three panels show how the intense updraft of the no-slip case gets cut off by the vortex breakdown for $C_d = 0.2$ and $C_d = 0.07$. The updraft is slightly reduced, but remains very intense. Due to the breakdown, there is a tendency of the updraft to skew outward. The next panels show the progressive descent of a very weak downdraft, and simultaneous weakening of the updraft. In particular, the simulation for $C_d = 0.015$ shows the downdraft extending all the way to the lower boundary, indicating the two-celled structure of the vortex. A further decrease in friction reduces the updraft's intensity and shifts it to larger radii. The last panel, for $C_d = 0.001$, shows a severely reduced updraft, a clear indication of the free-slip characteristic of the simulation for such low value of friction. We note that, similarly to the $v$ field, there is no updraft peak, and the maximum value is the one of the no-slip simulation. In addition to the hypothesis already made, we observe from figures 4.41 and 4.42 that, for decreasing friction, the inflow does not strengthen and the pressure drop weakens, whereas for $S_r = 0.005$ the opposite is true. Since both the inpinging inflow and the vertical pressure gradient provide important contributions to the updraft, this can explain the different behaviors found for $S_r = 0.005$ and $S_r = 0.01$.

While the minimum value of the radial velocity does not vary much across the sim-

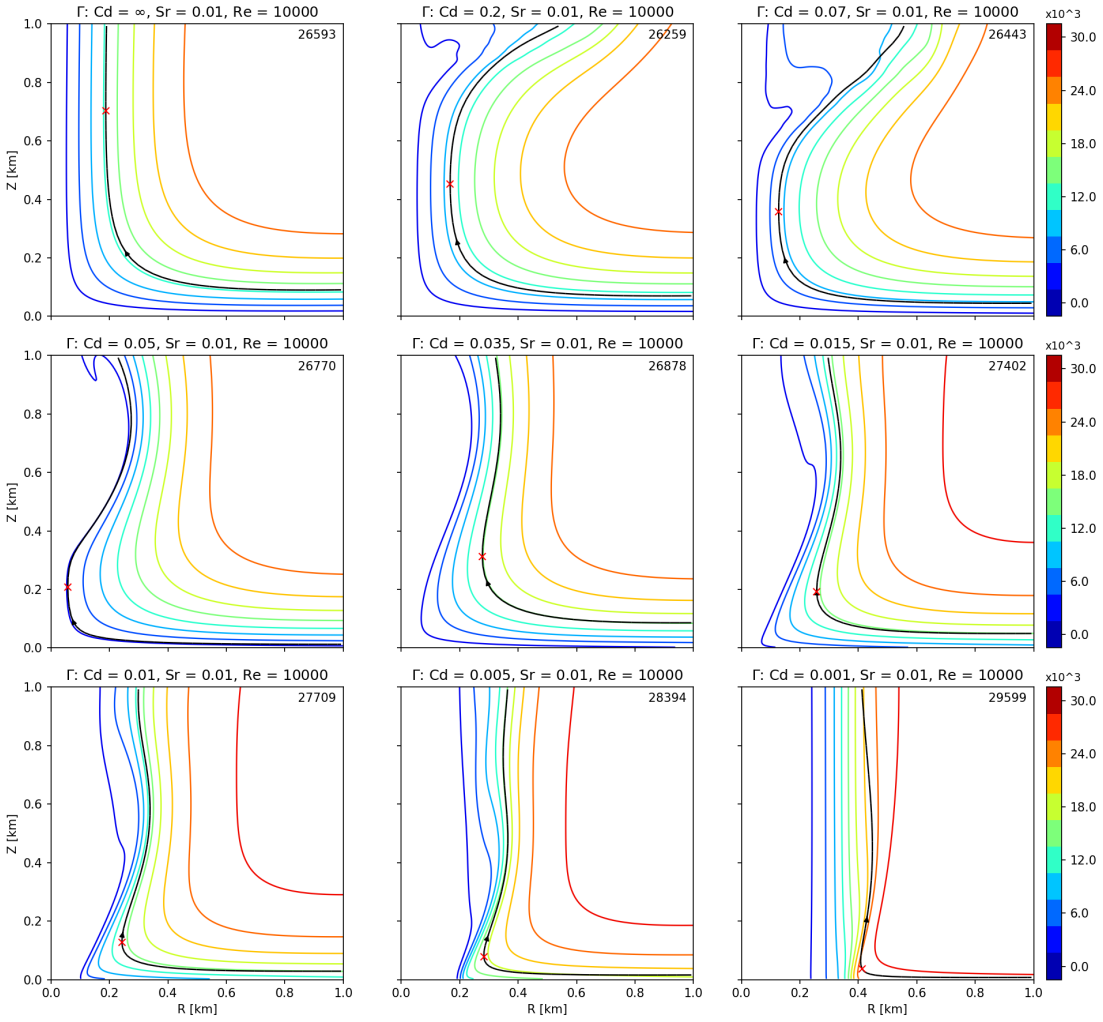


**Figure 4.38:** Angular momentum contourlines in the corner region $[(0,0),(1,1)]$ for $S_r = 0.01$, $R_e = 10000$ and semi-slip boundary conditions. The red x is the position of the maximum tangential velocity, and the solid black line is the streamline referring to that position.

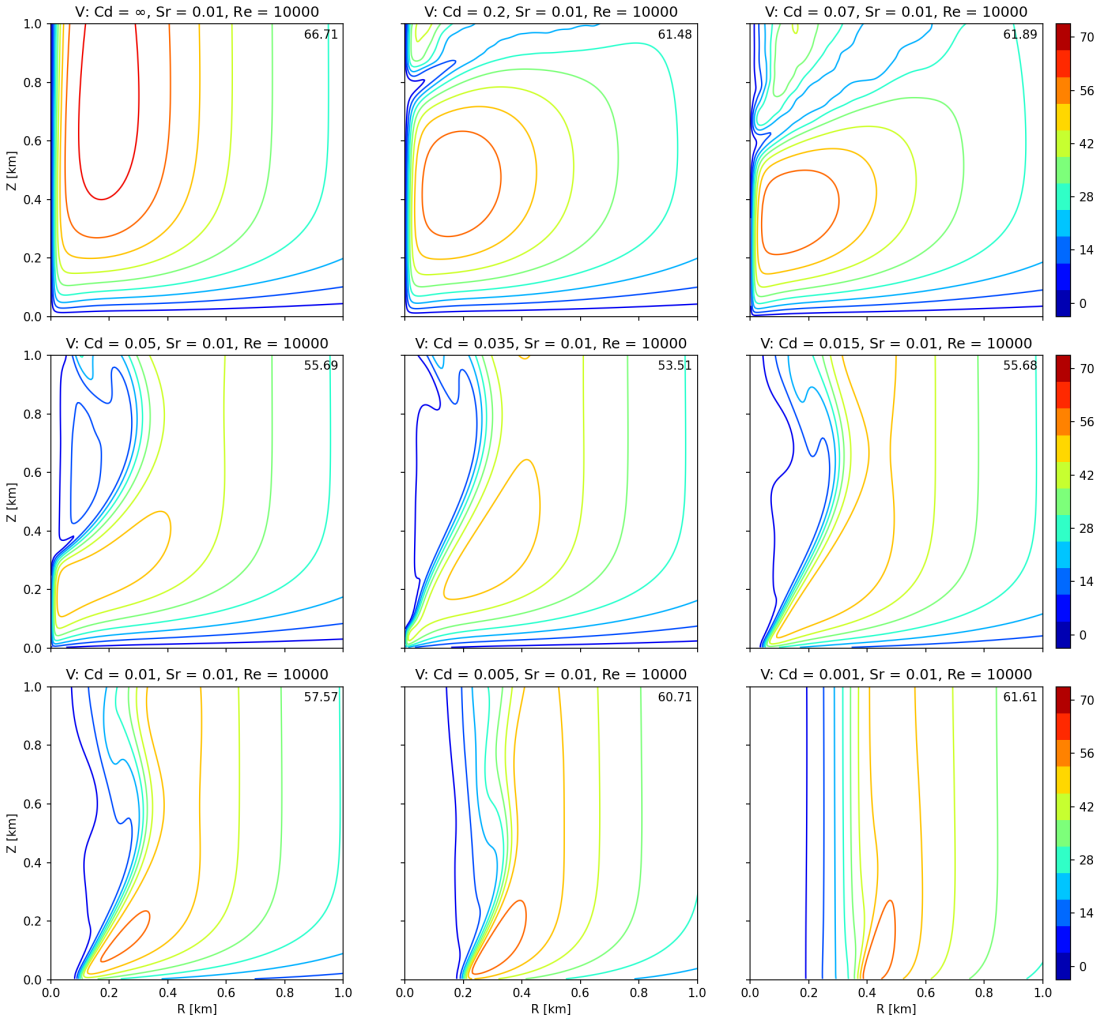


**Figure 4.39:** Tangential velocity contourlines in the corner region $[(0,0),(1,1)]$ for $S_r = 0.01$, $R_e = 10000$ and semi-slip boundary conditions.

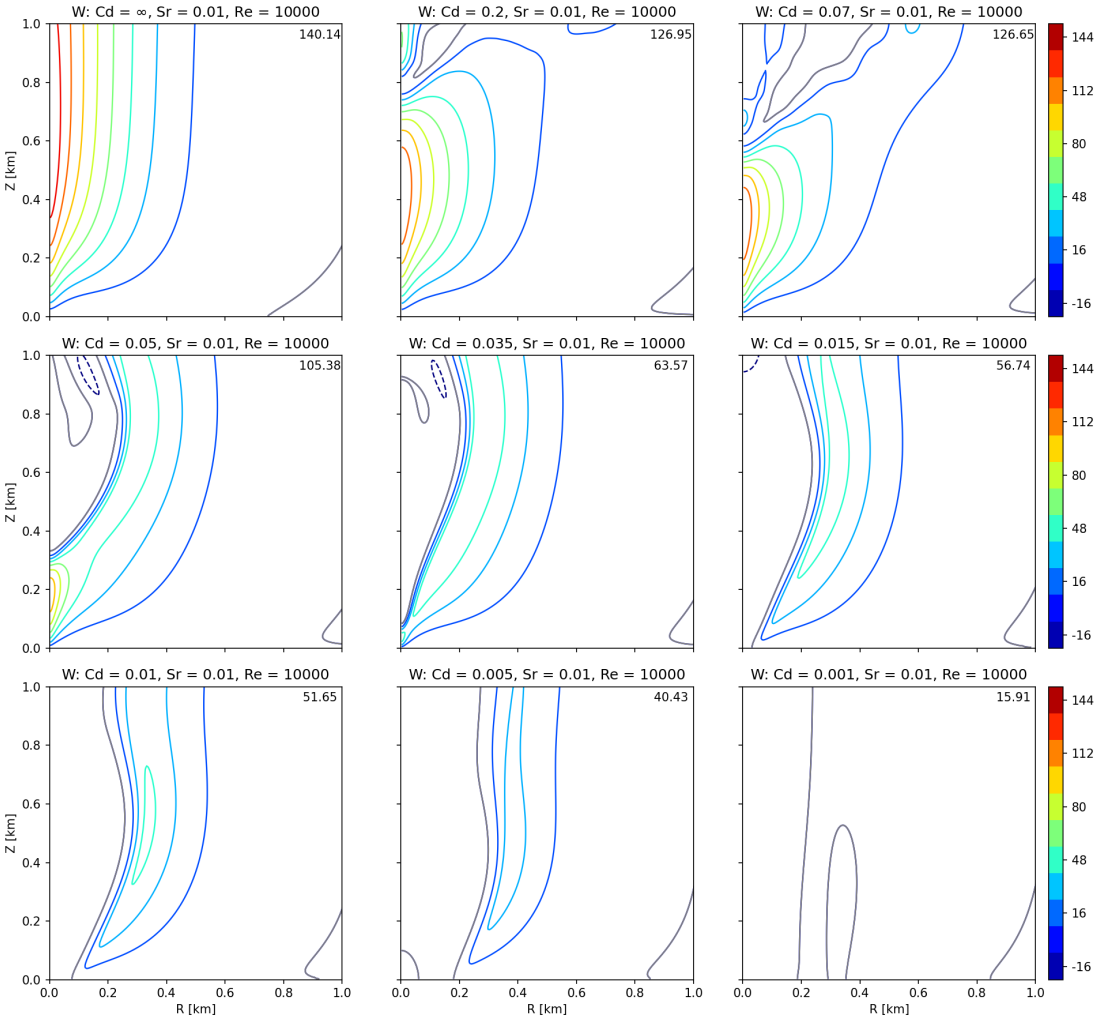


**Figure 4.40:** Vertical velocity contourlines in the corner region $[(0,0),(1,1)]$ for $S_r = 0.01$, $R_e = 10000$ and semi-slip boundary conditions. Zero contourline in grey.

ulations, the structure of the inflow undergoes extensive modifications, as figure 4.41 illustrates. For $C_d = 0.2$ a strong outflow appears in the upper levels of the corner region, as a consequence of the vortex breakdown. The descent of the breakdown for $C_d = 0.07$ explains the descent of the outflow, which tilts vertically. For $C_d = 0.05$, the outflow is even closer to the surface, squeezing the inflow. Moreover, the very intense and compact outward flow has tilted even more, assuming a predominantly vertical shape. A further decrease in friction to $C_d = 0.035$ leads to a reduction of the intensity of the outflow, which elongates towards the origin, distorting the inflow. A two-celled structure is present for $C_d = 0.015$, with a gap of negligible radial velocity near the origin. For lower $C_d$ values, the inflow moves to larger radii, and the outflow is substantially reduced. Finally, for $C_d = 0.001$, the near complete absence of the inflow suggests once more how for this value of friction the simulation is very similar to the free-slip case. The progressive weakening and tilting of the outflow is understandable taking in consideration the role of the updraft: while for larger values of friction ($C_d = 0.2$) the outflow severely disrupts and cuts off the updraft, for lower values ($C_d = 0.035$) the updraft and the outflow coexist, and the tendency of the updraft to become more vertically aligned means that the outward component is reduced.

Similar to the $w$ field, the first four panels of figure 4.42 illustrate how the elongated pressure drop of the no-slip case gets constrained to the lower levels by the breakdown for decreasing $C_d$. The most intense part of the pressure drop is limited to a very small portion near the origin for $C_d = 0.035$. The two-celled vortex for $C_d = 0.015$ exhibits a broad pressure drop, and a further decrease in friction enhances the vertical alignment of the pressure field. As previously mentioned, there is no indication of a peak in pressure drop for simulations where two-celled and single-celled vortices coexist. Instead, the pressure minimum slowly increases as the vortex breakdown shifts downward, before rising more abruptly as the vortex attains a complete two-celled structure. The two-celled vortices display similar values of minimum $\phi$, and the effect of decreasing $C_d$ is limited to a broadening and vertical alignment of the pressure drop.

### Analysis of the $S_r = 0.01$ field extrema for decreasing $C_d$

The extrema of $v$, $u$, $w$, $\phi$, $-u \cdot r$, $H$ and their positions are depicted in figure 4.43 for $S_r = 0.01$. The first panel illustrates that the maximum tangential velocity does not vary much throughout the entire range of $C_d$ values. Most of the variation is concentrated around $C_d = 0.035$, where, as previously observed, the $v$ field adjusts from largely one-celled to mostly two-celled. This adjustment weakens the one-celled vortex core near the origin, and the position of the maximum clearly shows the shift away from the origin for $C_d = 0.035$. For very low $C_d$ the radial position illustrates the expansion of the vortex, with the maximum $v$ moving to larger radii.

The magnitude of the minimum of $u$ experiences a gradual decrease for diminishing $C_d$, followed by a significantly steeper reduction of the inflow as the conditions move

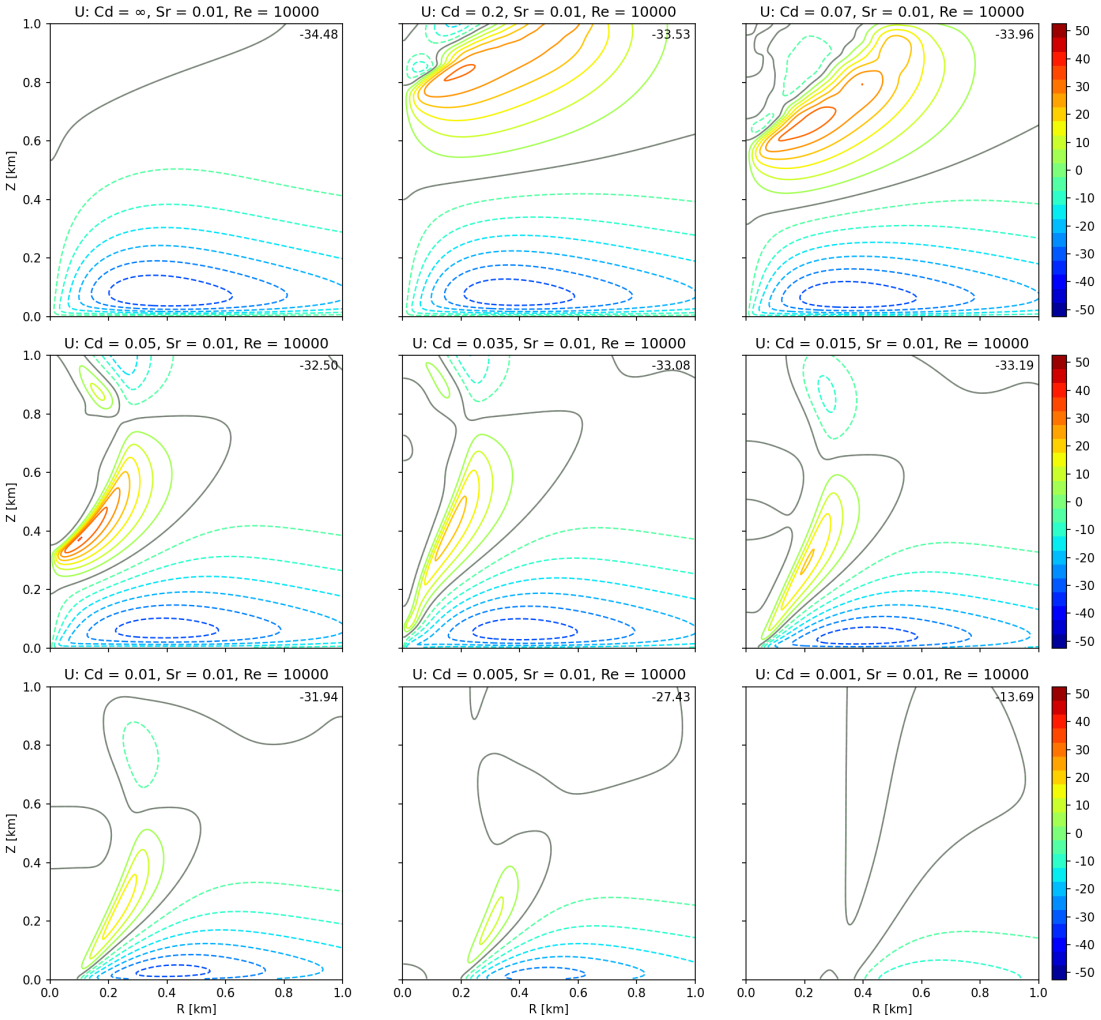


**Figure 4.41:** Radial velocity contourlines in the corner region $[(0,0),(1,1)]$ for $S_r = 0.01$, $R_e = 10000$ and semi-slip boundary conditions. Zero contourline in grey.

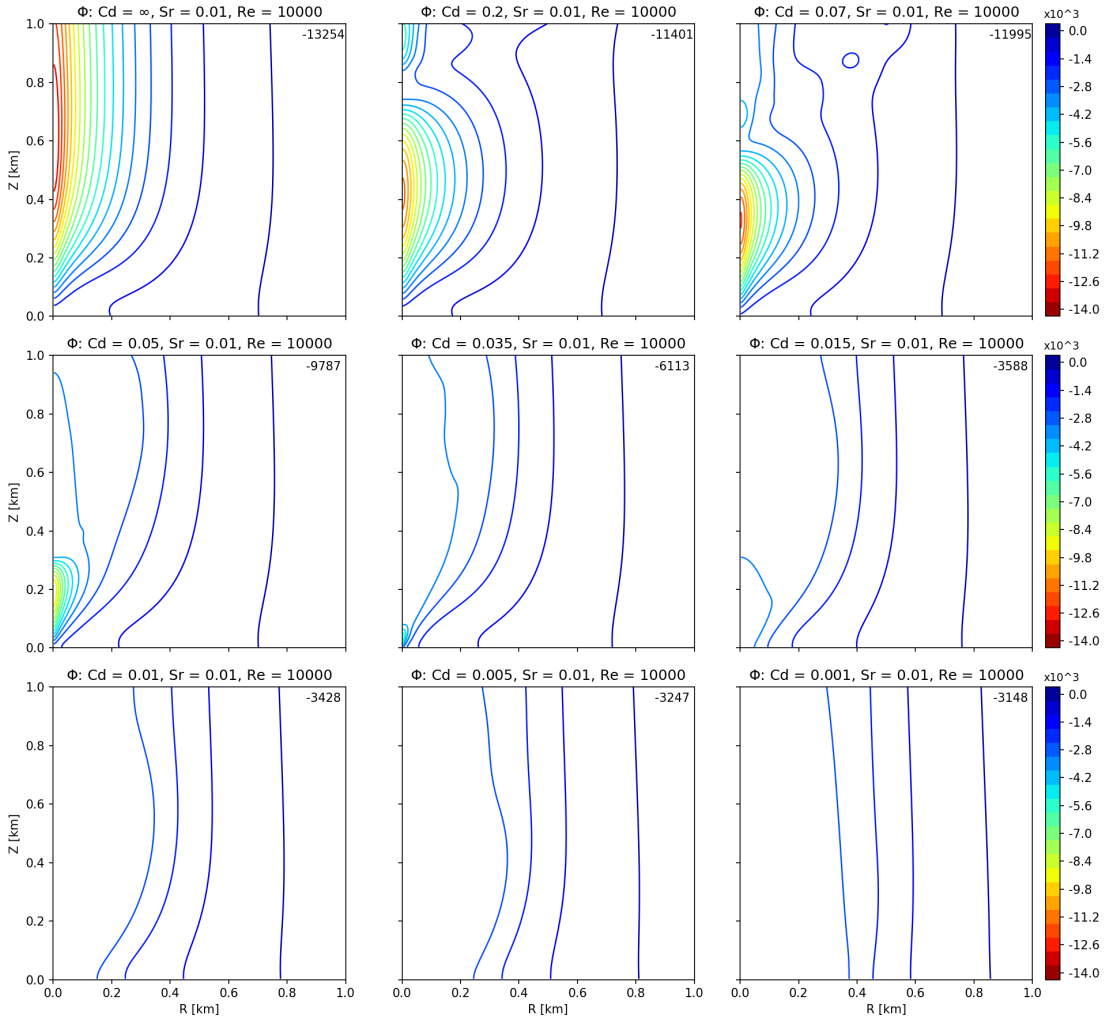


**Figure 4.42:** Pressure conturlines in the corner region $[(0,0),(1,1)]$ for $S_r = 0.01$, $R_e = 10000$ and semi-slip boundary conditions.

towards free-slip. The decreasing vertical position describes the progressive narrowing of the inflow due to the descent of the vortex breakdown. This phenomenon also explains why the radial position of the maximum inflow moves to larger radii before the complete transition to a two-celled vortex: as it is evident from figure 4.41, the breakdown produces an outflow that wedges towards the origin, weakening and shifting the inflow. The broadening of the two-celled vortex under low friction explains the successive pronounced increase of $r$.

The third panel confirms that an initial reduction of friction from no-slip conditions results in a moderate weakening of the updraft, as observed in figure 4.40 for $C_d = 0.2$ and $C_d = 0.07$, with the maximum $w$ decreasing from 140.14 to 126.65 m/s. A further decrease of $C_d$ is met with a more intense reduction of maximum $w$ all the way to free-slip conditions. The updraft adjustment around $C_d = 0.035$ is illustrated by a discontinuity of the rate of decrease of $w$, as well as a robust shift of the position of the maximum away from the origin. The maximum then continues to move to larger radii as a result of the vortex broadening under diminishing friction.

The pressure minimum slowly increases from no-slip conditions to $C_d = 0.06$. As the breakdown approaches the surface, the pressure rapidly rises until the vortex reaches a complete two-celled structure at $C_d = 0.02$. Subsequently, the pressure slowly rises to the free-slip value as $C_d$ diminishes. As for $S_r = 0.005$, the minimum pressure remains firmly central ($r = 0$), whereas its vertical position is observed at lower levels for decreasing $C_d$. Notably, the last panel shows that $H$ is no longer dominated by $\phi$, and the velocity components represent important contributions, in contrast to the $S_r = 0.005$ case.

Finally, the inflow mass flux exhibits the same behavior as for $S_r = 0.005$: $-u \cdot r$ remains relatively stable until the lower tier of the boundary layer vanishes for $C_d = 0.001$. The shrinking of the frictional layer is evidenced by the monotonic decrease in the height of maximum inflow mass flux. This once more validates the findings of section 4.2.

### The effect of $C_d$ on the structure of the vortex for $S_r = 0.04$

Moving to the $S_r = 0.04$ case, we expect that a decrease in friction will continue to induce structural changes akin to those produced by a variation of swirl ratio for a fixed $R_e$ and under no-slip boundary conditions. The no-slip solution for $S_r = 0.04$ and $R_e = 10000$ is a two-celled vortex, as illustrated by the solution matrix in figure 4.30 (yellow rectangle), where this specific case is found above the optimal vortex line in the $S_r$ - $R_e$ space. For very large swirl ratios, the two-celled vortex loses its axial symmetry and breaks into satellite vortices revolving around the center axis ([Rot13]). Naturally, the present work's axisymmetric model is not capable of capturing this behavior. Therefore, it is natural to anticipate that the introduction of semi-slip conditions for $S_r = 0.04$ will not lead to any change in structure other than the previously described vortex enlargement, but rather we expect the simulations to show more unsteadiness. Additionally, as $C_d \to 0$, we

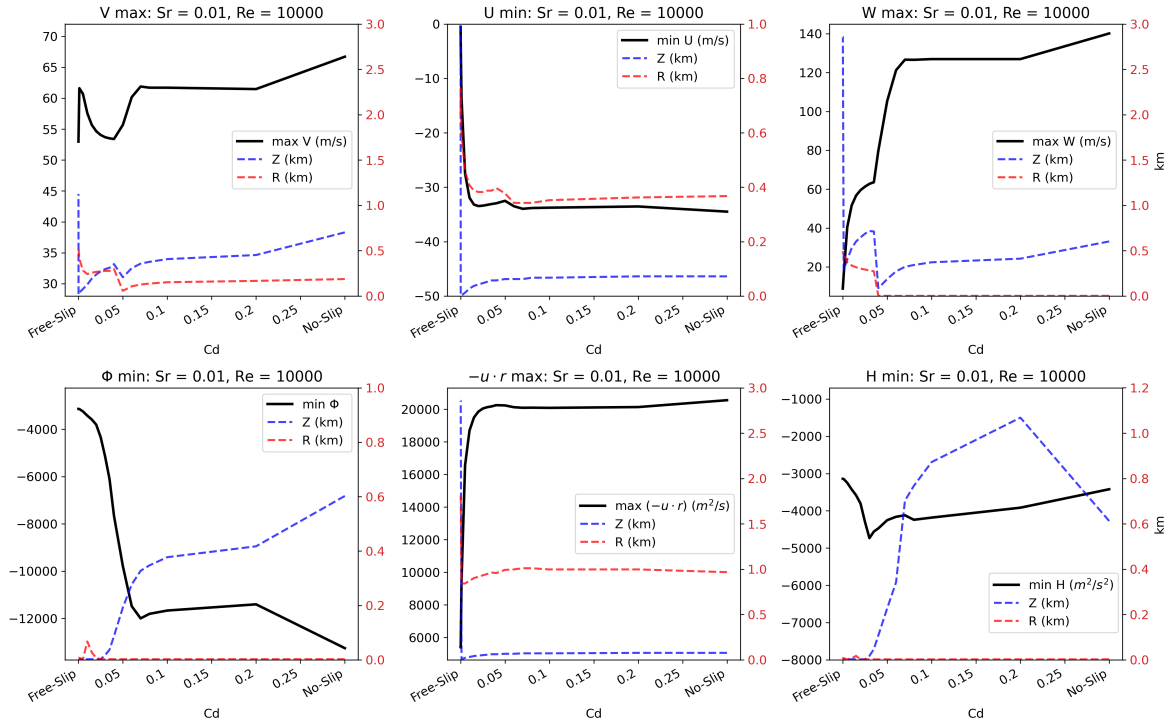


**Figure 4.43:** $S_r = 0.01$, $R_e = 10000$: extrema of $v$, $u$, $w$, $\phi$, $-u \cdot r$, $H$, and their position ($r$, $z$) for boundary conditions ranging from no-slip to free-slip.

expect to observe a progressive enhancement of free-slip features, such as reduced inflow, updraft, and an increased vertical alignment for all the fields. Indeed, while remaining statistically stationary, the semi-slip simulations under lower friction showed increased unsteadiness.

Figure 4.44 presents the angular momentum in the corner region for $S_r = 0.04$ and under semi-slip conditions. The values of $C_d$ are the same as for $S_r = 0.01$. The $\Gamma$ field clearly shows the lack of structural changes across the entire range of $C_d$ values. The most noticeable feature is the progressive tendency of the $\Gamma$ field to be vertically aligned moving towards free-slip conditions. There is a marginal vortex broadening, that can be better appreciated from the slow increase of the radial position of the maximum tangential velocity in figure 4.49. The structure emerging from the angular momentum field is that of two-celled vortex, with a column of low $\Gamma$ at its center.

The same observations can be made regarding the rotational velocity field (figure 4.45). The lack of changes in vortex structure and the tendency of vertical alignment as $C_d \to 0$ emerge clearly from the $v$ field. The vortex enlargement is more evident for $v$ than for $\Gamma$, as the vortex core is pushed further away from the origin for decreasing $C_d$. As the surface values of $v$ increase, the lower vortex core tends to become narrower. Moreover,

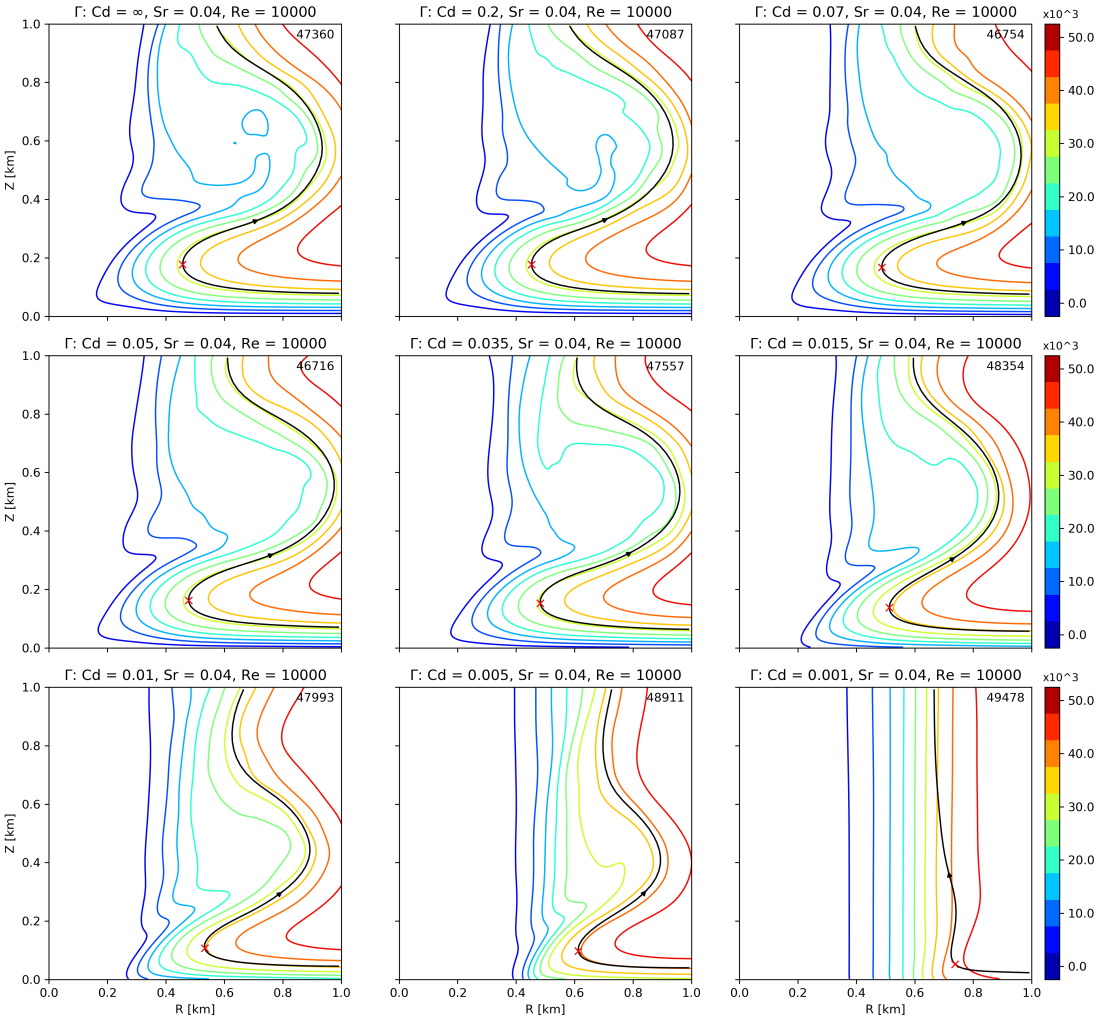


**Figure 4.44:** Angular momentum contourlines in the corner region $[(0,0),(1,1)]$ for $S_r = 0.04$, $R_e = 10000$ and semi-slip boundary conditions. The red x is the position of the maximum tangential velocity, and the solid black line is the streamline referring to that position.

the values of maximum swirling velocity do not vary much as friction is diminished.

Figure 4.46 displays the vertical velocity for $S_r = 0.04$ and semi-slip conditions. As anticipated, there is little variation in the $w$ field as friction diminishes. It can be observed how the updraft gradually weakens for $C_d \to 0$, and the pattern of updraft and downdraft tends to degrade as the vertical velocity becomes more vertically invariant. The simulation for $C_d = 0.001$ exhibits an almost complete lack of updraft in the corner region, a characteristic that proves how, for very low friction coefficient, the vortex behaves largely as if under free-slip boundary conditions. It is also worth highlighting the progressive shift to larger radii of the updraft, as a result of the vortex broadening for decreasing friction.

The radial velocity field (figure 4.47) confirms that the vortex does not undergo changes in structure as $C_d$ approaches zero. While the inflow does weaken for decreasing friction, this happens slowly over most of the range of $C_d$ values, whereas a sharp decrease of intensity occurs only for very low friction. The enlargement of the vortex for diminishing friction is depicted as a progressive shift of the inflow/outflow pattern to larger radii. For instance, comparing the simulations for $C_d = 0.07$ and $C_d = 0.015$ it is evident how the area near the origin becomes free of both inflow and outflow, and the radial velocity goes to zero in that region. The lack of inflow for $C_d = 0.001$ is in line with the expected behavior under very low friction.

The comparison of the pressure field between the simulations for $S_r = 0.005$ and $S_r = 0.01$, and the present simulations for $S_r = 0.04$ (figure 4.48) provides a clear illustration of how a variation in friction produces minimal effect in the present case. The previous cases showed large variations in the shape and values of $\phi$. Instead, for $S_r = 0.04$, the field remains largely the same, with only a tendency to align vertically as $C_d$ decreases.

### Analysis of the $S_r = 0.04$ field extrema for decreasing $C_d$

We conclude the analysis of the semi-slip simulations for $S_r = 0.04$ by presenting the extrema of the fields (figure 4.49). We must preliminarily note that the positions of the extrema of $\phi$ and $w$ are not meaningful. For $\phi$, the homogeneity of the field implies that the large and sudden shift in position between $C_d = 0.08$ and $C_d = 0.07$ does not correspond to a meaningful change in pressure. Regarding $w$, it can be observed in figure 4.46 how the updraft is composed of areas of moderately higher velocity, these areas extend also above the corner region (not shown). Since all these areas show comparable values of vertical velocity, the relative unsteadiness causes the maximum to be found at different positions for small increments of $C_d$, without an underlying change in intensity or structure.

Another preliminary observation is that all the fields appear noisy for $C_d < 0.08$. While this reflects the increased unsteadiness for decreasing friction, the effect is accentuated by the abundance of simulations in that range of $C_d$ values.

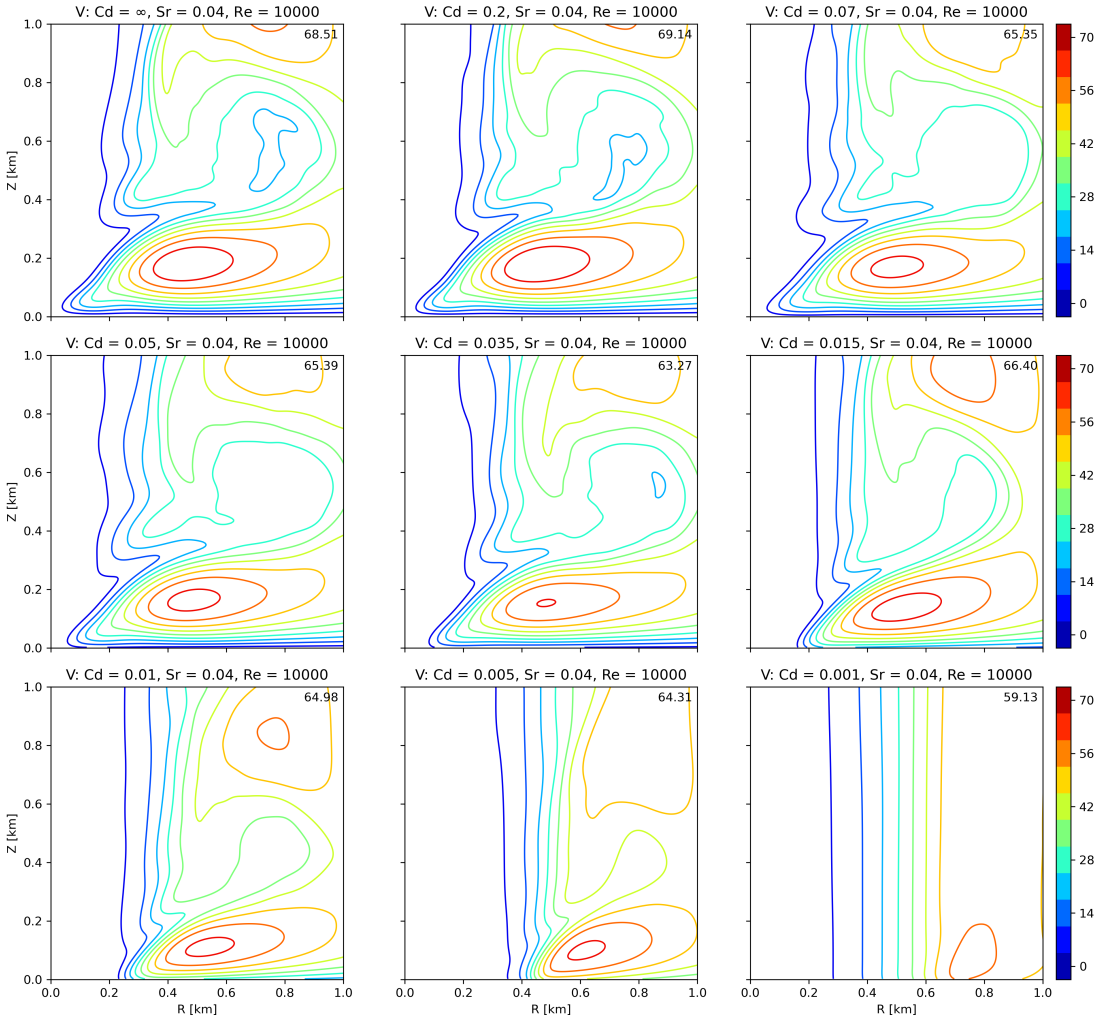


**Figure 4.45:** Tangential velocity contourlines in the corner region $[(0,0),(1,1)]$ for $S_r = 0.04$, $R_e = 10000$ and semi-slip boundary conditions.

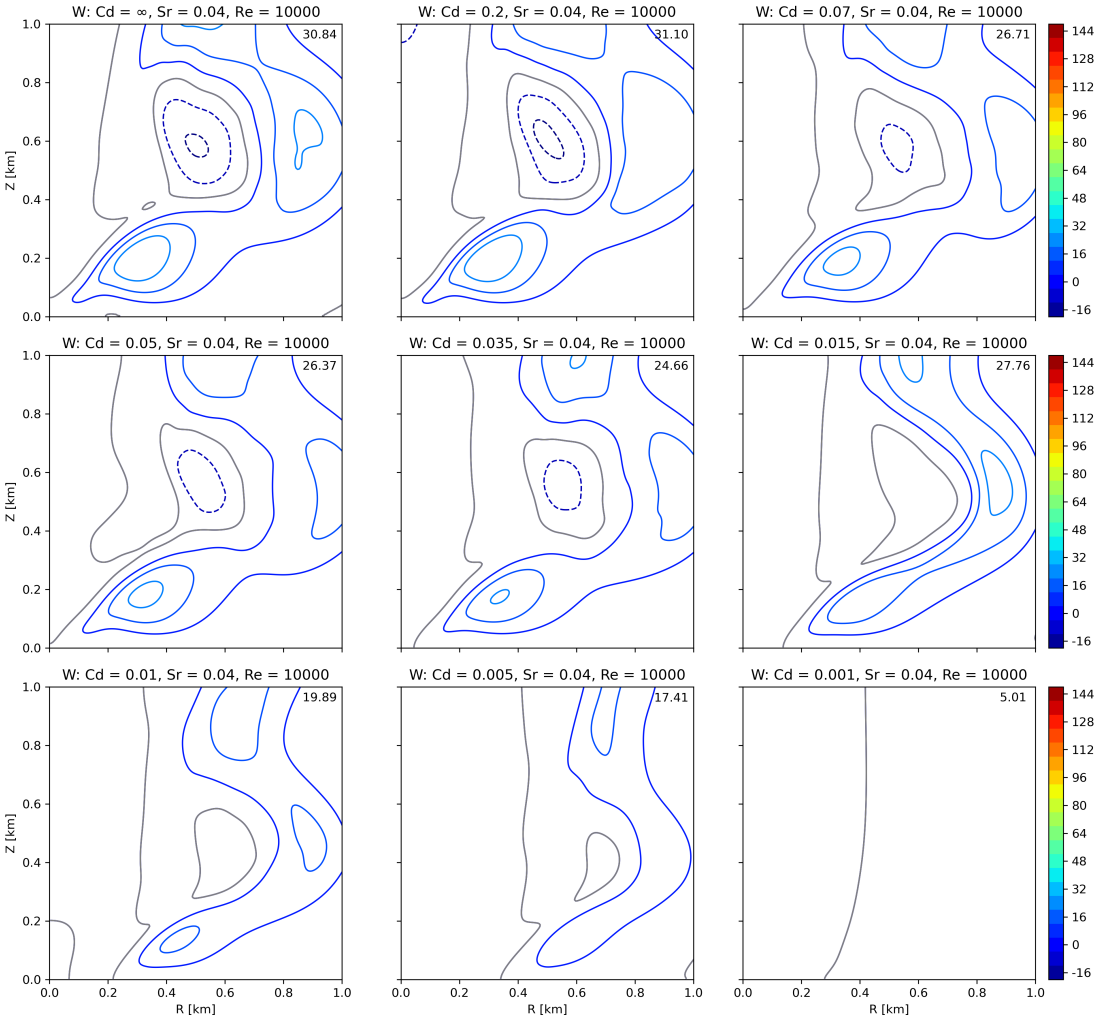


**Figure 4.46:** Vertical velocity contourlines in the corner region $[(0,0),(1,1)]$ for $S_r = 0.04$, $R_e = 10000$ and semi-slip boundary conditions. Zero contourline in grey.

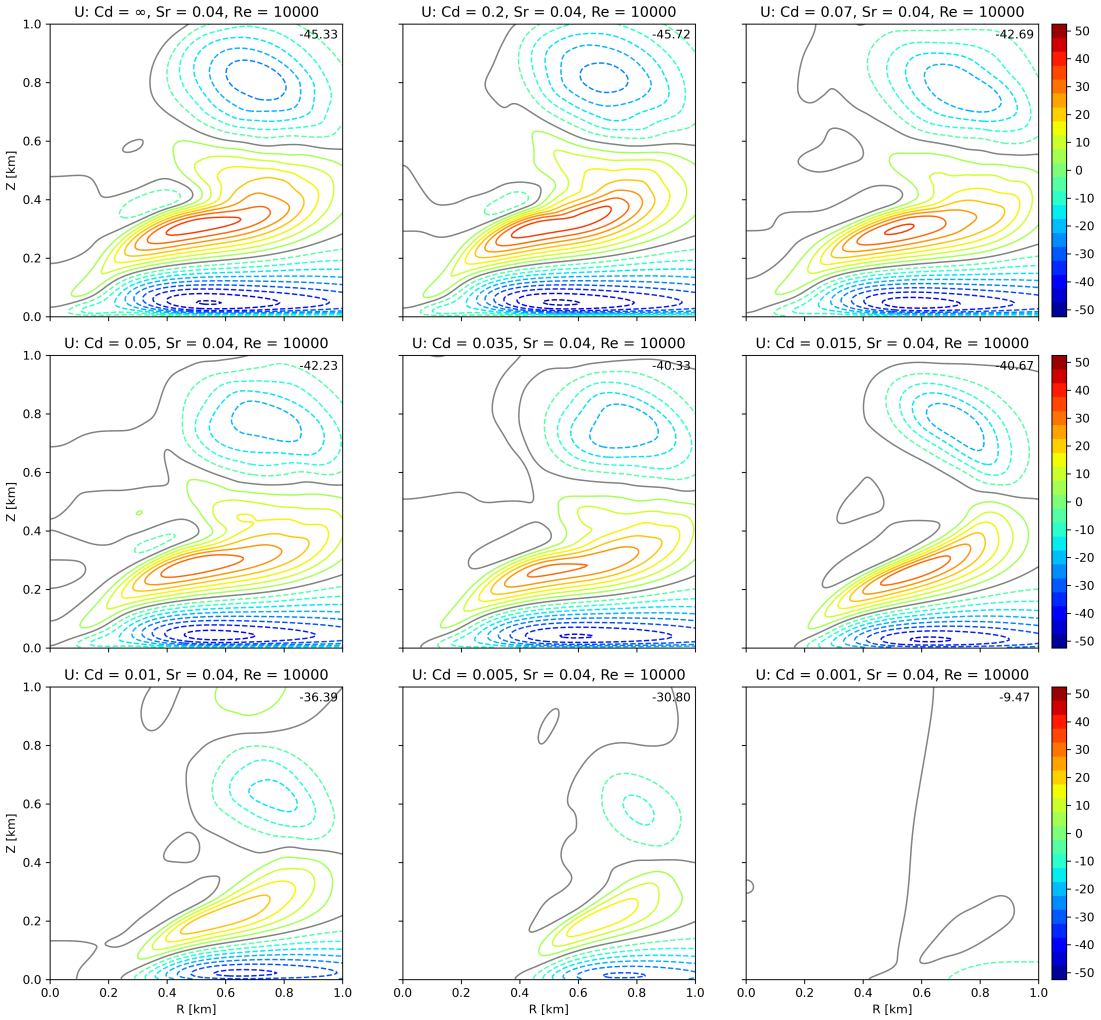


**Figure 4.47:** Radial velocity contourlines in the corner region $[(0,0),(1,1)]$ for $S_r = 0.04$, $R_e = 10000$ and semi-slip boundary conditions. Zero contourline in grey.

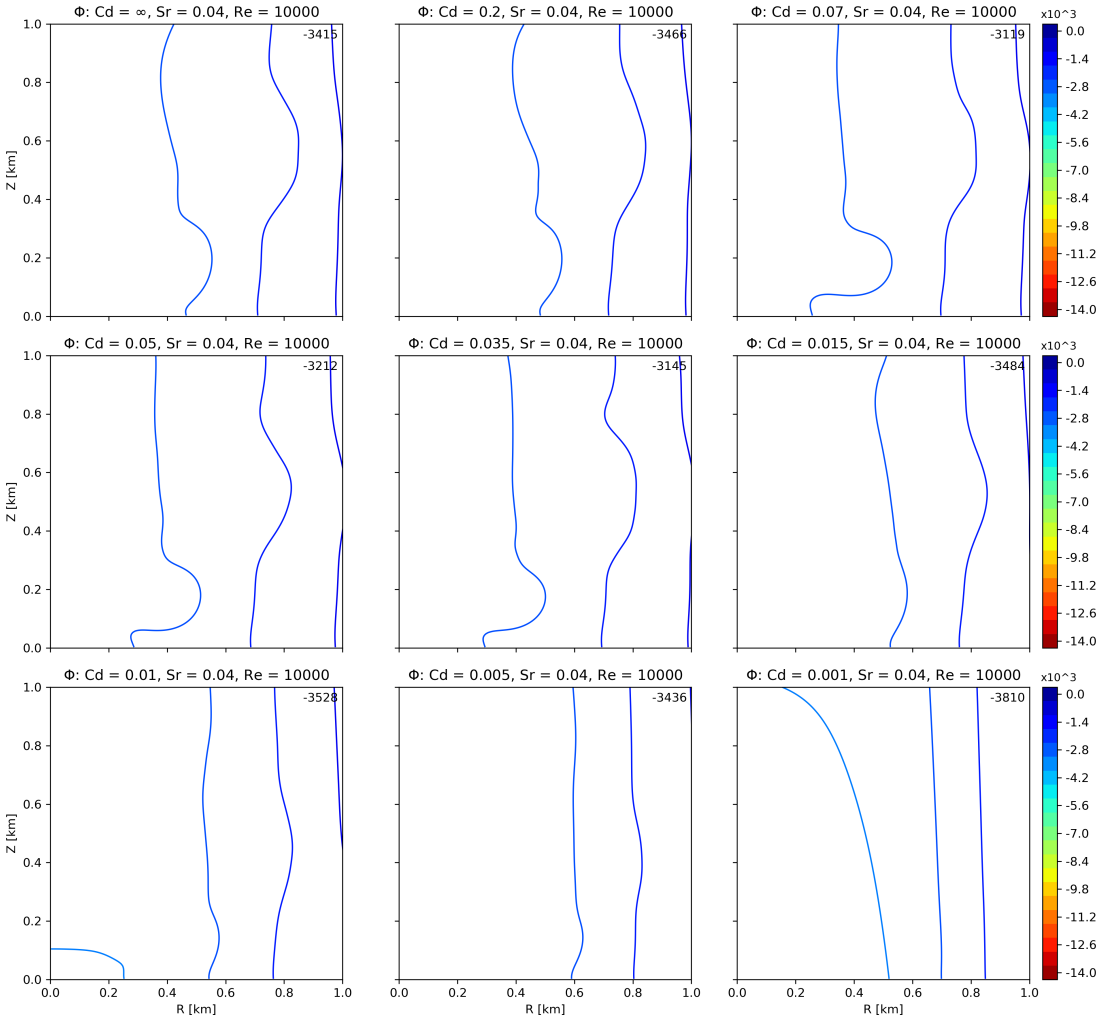


**Figure 4.48:** Pressure conturlines in the corner region $[(0,0),(1,1)]$ for $S_r = 0.04$, $R_e = 10000$ and semi-slip boundary conditions.

The first panel illustrates how the maximum tangential velocity remains mostly unchanged over the majority of the $C_d$ range, with only a small weakening for smaller $C_d$. The steepest decline happens for very low friction, with $v$ converging to the free-slip value. As previously mentioned, the maximum swirling velocity tends to slowly translate away from the origin, as a consequence of the enlargement of the vortex for diminishing $C_d$. Additionally, the vertical position shifts downward, in accordance with the observed narrowing of the vortex core.

The maximum inflow undergoes a slow weakening under decreasing friction, before a sharp decrease in magnitude towards free-slip conditions. The narrowing of the frictional inflow layer, as $C_d$ approaches zero, is evident from the decreasing $z$ of the minimum radial velocity, while the increase of the radial position confirms the outward shift of the inflow due to the vortex broadening. Similarly, the third panel reveals that the vertical velocity remains approximately stable under diminishing friction, before a steep decline to the free-slip case, characterized by a significantly reduced updraft. Analogous results emerge from the $\phi$ and $H$ fields, which show stable extrema over the entire range of $C_d$ values.

Finally, as for $S_r = 0.005$ and $S_r = 0.01$, $-u \cdot r$ remains approximately steady as friction diminishes, until $C_d = 0.001$, for which the lower tier of the potential vortex boundary layer vanishes, and the maximum inflow mass flux rapidly goes to zero. It is remarkable that the behavior of the maximum of $-u \cdot r$ is almost identical for the three cases, despite these describing different situations, due to the fact that the corresponding no-slip solutions represent different vortex structures. The reason for this similarity is that this physical quantity is related to the potential vortex boundary layer, which, as demonstrated in the previous section, is preserved for all three swirl ratios from $C_d = 0.2$ to $C_d = 0.005$. However, for $C_d = 0.001$, the lower, frictional tier vanishes and the assumption of potential vortex boundary layer is no longer valid; the decay of the inflow is evidenced by the sharp decrease in $-u \cdot r$.

### Final remarks on the role of $C_d$ on the structure of the vortex

The analysis of semi-slip simulations reveals that the friction coefficient is a fundamental parameter in determining the structure of a vortex, suggesting that under semi-slip conditions the parameter space depicted in figure 4.30 is, in fact, three-dimensional, with $C_d$ being the third dimension. The results indicate that a decrease in $C_d$ for fixed $S_r$ and $R_e$ induces the same one-celled to two-celled transition that occurs for an increase in $S_r$ for fixed $R_e$ and under no-slip conditions. The behavior is schematically represented in figure 4.50: a decrease in $C_d$ results in the same structural changes caused by an increase in $S_r$. A single-celled vortex undergoes vortex breakdown and transitions to a two-celled structure for increasing swirl ratio (from left to right along the rows), as well as for decreasing friction coefficient (from top to bottom along the columns). For fixed $R_e$, the structure of a vortex is defined by the position of its solution in the $S_r$ - $C_d$

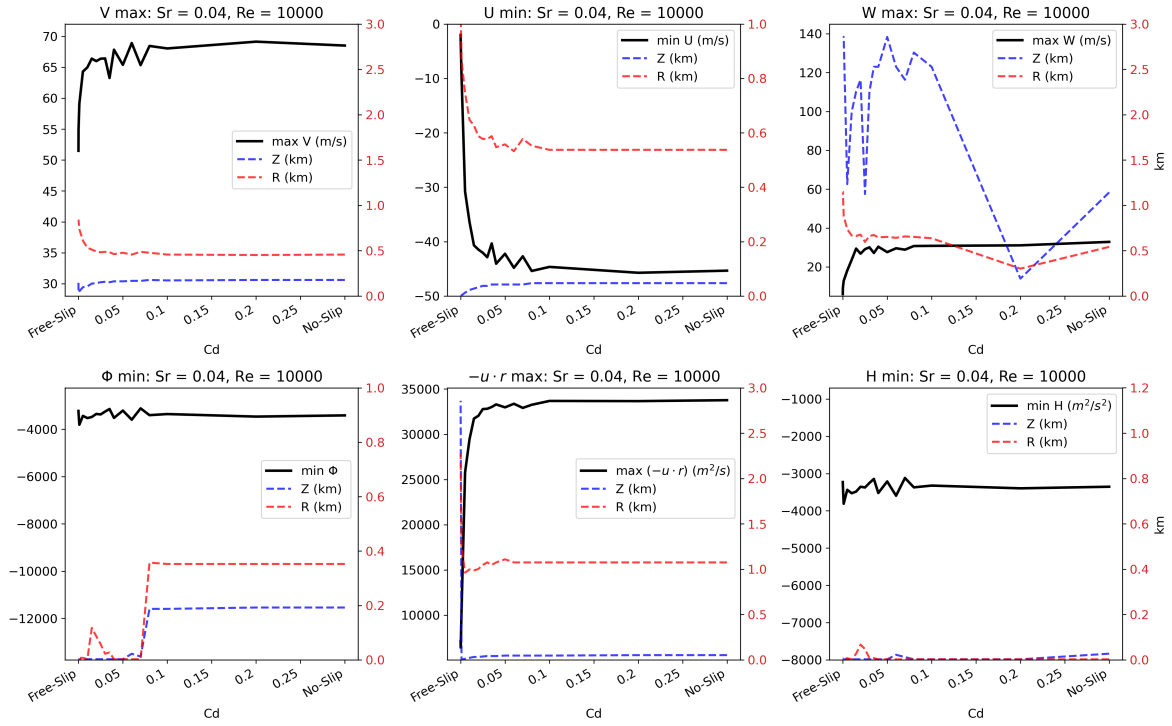


**Figure 4.49:** $S_r = 0.04$, $R_e = 10000$: extrema of $v$, $u$, $w$, $\phi$, $-u \cdot r$, $H$, and their position ($r$, $z$) for boundary conditions ranging from no-slip to free-slip.

parameter space. A possible consequence of this result is that the potential vortex line, described in [Rot+16], might be a slanted surface in the three-dimensional parameter space. However, it is important to remark that in this work we studied the consequences of semi-slip conditions for only three $S_r - R_e$ combinations. Therefore, further research is needed to assess the details of this three-dimensional parameter space.

## 4.4 Analysis of the corner region

In the previous section, we highlighted how a decrease in friction for the $S_r = 0.005$ and $S_r = 0.01$ semi-slip simulations causes an intensification of all the fields in the vicinity of the origin ($0 < r < 0.2$ km, $0 < z < 0.2$ km), as long as the solution has not reached a full two-celled structure. In particular, for $S_r = 0.005$ this intensification leads to a peak in intensity of all fields, with magnitudes larger than the extrema of both the no-slip and free-slip cases, illustrating that within a certain range of $C_d$ values the employment of semi-slip conditions can lead to an intensification of the vortex. Unfortunately, the study of this region of the domain is challenging, due to the stationarity of the solution and the fact that almost every term of the Navier-Stokes equation is important. The

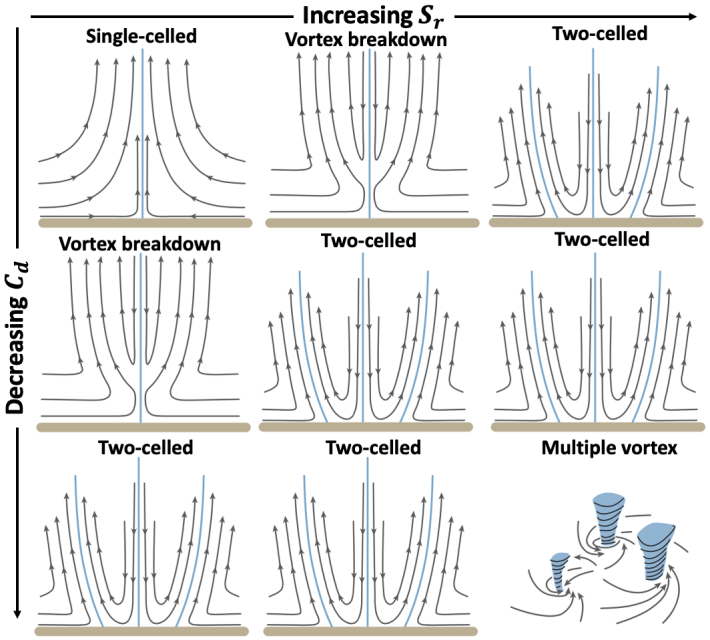


**Figure 4.50:** Schematic diagram of the vortex structures in the $S_r$ - $C_d$ parameter space. A decrease in $C_d$ (from top to bottom) results in the same transitions as an increase in $S_r$ (from left to right).

region near the origin must reflect the properties of the radial inward flow that is located upstream, therefore we can focus on the region of the inflow instead. As we have seen in the previous sections, the inflow is located within the region $[(0,0),(1,1)]$ of the domain, which we defined as the corner region. In previous studies, the corner region has not been defined by a strict set of coordinates, but rather as the region of the domain where both the radial and vertical pressure gradients are significantly different from zero. This property is indeed true in the region $[(0,0),(1,1)]$ (figures 4.35,4.42), therefore we can consider the study of the role of friction on the inflow and its consequences on the vicinity of the origin as the analysis of the corner region of the vortex.

### Derivation of a simplified set of equations

Since the horizontal diffusion for both the radial and tangential components of the Navier-Stokes equations is negligible for $r > 0.25$ km, we can work with simplified equations limiting ourselves to the region $r > 0.25$ km. We will now obtain a simplified set of equations to study the situation. We start with the radial component of the cylindrical Navier-Stokes equations (u-equation):

$$\frac{du}{dt} = -\frac{\partial \phi}{\partial r} + 2\Omega v + \frac{v^2}{r} + \frac{1}{\rho}\frac{\partial \tau_{rz}}{\partial z} + \frac{1}{\rho}\frac{\partial \tau_{rr}}{\partial r}, \tag{4.3}$$

where $-\frac{\partial \phi}{\partial r}$ is the gradient of the pressure divided by a constant density $\phi = p/\rho$, $2\Omega v$ the Coriolis acceleration, $\frac{v^2}{r}$ the centrifugal acceleration, $\frac{1}{\rho}\frac{\partial \tau_{rz}}{\partial z}$ the vertical diffusion, and $\frac{1}{\rho}\frac{\partial \tau_{rr}}{\partial r}$ the horizontal diffusion. Once the simulation has reached a steady state, the Coriolis component becomes numerically negligible with respect to the other terms of the equation. The horizontal diffusion is negligible for $r > 0.25$ km. Therefore, limiting ourselves to the region of the domain $r > 0.25$ km, we can assume the u-equation to be:

$$\frac{du}{dt} = -\frac{\partial \phi}{\partial r} + \frac{v^2}{r} + \frac{1}{\rho}\frac{\partial \tau_{rz}}{\partial z}. \tag{4.4}$$

For simplicity, we will define $\frac{\partial \phi}{\partial r} = P$, and $\frac{v^2}{r} = C$:

$$\frac{du}{dt} = [-P + C] + \frac{1}{\rho}\frac{\partial \tau_{rz}}{\partial z}. \tag{4.5}$$

We note that when $P > C$ the pressure gradient drives an inward radial flow, whereas for $P < C$ the centrifugal acceleration drives an outward radial flow. Now we take a vertical average, integrating between $z = 0$ and $z = \delta$, where $\delta$ is the height at which the lower tier of the boundary layer ends. We have seen in section 4.1.2 that the upper limit of the lower layer (frictional layer) is the height of the maximum of $-ur$, therefore characterized by $\frac{\partial u}{\partial z} = 0$. The average yelds:

$$\overline{\frac{du}{dt}} = [-\bar{P} + \bar{C}] + \frac{1}{\delta\rho}\int_0^\delta \frac{\partial \tau_{rz}}{\partial z}\, dz, \tag{4.6}$$

where

$$\bar{(...)} = \frac{1}{\delta}\int_0^\delta (...)\, dz. \tag{4.7}$$

Solving the integral, we obtain:

$$\frac{1}{\delta\rho}\int_0^\delta \frac{\partial \tau_{rz}}{\partial z}\, dz = \frac{1}{\delta\rho}\left(\tau_{rz}\Big|_{z=\delta} - \tau_{rz}\Big|_{z=0}\right). \tag{4.8}$$

Substituting the formulation for $\tau_{rz}\Big|_{z=\delta}$, we notice that:

$$\tau_{rz}\Big|_{z=\delta} = \nu\rho\frac{\partial u}{\partial z}\Big|_{z=\delta} = 0 \tag{4.9}$$

since $\frac{\partial u}{\partial z}\Big|_{z=\delta} = 0$. The vertical average allows us to simplify the equation, limiting the vertical diffusion to its surface contribution. In the present work, the model computes $\tau_{rz}\Big|_{z=0}$ under semi-slip conditions as:

$$\tau_{rz}\Big|_{z=0} = \rho u_*^2 \frac{u}{V}\Big|_{z=0}, \tag{4.10}$$

where $V$ is the surface velocity

$$V = \sqrt{u^2 + v^2}\Big|_{z=0}, \tag{4.11}$$

and $u_*$ is the friction velocity, computed by the model as

$$u_* = \frac{V\kappa}{\ln \frac{2.5+z_0}{z_0}}. \tag{4.12}$$

In equation (4.12), $\kappa = 0.40$ is the von Kármán constant, 2.5 meters is the height of the first grid point, where this calculation is carried out, and $z_0$ is the roughness length ([LP64] chapter 3.3)

$$z_0 = \frac{10}{\exp\left(\frac{\kappa}{\sqrt{C_d}}\right) - 1} \tag{4.13}$$

where 10 appears because the estimate of $z_0$ is conventionally carried out at 10 meters. Substituting, equation (4.6) becomes:

$$\overline{\frac{du}{dt}} = [-\bar{P} + \bar{C}] - \frac{1}{\delta} u_*^2 \frac{u}{\sqrt{u^2 + v^2}}\Big|_{z=0}. \tag{4.14}$$

Equation (4.14) can be written in a more concise way by using the property $u_*^2 = C_d V^2$ ([LP64] chapter 3.3):

$$\overline{\frac{du}{dt}} = [-\bar{P} + \bar{C}] - \frac{1}{\delta}(C_d V u)\Big|_{z=0}. \tag{4.15}$$

It is worth highlighting the formulation of the vertical diffusion in equation (4.15), with $C_d$ multiplying $V$. A decrease in friction increases the surface velocity $V$ while decreasing $C_d$. The outcome of a decrease in friction is therefore non-trivial, with the behaviors of $C_d$ and $V$ in opposition.

Moving to the tangential component of the cylindrical Navier-Stokes equations ($\Gamma$-equation):

$$\frac{dv}{dt} = -\frac{uv}{r} - 2\Omega u + \frac{1}{\rho}\frac{\partial \tau_{r\theta}}{\partial r} + \frac{1}{\rho}\frac{\partial \tau_{\theta z}}{\partial z}, \tag{4.16}$$

where $-\frac{uv}{r}$ is the centrifugal acceleration, $-2\Omega u$ the Coriolis acceleration, $\frac{1}{\rho}\frac{\partial \tau_{\theta z}}{\partial z}$ the vertical diffusion, and $\frac{1}{\rho}\frac{\partial \tau_{r\theta}}{\partial r}$ the horizontal diffusion. As for the u-equation, the Coriolis term is negligible, and the horizontal diffusion is negligible for $r > 0.25$ km. Therefore, we can assume the $\Gamma$-equation to be:

$$\frac{dv}{dt} = -\frac{uv}{r} + \frac{1}{\rho}\frac{\partial \tau_{\theta z}}{\partial z}, \tag{4.17}$$

Multiplying by $r$ and rearranging:

$$\begin{aligned} r\frac{dv}{dt} + uv &= \frac{r}{\rho}\frac{\partial \tau_{\theta z}}{\partial z}, \\ r\frac{dv}{dt} + v\frac{dr}{dt} &= \frac{1}{\rho}\frac{\partial (r\tau_{\theta z})}{\partial z}, \\ \frac{d(rv)}{dt} &= \frac{d\Gamma}{dt} = \frac{1}{\rho}\frac{\partial (r\tau_{\theta z})}{\partial z}. \end{aligned} \tag{4.18}$$

We can now take the vertical average, using the operator in equation (4.7), and employing the formulations of $\tau$ described for the u-equation (equation (4.9) and (4.10))

$$\overline{\frac{d\Gamma}{dt}} = \frac{1}{\delta}\left(\nu \frac{\partial \Gamma}{\partial z}\Big|_{z=\delta} - u_*^2 \frac{\Gamma}{\sqrt{u^2+v^2}}\Big|_{z=0}\right), \tag{4.19}$$

which can be written in a more concise way

$$\overline{\frac{d\Gamma}{dt}} = \frac{1}{\delta}\left(\nu \frac{\partial \Gamma}{\partial z}\Big|_{z=\delta} - (C_d V \Gamma)\Big|_{z=0}\right). \tag{4.20}$$

Combining equations (4.14) and (4.19) we obtain the set of equations employed in this section:

$$\begin{cases} \overline{\frac{du}{dt}} = [-\bar{P} + \bar{C}] - \frac{1}{\delta} u_*^2 \frac{u}{\sqrt{u^2+v^2}}\Big|_{z=0} \\ \overline{\frac{d\Gamma}{dt}} = \frac{1}{\delta}\left(\nu \frac{\partial \Gamma}{\partial z}\Big|_{z=\delta} - u_*^2 \frac{\Gamma}{\sqrt{u^2+v^2}}\Big|_{z=0}\right) \end{cases} \tag{4.21}$$

It must be remarked that the use of the $\frac{\partial u}{\partial z}\Big|_{z=\delta} = 0$ property of the frictional layer's upper limit does not imply that the equations are valid only in the potential vortex region, we only need the two-tiered structure of the boundary layer to exist, so that $\frac{\partial u}{\partial z}\Big|_{z=\delta} = 0$ is true. Indeed, this two-tiered structure exists, figure 4.51 shows an example for $S_r = 0.005$ and $C_d = 0.2$. The plot evidences that the boundary layer does not exhibit the radial behavior of a potential vortex boundary layer, as the lower tier has almost the same thickness for $z = 0.25$, $z = 0.5$, and $z = 1$ km, in agreement with the results of sections 4.1.2 and 4.2, where the potential vortex region was always found to extend from $r > 1$ km. This property of $\delta \approx const$ is useful, allowing to employ a fixed upper limit of integration $\delta$. The black horizontal line in figure 4.51 represents the height of the upper limit of the lower tier for $r = 0.25$ km, which is the same for $r = 0.5$ km, while the height for $r = 1$ km differs by only one grid spacing. More generally, for any fixed $C_d$ value between 0.2 and 0.035, $\delta$ does not vary by more than two grid points through the $0.25 < r < 1$ km range for $S_r = 0.005$ and $S_r = 0.01$. This property is degraded for

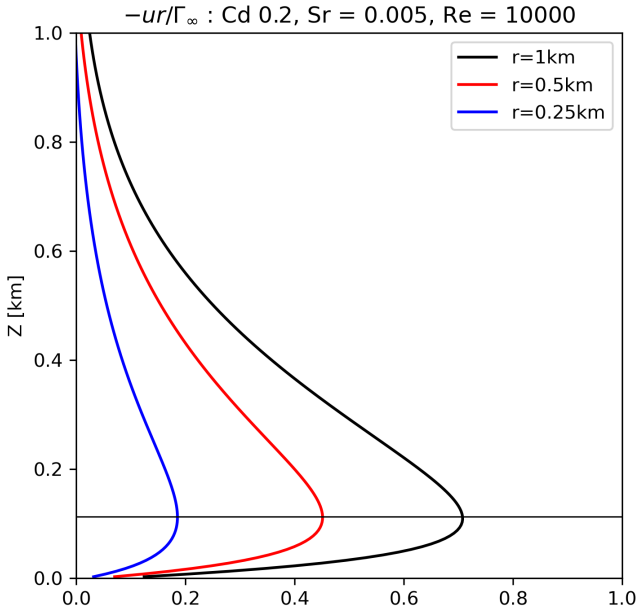


**Figure 4.51:** $S_r = 0.005$, $R_e = 10000$ and $C_d = 0.2$: vertical profiles of $-ur/\Gamma_\infty$ sampled at $r = 0.25$, $r = 0.5$, and $r = 1$km. The black line illustrates the height of the lower tier for $r = 0.25$ and $r = 0.5$ km.

$C_d < 0.035$, therefore we limit the analysis to the $0.035 \leq C_d \leq 0.2$ range. We note that for these values of friction coefficient the $S_r = 0.005$ simulations represent a single-celled vortex, whereas for $S_r = 0.01$ the vortex undergoes breakdown. We further limit the domain of the analysis to $0.25 < r < 0.95$ km to avoid the numerical noise caused by the change in grid spacing that occurs at $r = 1$ km.

In the first of equations (4.21), we will define $term_1 = [-\bar{P} + \bar{C}]$, which represents the sum of the radial pressure gradient and the centrifugal acceleration. The contribution of surface friction to the u-equation $-\frac{1}{\delta}u_*^2 \frac{u}{\sqrt{u^2+v^2}}\Big|_{z=0}$ will be defined $term_2$. The sum of these two terms represents the vertical average of the total derivative of $u$: $\overline{\frac{du}{dt}}$. In the second equation, we will define $term\text{-}z_1 = \frac{\nu}{\delta}\frac{\partial \Gamma}{\partial z}\Big|_{z=\delta}$, while the contribution of surface friction to the $\Gamma$-equation will be defined $term\text{-}z_0 = -\frac{u_*^2}{\delta}\frac{\Gamma}{\sqrt{u^2+v^2}}\Big|_{z=0}$. The sum of $term\text{-}z_1$ and $term\text{-}z_0$ represents the vertical average of the total derivative of $\Gamma$: $\overline{\frac{d\Gamma}{dt}}$. In the u-equation, $\overline{\frac{du}{dt}} = \overline{\left(u\frac{\partial u}{\partial r} + w\frac{\partial u}{\partial w}\right)}$ and we empirically find that $|u\frac{\partial u}{\partial r}| \gg |w\frac{\partial u}{\partial w}|$ in the region of interest. Thus $\overline{\frac{du}{dt}} = \overline{\left(u\frac{\partial u}{\partial r}\right)}$ and $u < 0$ for the inflow, thus a negative value of the sum indicates an intensification of the inflow moving inward. The radius for which the sum is zero gives an indication of the radial position of the inflow's strongest region. Moving inwards from $r = 0.95$ km we expect a negative value of $\overline{\frac{du}{dt}}$, which eventually decreases to zero, before

attaining positive values in the stagnation area, where the inflow is stopped and turned. We anticipate $term_1$ to be negative where the pressure gradient drives the inwards flux, and positive in the stagnation area, where the flow is gradually stopped. Being the surface friction, $term_2$ is expected to be always positive, as it opposes to the inward flow. In the $\Gamma$-equation $\frac{\overline{d\Gamma}}{dt} = \overline{\left(u\frac{\partial\Gamma}{\partial r} + w\frac{\partial\Gamma}{\partial w}\right)}$ and we empirically find that $|u\frac{\partial\Gamma}{\partial r}| \gg |w\frac{\partial\Gamma}{\partial w}|$ in the region of interest. Thus $\frac{\overline{d\Gamma}}{dt} = \overline{\left(u\frac{\partial\Gamma}{\partial r}\right)}$ and since $u < 0$ and $\Gamma$ decreases moving inward, we expect the sum to be always negative. The angular momentum increases with height, thus we anticipate $term\text{-}z_1$ to be always positive. Finally, $term\text{-}z_0$ is the dissipation of angular momentum, hence it is a negative quantity.

### Analysis of the corner region for $S_r = 0.005$

Figure 4.52 presents the terms of equations (4.21) for $S_r = 0.005$. In the left column, the u-equation is described by plotting $term_1$ in blue, $term_2$ in orange, and the sum of the two terms in magenta. In the right column, the $\Gamma$-equation is depicted with $term\text{-}z_1$ in blue, $term\text{-}z_0$ in orange, and the sum of the terms in magenta. The first row is for $C_d = 0.2$, the second for $C_d = 0.05$, and the last one for $C_d = 0.035$.

Scanning the first column vertically, we note how the point where the the sum intersects with zero is shifted to lower radii. Since a negative sign for $\frac{\overline{du}}{dt}$ identifies a strengthening of the inflow, the shift reveals how the decrease in friction enables the inflow to reach deeper in the corner region, closer to the origin. A similar shift is observed for the minimum of $\frac{\overline{du}}{dt}$, indicating that the maximum strengthening occurs closer to the origin. Moreover, the magnitude of the minimum total derivative of $\bar{u}$ increases significantly for decreasing friction, going from $-0.072\ m/s^2$ at $C_d = 0.2$ to $-0.120\ m/s^2$ at $C_d = 0.05$, and finally to $-0.169\ m/s^2$ at $C_d = 0.035$. These results suggest that a decrease in friction causes the inflow to intensify and move closer to the origin. Notably, $term_2$ decreases towards the origin for $C_d = 0.2$, whereas it increases for $C_d = 0.035$. Since $term_2$ depends only on $C_d$ and surface velocity, for constant $C_d$ the variation is due to the behavior of the surface velocity, indicating that for decreasing friction the surface velocity near the origin increases.

The negative value of $\frac{\overline{d\Gamma}}{dt}$ (magenta line) indicates dissipation of angular momentum as parcels are advected towards the origin by the inflow. The second column of figure 4.52 shows that the dissipation of $\bar{\Gamma}$ becomes more intense as friction diminishes. The fact that the dissipation of $\bar{\Gamma}$ becomes larger as $C_d$ diminishes suggests that the inflow brings parcels with larger $\Gamma$ towards the origin. From equation (4.20) we see that $term\text{-}z_0$ depends on $\Gamma$, a larger magnitude reflects a larger value of $\Gamma$. This can be appreciated in figure 4.55, showing the $\Gamma$ field for $S_r = 0.005$ under no-slip conditions (left) and semi-slip conditions with $C_d = 0.035$ (right): the value of $\Gamma$ near the origin ([0,0],[0.2,0.2]) becomes significantly larger for lower friction coefficient. It is worth highlighting that while for $C_d = 0.2$ the magnitude of $\frac{\overline{d\Gamma}}{dt}$ decreases slightly as $r \to 0$, for $C_d = 0.035$ it remains steady. The decrease for $C_d = 0.2$ indicates that at $r = 0.25$ km the parcel's

angular momentum approaches zero, and therefore the rate of decrease weakens, whereas for $C_d = 0.035$ the angular momentum at $r = 0.25$ km is still significant, and the rate of decrease is steady. It is useful to compute the values of $\frac{\overline{d\Gamma}}{dt}$ for the three $C_d$ cases at $r = 0.25$ km: $\frac{\overline{d\Gamma}}{dt}$ decreases from $-1.964$ $m^2/s^2$ at $C_d = 0.2$ to $-5.392$ $m^2/s^2$ at $C_d = 0.05$, before reaching $-9.692$ $m^2/s^2$ at $C_d = 0.035$. These outcomes illustrate the robust decrease of $\frac{\overline{d\Gamma}}{dt}$ near the origin, evidencing that parcels with large angular momentum are advected near the origin.

We have emphasized in section 4.1.2 how vertical diffusion plays a crucial role in balancing the pressure gradient at the surface, resulting in the presence of an inflow. A natural consequence is that a reduction in friction weakens the inflow, and in the limit to free-slip ($C_d \to 0$) the inflow disappears, as was shown in section 4.3. While, for $S_r = 0.005$, this inflow reduction occurs for very low values of friction (as evidenced in figure 4.36 by the sharp increase towards zero of $u$ as $C_d \to 0$ after the peak), in the range $C_d = 0.2 - 0.035$ a decrease in friction causes the surface velocity to increase substantially, boosting the contribution of $term_2$ in the u-equation, thus strengthening the inflow. Simultaneously, a reduction in friction implies that less angular momentum is dissipated across the inflow, and parcels with larger $\Gamma$ are advected towards the origin. Let us assume for simplicity that a decrease in friction causes the angular momentum to be conserved across the inflow: since $\Gamma = rv$, as the parcels flow towards the origin, the tangential velocity increases as the radius decreases, and the closer the parcels are advected to the origin, the more the swirling motion is enhanced. Naturally, $\Gamma$ is not conserved across the inflow, but the advection by the inflow of parcels with large $\Gamma$ near the origin produces the same increase in rotational velocity. This effect is clearly evident in figure 4.32, which shows the progressive intensification of the $v$ field in the vicinity of the origin. The intensification and shift towards the origin of the inflow in the range $C_d = 0.2 - 0.035$ was observed examining the $u$ field (figure 4.34) and the extrema of the inflow (figure 4.36) in section 4.3. The presence of a stronger inflow closer to the origin implies that air flowing inward is forced to perform a tighter turn close to the origin, as evidenced by the streamlines of figure 4.31. Moreover, the tighter turn produces a funneling effect which, together with the stronger inflow, contributes to considerably intensify the updraft, explaining the intensification observed for $S_r = 0.005$ (figures 4.33 and 4.36).

These findings suggest that semi-slip conditions are characterized by two competing effects: the decrease of $C_d$ tends to weaken the inflow while allowing the surface velocity to attain larger values. Since in the u-equation (4.15) the surface vertical diffusion is in the form $-C_d \cdot V \cdot u\Big|_{z=0}$, the competing effect is illustrated by the multiplication of the friction coefficient with the surface velocity. The results presented in figure 4.52 show that within a certain range of $C_d$ values, a decrease in friction results in a strengthening of the inflow, which due to the reduced friction brings parcels with larger angular momentum near the origin. Therefore, the competing effects give rise to a peak in intensity of all

fields, explaining the peaking behavior of the extrema shown in figure 4.36.

### Analysis of the corner region for $S_r = 0.01$

In section 4.3, the extrema of the fields for $S_r = 0.01$ (figure 4.43) did not exhibit the same peaking behavior as for $S_r = 0.005$. Instead, the maximum tangential velocity and the minimum radial velocity showed marginal weakening of the swirling motion and the inflow. It is therefore interesting to perform the same analysis on the $S_r = 0.01$ simulations. In stark contrast with the $S_r = 0.005$ case, the left column of figure 4.53 shows marginal changes in the $\overline{\frac{du}{dt}}$ profile. The point where the sum intersects with zero does not shift towards the origin for decreasing friction; instead, it shows a marginal translation to larger radius. The magnitude of the minimum of $\overline{\frac{du}{dt}}$ shows minimal variation, going from $-0.598\ m/s^2$ at $C_d = 0.2$ to $-0.519\ m/s^2$ at $C_d = 0.05$, and to $-0.575\ m/s^2$ at $C_d = 0.035$. Therefore, for $S_r = 0.01$ the competing effects do not cause an intensification of the inflow, which instead remains mostly unchanged. On the other hand, the right column illustrates that a decrease in friction causes an increase in the magnitude of $\overline{\frac{d\Gamma}{dt}}$, similar to the $S_r = 0.005$ case. Quantitatively, $\overline{\frac{d\Gamma}{dt}}$ at $r = 0.25$ km diminishes from $-8.095\ m^2/s^2$ at $C_d = 0.2$ to $-15.293\ m^2/s^2$ at $C_d = 0.05$, before reaching $-20.213\ m^2/s^2$ at $C_d = 0.035$. As for $S_r = 0.005$, a reduction in friction results in lower angular momentum dissipation across the inflow. However, while for $S_r = 0.005$ the intensification and shift towards the origin of the inflow cause the magnitude of $\overline{\frac{d\Gamma}{dt}}$ at $r = 0.25$ km to increase by 5 times from $C_d = 0.2$ to $C_d = 0.035$, for $S_r = 0.01$ the increase in the same range of $C_d$ is only by 2.5 times, due to the lack of inflow strengthening. The fact that for both $S_r = 0.005$ and $S_r = 0.01$ a decrease in friction leads to parcels attaining larger values of angular momentum near the origin explains the observed increase in tangential velocity in the vicinity of the origin.

The present analysis confirms the differences between the $S_r = 0.005$ and $S_r = 0.01$ semi-slip simulations observed in section 4.3. While for $S_r = 0.005$ the inflow intensifies and shifts towards the origin for decreasing friction within the range $C_d = 0.2 - 0.035$, for $S_r = 0.01$ the inflow remains mostly unchanged. The occurrence of the inflow strengthening and shift appears to be related to the value of the swirl ratio. In particular, it is possible that this peculiar behavior is related to the structure of the vortex, which, as demonstrated in [Rot+16], is a direct consequence of the $S_r$ value, as the position of the $S_r$ - $R_e$ combination in the parameter space determines the vortex structure. In fact, we have emphasized the different vortex structures of the two cases: while for $S_r = 0.005$ the vortex is single-celled up to $C_d = 0.03$, for $S_r = 0.01$ the vortex undergoes breakdown throughout the $C_d$ range examined. As mentioned in section 4.3, since the vortex breakdown for $S_r = 0.01$ occurs for the highest $C_d$ value employed in this study, it is unclear if the inflow strengthening happens for higher friction. In order to better understand this phenomenon, more simulations are needed. In particular, the present results suggest that investigating the range $S_r = 0.005 - 0.01$ can provide

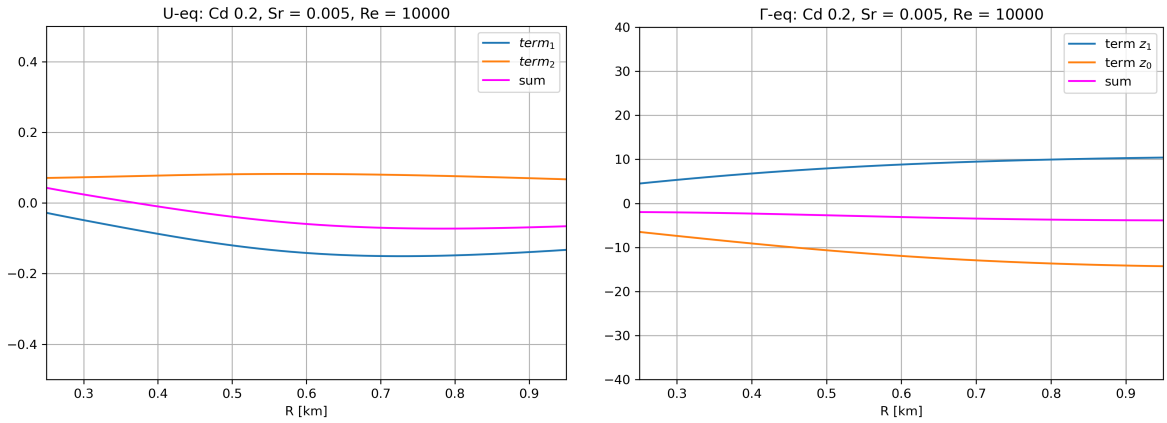


(a)




(b)

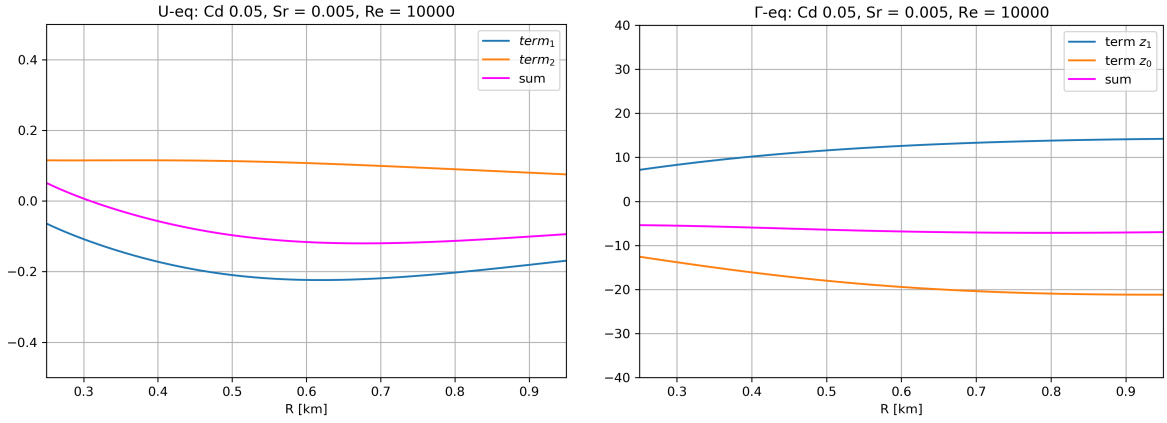


(c)




(d)

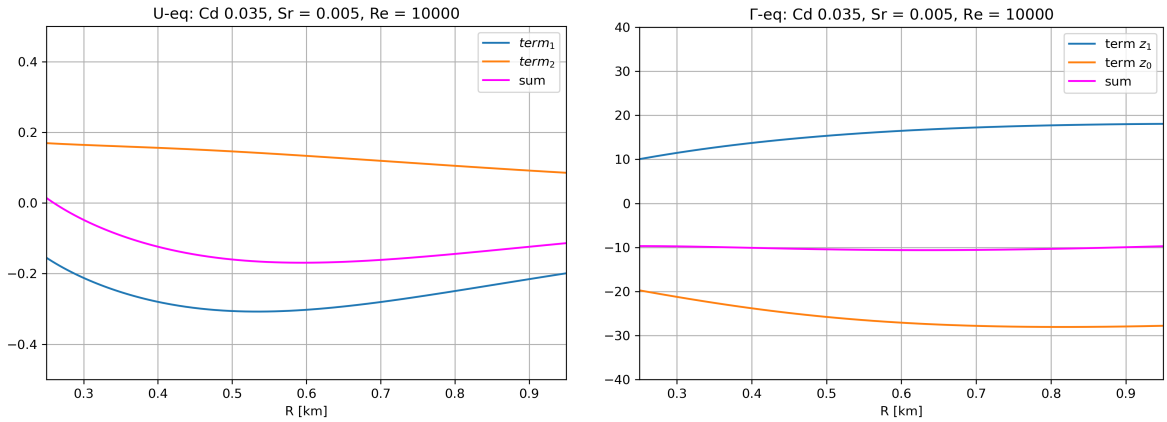


(e)




(f)

**Figure 4.52:** $S_r = 0.005$, $R_e = 10000$: u-equation for a) $C_d = 0.2$ c) $C_d = 0.05$, and e) $C_d = 0.035$ $[m/s^2]$; Γ-equation for b) $C_d = 0.2$ d) $C_d = 0.05$, and f) $C_d = 0.035$ $[m^2/s^2]$.

important information on the matter.

### Final remarks on the vortex intensification for decreasing $C_d$

The study of the semi-slip simulations for $S_r = 0.005$ has highlighted that a decrease in friction in the range $C_d = 0.2 - 0.035$ leads to an intensification of the vortex. The strengthening has been attributed to the combined effects of the friction decrease: the intensification and shift towards the origin of the inflow, and the advection of larger values of $\Gamma$ due to reduced dissipation. Figure 4.54 shows a schematic diagram of the process. The inflow becomes stronger for lower $C_d$, enhancing the updraft downstream. Moreover, the shift towards the origin forces the inflow to turn more tightly, resulting in a funneling effect that further intensifies the updraft. Simultaneously, the decrease in friction leads to smaller $\Gamma$ dissipation, hence the inflow advects larger values of angular momentum near the origin, causing the rotation to significantly intensify in the vicinity of the origin. This phenomenon is evident from figure 4.55, which shows the angular momentum field in the region $[(0, 0), (0.2, 0.2)]$, near the origin, for no-slip conditions (4.55a) and semi-slip with $C_d = 0.035$ (4.55b): a decrease in friction leads to a considerable increase in $\Gamma$ in the vicinity of the origin.

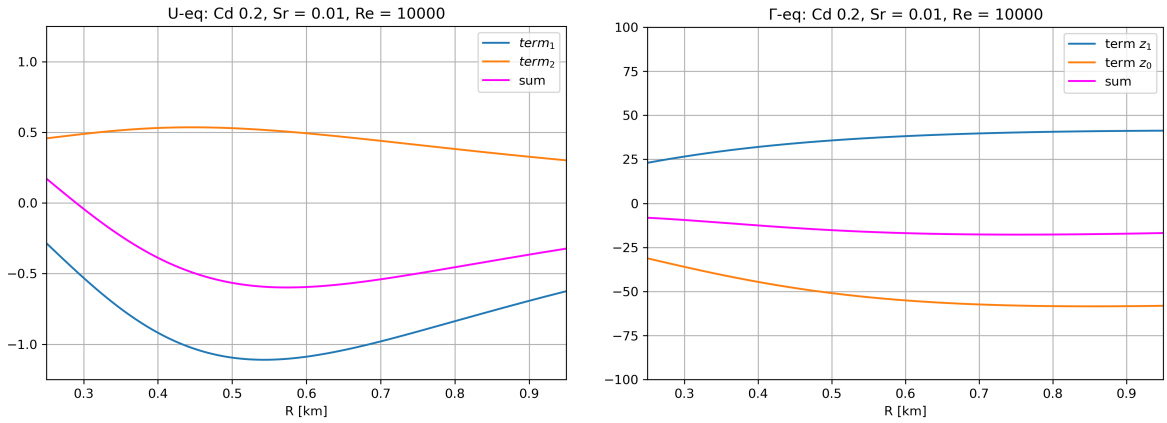


(a)




(b)

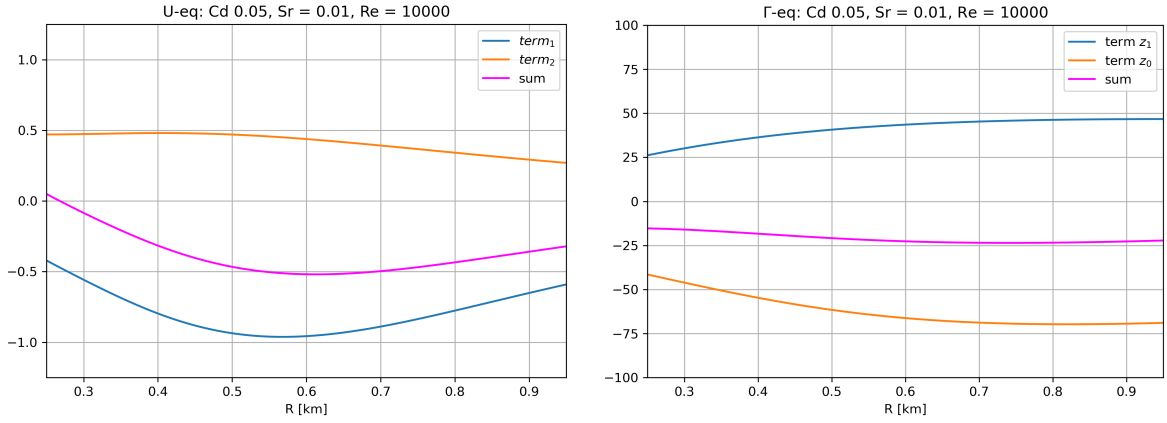


(c)




(d)

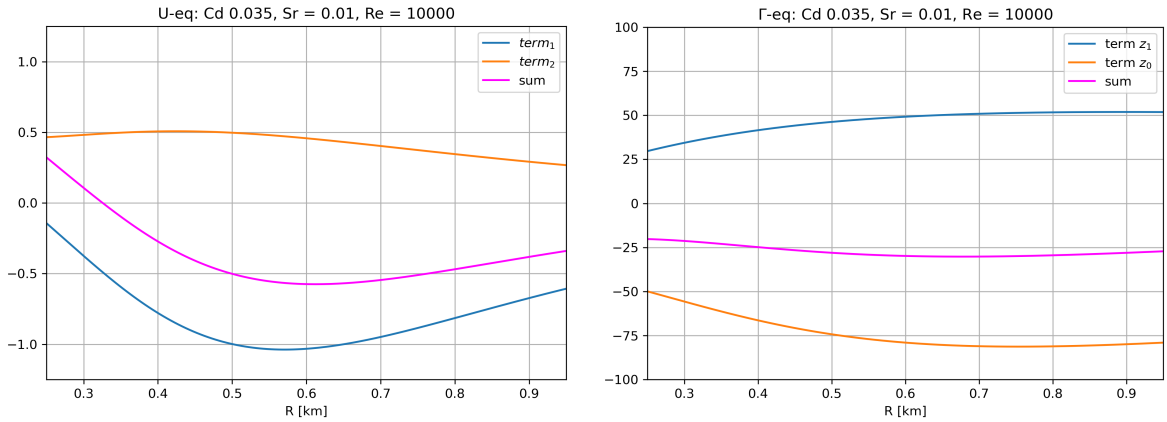


(e)




(f)

**Figure 4.53:** $S_r = 0.01$, $R_e = 10000$: u-equation for a) $C_d = 0.2$ c) $C_d = 0.05$, and e) $C_d = 0.035$ $[m/s^2]$; Γ-equation for b) $C_d = 0.2$ d) $C_d = 0.05$, and f) $C_d = 0.035$ $[m^2/s^2]$.

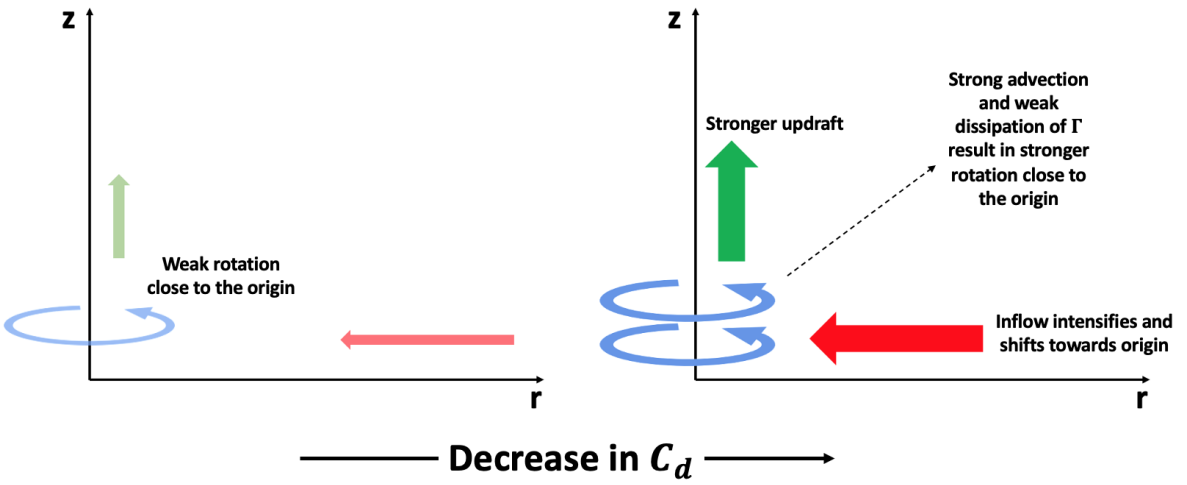


**Figure 4.54:** Schematic diagram of the vortex intensification under decreasing $C_d$. The red arrow indicates the inflow, the blue arrow the rotating flow, and the green arrow the updraft. $C_d$ decreases from left to right.

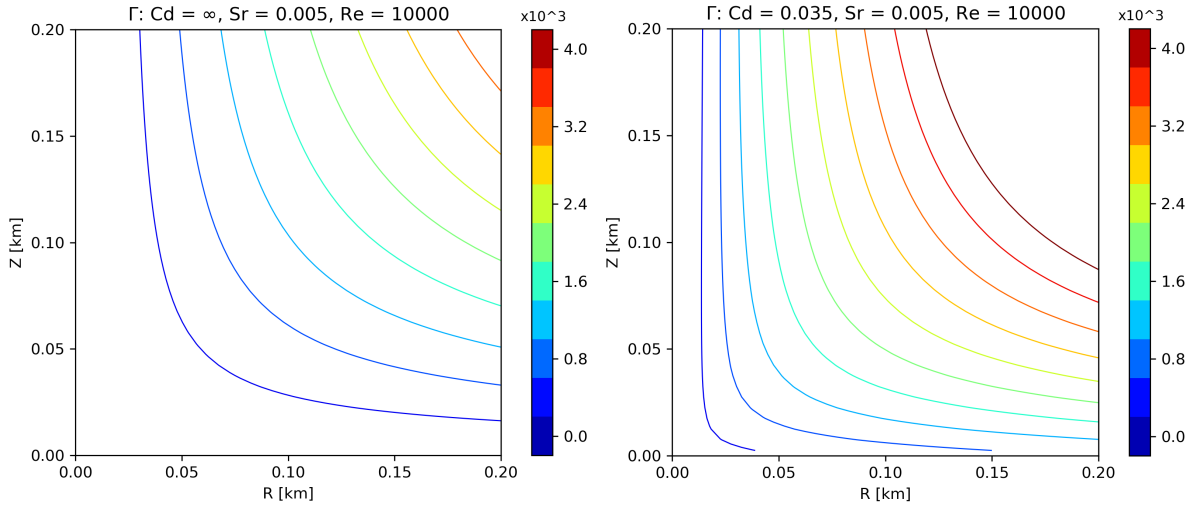


**(a)** **(b)**

**Figure 4.55:** Contourlines of angular momentum in the region $[(0,0),(0.2,0.2)]$ for $S_r = 0.005$, $R_e = 10000$, and a) no-slip conditions ($C_d = \infty$) b) semi-slip conditions with $C_d = 0.035$.

# Chapter 5

# Conclusions

Past research has investigated the dynamics of supercell tornadoes employing idealized supercell simulations, characterized by an axisymmetric cylindrical updraft and a source of rotation. The solutions resulting from this approach are governed by two nondimensional parameters, the swirl ratio $S_r$ (related to the system's rotation), and the Reynolds number $R_e$ (related to diffusive effects). Previous studies have shown that, for fixed $R_e$, a low value of swirl ratio results in a single-celled vortex, with a central updraft. For larger values of $S_r$, the vortex undergoes a breakdown, with the central updraft abruptly transitioning at some level above the surface to a central downdraft surrounded by an updraft. A further increase in swirl ratio leads to the downdraft reaching the surface, and the vortex attains a two-celled structure. The vortices produced by the idealized supercells are potential vortices, featuring an area of constant angular momentum. The use of no-slip boundary conditions gives rise to a potential vortex boundary layer, characterized by a radially inward flow towards the center of the vortex (inflow). In particular, the boundary layer exhibits a two-tiered structure, with the radial velocity increasing from zero to a maximum value in the frictional lower tier, before decreasing to zero in the upper inviscid layer.

The aim of the present work has been to investigate the effect of semi-slip lower boundary conditions on simulated supercell tornadoes. We followed the same axisymmetric approach of previous studies, simulating the supercell's spinning updraft as a rotating cylindrical domain with a prescribed upward forcing, but employing a drag law as the bottom boundary condition. We employed three combinations of $S_r$ - $R_e$, with $R_e$ kept constant at 10000, representing a single-celled vortex ($S_r = 0.005$), a single-celled vortex near transition ($S_r = 0.01$), and a two-celled vortex ($S_r = 0.04$). For each of these combinations, we performed sixteen semi-slip simulations with the friction coefficient ($C_d$) ranging from $C_d = 0.2$ to $C_d = 0.0001$, along with no-slip and free-slip cases. The results show that the two-tiered potential vortex boundary layer is preserved under a wide range of friction coefficients, from $C_d = 0.2$ to $C_d = 0.005$. The lower frictional layer becomes narrower as $C_d$ decreases, vanishing between $C_d = 0.005$ and $C_d = 0.001$.

For $C_d \leq 0.001$, the potential vortex boundary layer is no longer maintained and the solution exhibits features similar to the free-slip case, such as an enhanced vertical alignment of all fields. Although obtained for tornado-like vortices, these results can be useful for a broad range of atmospheric vortices exhibiting a potential vortex radial profile of azimuthal winds. For instance, tropical cyclones and hurricanes exhibit radial profiles of tangential wind approximately in agreement with the potential vortex assumption from the region of maximum rotational velocity outward.

The analysis of the vortex structures has shown that a decrease in $C_d$ for fixed $S_r$ and $R_e$ leads to the same structural changes previously observed for increasing $S_r$ and fixed $R_e$ under no-slip conditions. Starting from a vortex that is single-celled in the no-slip case, a decrease in $C_d$ results in a tightening and intensification of the vortex, eventually leading to the occurrence of a vortex breakdown. A further decrease in friction causes the breakdown to shift toward the surface, and the vortex attains a two-celled structure when the breakdown and the downdraft reach the surface. For even lower $C_d$, the vortex broadens, with a larger central area exhibiting a weak downdraft. All the structures observed are in agreement with previous no-slip simulations and laboratory experiments. These outcomes suggest that the parameter space is a three-dimensional space, with the three nondimensional parameters $S_r$, $R_e$, and $C_d$ determining the solution.

The adoption of semi-slip boundary conditions results in a more accurate representation of the lowest levels of a tornado. Our simulations show that the maximum tangential wind speed can be found at very low levels; for instance, the simulation for $S_r = 0.005$, $R_e = 10000$, and $C_d = 0.02$ exhibits the maximum of rotational velocity at 12.5 meters. This is a significant improvement over no-slip conditions, usually employed in idealized tornado simulations and cloud models, which lead to weaker winds near the surface compared to upper levels. The accurate representation of the lowest levels of a tornado is crucial since the near-surface winds are the cause of the damage and loss of lives brought by these extreme weather phenomena. Moreover, recent Doppler on wheels measurements indicate that the strongest tornado winds are found at the lowest levels ($< 15$ meters above ground level), in agreement with the findings of our surface drag simulations, providing additional motivation to the investigation of semi-slip lower boundary conditions.

This study has shown that within a certain range of $C_d$ values ($C_d = 0.2 - 0.035$), a decrease in friction leads to an intensification of the vortex. A reduction in friction within this range of $C_d$ leads to a strengthening and shift of the inflow towards the center of the vortex, while the reduced dissipation of angular momentum allows the advection by the inflow of parcels with large angular momentum in the vicinity of the origin. The combination of these two effects results in a significant intensification of the swirling motion, while the proximity of the inflow to the center of the vortex forces the inward flow to be funneled tightly into the updraft, boosting the intensity of the vertical velocity. A schematic diagram of the intensification under decreasing $C_d$ is shown in figure 5.1. This effect has been observed for the ($S_r = 0.005$, $R_e = 10000$) case but not

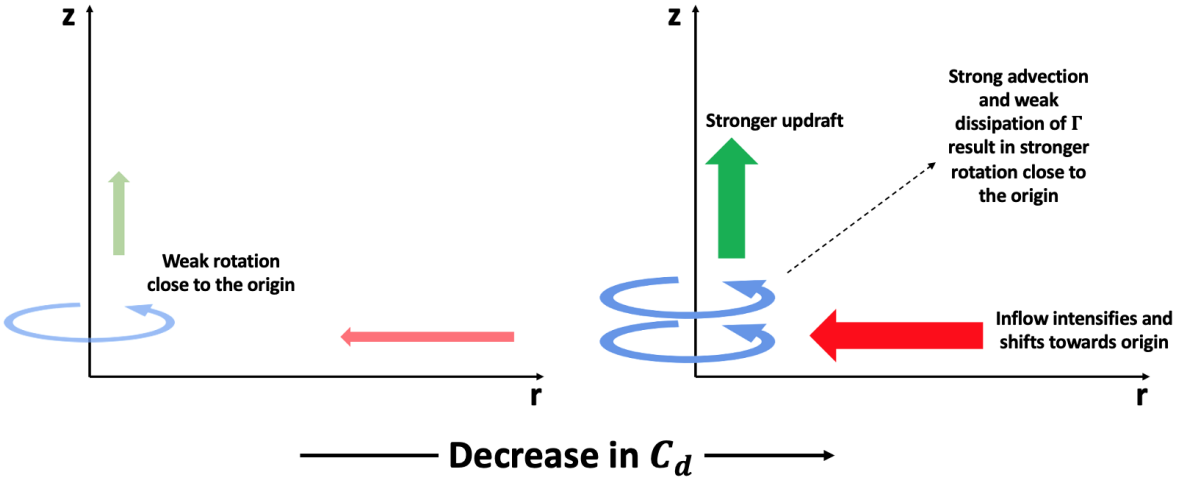


**Figure 5.1:** Schematic diagram of the vortex intensification under decreasing $C_d$. The red arrow indicates the inflow, the blue arrow the rotating flow, and the green arrow the updraft. $C_d$ decreases from left to right.

for the ($S_r = 0.01$, $R_e = 10000$) one, suggesting that the structure of the vortex might play a role. A follow-up of this work, with more simulations in the range of swirl ratios from one-celled to transitional vortices, is needed to better understand the role of vortex structure in the intensification for decreasing friction coefficient.

The limitation of the approach followed in this work is that the experimental setup employs somewhat artificial assumptions, with a steady-state, axisymmetric approach, a prescribed forcing in lieu of the buoyancy acceleration, and a linear damping near the impermeable top boundary instead of the tropopause. Although artificial, these assumptions allow us to simplify the complex dynamics of a tornado-producing supercell, enabling us to investigate the dynamics of tornadoes with a reasonable computational cost. Notably, the assumptions lead to potential vortex radial profiles of tangential winds, in agreement with the profiles observed for natural tornadoes.

The results obtained suggest that the role of surface friction on mature tornadoes should be further investigated. The findings of the present study can provide the basis for an in-depth analysis, employing axisymmetric simulations of vortices exhibiting structures in the range from single-celled to transitional, as it appears that surface drag plays a crucial role in determining the maximum intensity of the rotation. Moreover, the height at which maximum intensity is achieved is strongly related to the $C_d$ value, hence semi-slip conditions could be employed in three-dimensional storm models to provide a more accurate estimate of the impact of tornadoes on man-made structures. Finally, a detailed analysis of the parameter space may be the basis for the development of a parameterization scheme that represents better the characteristics of the solution as a function of the control parameters.

# Appendix 1

For simplicity, the demonstration is carried out in cartesian coordinates. In frictionless, steady-state conditions, with no gravity and using Einstein's notation, the Navier-Stokes equations become the Euler equations:

$$u_j \frac{\partial u_i}{\partial x_j} = -\frac{\partial \phi}{\partial x_i},\ i, j = 1, 2, 3. \tag{5.1}$$

Multiplying each side by $u_i$ we get:

$$u_i u_j \frac{\partial u_i}{\partial x_j} = \frac{u_j}{2} \frac{\partial u_i^2}{\partial x_j} = -u_i \frac{\partial \phi}{\partial x_i}. \tag{5.2}$$

We can now replace the repeated index $j$ with $i$, and bring everything to the same side:

$$u_i \frac{\partial}{\partial x_i} \left( \frac{u_i^2}{2} + \phi \right) = 0. \tag{5.3}$$

Finally, noticing that

$$\frac{u_i^2}{2} + \phi = \frac{v^2}{2} + \frac{u^2}{2} + \frac{w^2}{2} + \phi = H \tag{5.4}$$

it is clear that the head is constant along a streamline.

# Appendix 2

To prove that $-ur$ is related to the inflow mass flux, let us compute the volume flux across the lateral surface of a cylinder of radius $R$ and height $Z$. A schematic diagram of the situation is shown in figure 5.2. Given the axisimmetric nature of the model, we assume the inpinging flow to be purely radial and axisymmetric. The volume flux $Q$ is:

$$Q = \iint_S \vec{u} \cdot \hat{n}\, ds \tag{5.5}$$

where $S$ is the lateral surface of the cylinder, $\hat{n}$ the surface unit vector (pointing outwards), and $ds = rd\theta dz$ the infinitesimal surface. We expand equation (5.5), exploiting the axial symmetry:

$$Q = \int_0^{2\pi} \int_0^Z -ur\, d\theta\, dz = 2\pi \int_0^Z -ur\, dz. \tag{5.6}$$

Since the model employs a constant density, the volume flux is proportional to the mass flux. Therefore, equation (5.6) proves that $-ur$ is related to the inflow mass flux.

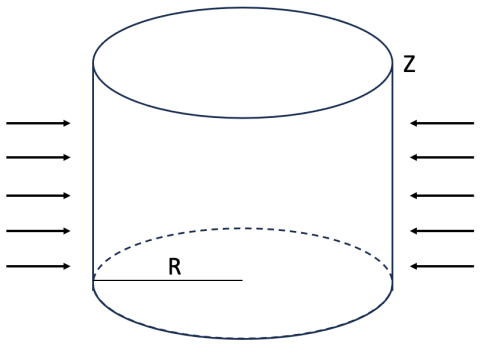


**Figure 5.2:** Schematic diagram of the situation with a radial inward flow inpinging on a cylinder of radius $R$ and height $Z$.

# Acknowledgments

I gratefully acknowledge the Mesoscale and Microscale Meteorology laboratory of the National Center for Atmospheric Research for funding my visitor stay at NCAR, and for allowing me to perform the simulations on the cluster Casper. I thank Dr. George H. Bryan for sharing with me the details of the implementation of CM1, and for giving me precious advices. I thank Hank Schyma for allowing me to showcase one of his incredible photos in my thesis.

I gratefully thank Dr. Carlo Cintolesi for the support and advice he gave me along the way. I want to express my sincere gratitude to Dr. Marcello Miglietta and Dr. Richard Rotunno for all the effort they put into providing me with the incredible opportunity to work on this project, as well as for all the insightful suggestions they shared with me. I thank Prof. Vincenzo Levizzani for kindly getting me in contact with Marcello, and spending nice words for me.

I want to thank my family for all the support they gave me. I thank my brother Nicola for all the laughs we share together, and for the love he constantly gives me. I want to express my appreciation to my friends, in particular to Stefano Franzoni, for his help along this bumpy journey. Finally, I want to thank my Sunset for everything she has done for me, and for filling my days with immense joy.

# Bibliography


[LP64] Lumley, J.L. and Panofsky, H.A. *The Structure of Atmospheric Turbulence*. Interscience monographs and texts in physics and astronomy. Interscience Publishers, 1964. ISBN: 9780470553657.

[BSB71] Burggraf, Odus R., Stewartson, Keith, and Belcher, Ralph. Boundary Layer Induced by a Potential Vortex. In: *The Physics of Fluids* 14.9 (Sept. 1971), pp. 1821–1833. ISSN: 0031-9171. DOI: 10.1063/1.1693691.

[War72] Ward, Neil B. The exploration of certain features of tornado dynamics using a laboratory model. In: *Journal of Atmospheric Sciences* 29.6 (1972), pp. 1194–1204. DOI: https://doi.org/10.1175/1520-0469(1972)029<1194:TEOCFO>2.0.CO;2.

[CSA77] Church, CR, Snow, JT, and Agee, EM. Tornado vortex simulation at Purdue University. In: *Bulletin of the American Meteorological Society* 58.9 (1977), pp. 900–909. DOI: https://doi.org/10.1175/1520-0477(1977)058<0900:TVSAPU>2.0.CO;2.

[KW78] Klemp, Joseph B. and Wilhelmson, Robert B. The Simulation of Three-Dimensional Convective Storm Dynamics. In: *Journal of Atmospheric Sciences* 35.6 (1978), pp. 1070–1096. DOI: https://doi.org/10.1175/1520-0469(1978)035<1070:TSOTDC>2.0.CO;2.

[Chu+79] Church, CRo, Snow, JT, Baker, GL, and Agee, EM. Characteristics of tornado-like vortices as a function of swirl ratio: A laboratory investigation. In: *Journal of Atmospheric Sciences* 36.9 (1979), pp. 1755–1776. DOI: https://doi.org/10.1175/1520-0469(1979)036<1755:COTLVA>2.0.CO;2.

[Ema86] Emanuel, Kerry A. An air-sea interaction theory for tropical cyclones. Part I: Steady-state maintenance. In: *Journal of Atmospheric Sciences* 43.6 (1986), pp. 585–605. DOI: https://doi.org/10.1175/1520-0469(1986)043<0585:AASITF>2.0.CO;2.

[SK92] Skamarock, William C. and Klemp, Joseph B. The Stability of Time-Split Numerical Methods for the Hydrostatic and the Nonhydrostatic Elastic Equations. In: *Monthly Weather Review* 120.9 (1992), pp. 2109–2127. DOI: https://doi.org/10.1175/1520-0493(1992)120<2109:TSOTSN>2.0.CO;2.

[Fie94] Fiedler, Brian H. The thermodynamic speed limit and its violation in axisymmetric numerical simulations of tornado-like vortices. In: *Atmosphere-Ocean* 32.2 (1994), pp. 335–359. DOI: 10.1080/07055900.1994.9649501.

[Fie95] Fiedler, Brian H. On Modelling Tornadoes in isolation from the Parent Storm. In: *Atmosphere-Ocean* 33.3 (1995), pp. 501–512. DOI: 10.1080/07055900.1995.9649542.

[Bat00] Batchelor, G. K. *An Introduction to Fluid Dynamics*. Cambridge Mathematical Library. Cambridge University Press, 2000. DOI: 10.1017/CBO9780511800955.

[LLX00] Lewellen, DC, Lewellen, WS, and Xia, J. The influence of a local swirl ratio on tornado intensification near the surface. In: *Journal of the atmospheric sciences* 57.4 (2000), pp. 527–544. DOI: https://doi.org/10.1175/1520-0469(2000)057<0527:TIOALS>2.0.CO;2.

[DTB01] Davies-Jones, Robert, Trapp, R. Jeffrey, and Bluestein, Howard B. Tornadoes and Tornadic Storms. In: *Severe Convective Storms*. Ed. by Charles A. Doswell. Boston, MA: American Meteorological Society, 2001, pp. 167–221. ISBN: 978-1-935704-06-5. DOI: 10.1007/978-1-935704-06-5_5.

[BF02] Bryan, George H. and Fritsch, J. Michael. A Benchmark Simulation for Moist Nonhydrostatic Numerical Models. In: *Monthly Weather Review* 130.12 (2002), pp. 2917–2928. DOI: https://doi.org/10.1175/1520-0493(2002)130<2917:ABSFMN>2.0.CO;2.

[WS02] Wicker, Louis J. and Skamarock, William C. Time-Splitting Methods for Elastic Models Using Forward Time Schemes. In: *Monthly Weather Review* 130.8 (2002), pp. 2088–2097. DOI: https://doi.org/10.1175/1520-0493(2002)130<2088:TSMFEM>2.0.CO;2.

[MMW05] Mallen, Kevin J., Montgomery, Michael T., and Wang, Bin. Reexamining the Near-Core Radial Structure of the Tropical Cyclone Primary Circulation: Implications for Vortex Resiliency. In: *Journal of the Atmospheric Sciences* 62.2 (2005), pp. 408–425. DOI: https://doi.org/10.1175/JAS-3377.1.

[Nol05] Nolan, David S. A New Scaling for Tornado-Like Vortices. In: *Journal of the Atmospheric Sciences* 62.7 (2005), pp. 2639–2645. DOI: https://doi.org/10.1175/JAS3461.1.

[WH06] Wallace, John M. and Hobbs, Peter V. *Atmospheric Science, an Introductory Survey*. Academic Press, 2006. ISBN: 978-0-12-732951-2. DOI: https://doi.org/10.1016/B978-0-12-732951-2.50013-2.

[Tan+07] Tanamachi, Robin L, Bluestein, Howard B, Lee, Wen-Chau, Bell, Michael, and Pazmany, Andrew. Ground-based velocity track display (GBVTD) analysis of W-band Doppler radar data in a tornado near Stockton, Kansas, on 15 May 1999. In: *Monthly weather review* 135.3 (2007), pp. 783–800. DOI: https://doi.org/10.1175/MWR3325.1.

[AW08] Alexander, Curtis R. and Wurman, Joshua M. Updated mobile radar climatology of supercell tornado structures and dynamics. In: *24th Conference on Severe Local Storms* (2008).

[Bor+08] Borges, Rafael, Carmona, Monique, Costa, Bruno, and Don, Wai Sun. An improved weighted essentially non-oscillatory scheme for hyperbolic conservation laws. In: *Journal of Computational Physics* 227.6 (2008), pp. 3191–3211. ISSN: 0021-9991. DOI: https://doi.org/10.1016/j.jcp.2007.11.038.

[BR09] Bryan, George H. and Rotunno, Richard. The Maximum Intensity of Tropical Cyclones in Axisymmetric Numerical Model Simulations. In: *Monthly Weather Review* 137.6 (2009), pp. 1770–1789. DOI: https://doi.org/10.1175/2008MWR2709.1.

[Fie09] Fiedler, Brian. Suction vortices and spiral breakdown in numerical simulations of tornado-like vortices. In: *Atmospheric Science Letters* 10.2 (2009), pp. 109–114. DOI: https://doi.org/10.1002/asl.217.

[How13] Howard, B Bluestein. *Severe Convective Storms and Tornadoes: Observations and Dynamics*. Springer, Berlin, Heidelberg, 2013. ISBN: 978-3642053801.

[KW13] Kosiba, Karen A. and Wurman, Joshua. The Three-Dimensional Structure and Evolution of a Tornado Boundary Layer. In: *Weather and Forecasting* 28.6 (2013), pp. 1552–1561. DOI: https://doi.org/10.1175/WAF-D-13-00070.1.

[Rot13] Rotunno, Richard. The Fluid Dynamics of Tornadoes. In: *Annual Review of Fluid Mechanics* 45.1 (2013), pp. 59–84. DOI: 10.1146/annurev-fluid-011212-140639.

[Rot14] Rotunno, Richard. Secondary circulations in rotating-flow boundary layers. In: *Australian Meteorological and Oceanographic Journal* 64 (Mar. 2014), pp. 27–35. DOI: 10.22499/2.6401.004.

[Dav15] Davies-Jones, Robert. A review of supercell and tornado dynamics. In: *Atmospheric Research* 158-159 (2015), pp. 274–291. ISSN: 0169-8095. DOI: https://doi.org/10.1016/j.atmosres.2014.04.007.

[SM15] Smith, Adam B. and Matthews, Jessica L. Quantifying uncertainty and variable sensitivity within the US billion-dollar weather and climate disaster cost estimates. In: *Natural Hazards* 77.3 (July 2015), pp. 1829–1851. ISSN: 1573-0840. DOI: 10.1007/s11069-015-1678-x.

[AS16] Ashley, Walker S. and Strader, Stephen M. Recipe for Disaster: How the Dynamic Ingredients of Risk and Exposure Are Changing the Tornado Disaster Landscape. In: *Bulletin of the American Meteorological Society* 97.5 (2016), pp. 767–786. DOI: https://doi.org/10.1175/BAMS-D-15-00150.1.

[Rob+16] Roberts, Brett, Xue, Ming, Schenkman, Alexander D, and Dawson, Daniel T. The role of surface drag in tornadogenesis within an idealized supercell simulation. In: *Journal of the Atmospheric Sciences* 73.9 (2016), pp. 3371–3395. DOI: https://doi.org/10.1175/JAS-D-15-0332.1.

[Rot+16] Rotunno, Richard, Bryan, George H., Nolan, David S., and Dahl, Nathan A. Axisymmetric Tornado Simulations at High Reynolds Number. In: *Journal of the Atmospheric Sciences* 73.10 (2016), pp. 3843–3854. DOI: https://doi.org/10.1175/JAS-D-16-0038.1.

[CP17] Coffer, Brice E and Parker, Matthew D. Simulated supercells in nontornadic and tornadic VORTEX2 environments. In: *Monthly Weather Review* 145.1 (2017), pp. 149–180. DOI: https://doi.org/10.1175/MWR-D-16-0226.1.

[Fie17] Fiedler, Brian H. Axisymmetric Tornado Simulations with a Semi-Slip Boundary. In: *Fluids* 2.4 (2017). ISSN: 2311-5521. DOI: 10.3390/fluids2040068. URL: https://www.mdpi.com/2311-5521/2/4/68.

[Nol+17] Nolan, David S, Dahl, Nathan A, Bryan, George H, and Rotunno, Richard. Tornado vortex structure, intensity, and surface wind gusts in large-eddy simulations with fully developed turbulence. In: *Journal of the Atmospheric Sciences* 74.5 (2017), pp. 1573–1597. DOI: https://doi.org/10.1175/JAS-D-16-0258.1.

[Orf+17] Orf, Leigh, Wilhelmson, Robert, Lee, Bruce, Finley, Catherine, and Houston, Adam. Evolution of a long-track violent tornado within a simulated supercell. In: *Bulletin of the American Meteorological Society* 98.1 (2017), pp. 45–68. DOI: https://doi.org/10.1175/BAMS-D-15-00073.1.

[KW23] Kosiba, Karen and Wurman, Joshua. The strongest winds in tornadoes are very near the ground. In: *Communications Earth & Environment* 4.1 (Feb. 2023), p. 50. ISSN: 2662-4435. DOI: 10.1038/s43247-023-00716-6.